(6)

Metrology of Very Thin Silicon Epitaxial Films

by

Alexander Cherkassky

B.S., Electrical Engineering and Computer Science
Massachusetts Institute of Technology, June 1987

M.S., Electrical Engineering and Computer Science
Massachusetts Institute of Technology, June 1995

Submitted to the
Department of Electrical Engineering and Computer Science
in partial fulfillment of the requirements for the degree of

Doctor of Science in Electrical Engineering

at the

Massachusetts Institute of Technology

May 1998

Signature of Author .....
Department of Electrical Engineering and Computer Science
May 6, 1995

Certified by .....
Rafael Reif
Professor of Electrical Engineering and Computer Science
Director, Microsystems Technology Laboratories
Thesis Supervisor

Accepted by .....
Arthur C. Smith
Chairman, Departmental Committee on Graduate Students

Metrology of Very Thin Silicon Epitaxial Films

By

Alexander Cherkassky

Submitted to the Department of Electrical Engineering and Computer Science
in partial fulfillment of the requirements for the degree of
Doctor of Science in Electrical Engineering

Abstract

This thesis presents the methods, models and algorithms enabling characterization of very thin (500 nm and below) silicon epitaxial films on silicon substrates using Fourier Transform Infrared spectrometry and Infrared Spectroscopic Ellipsometry.

Semiconductor industry has relied on Fourier Transform Infrared (FT-IR) spectrometry for measurements of silicon epi-layer thickness. Such measurements are performed in the interferogram domain and are limited to relatively thick (1 um and above) films on very heavily doped (> 10^{19} cm^{-3}) substrates. These are also single-purpose measurements limited to the thickness determination only. It is shown in this thesis that FT-IR in the frequency mode, coupled with physical models and signal processing and optimization algorithms, overcomes its traditional limitations and extends the measurement range by more than an order of magnitude (sub-50 nm films are easily measured), while providing information on a number of additional parameters such as substrate dopant concentration, transition layer thickness and doping profile in the thicker (> 1 um) films, and, if desired, surface roughness. The lower limit on the substrate doping level is extended by at least an order of magnitude as well, with measurements on 100 nm-class films on 10^{18} cm^{-3} substrates demonstrated.

The models and methods are further extended into the domain of Spectroscopic Ellipsometry. Spectroscopic Ellipsometry (SE) in the UV, visible and near-IR spectral ranges has traditionally been utilized for non-destructive analysis of very thin films and multi-layer stacks on variety of substrates. However, these spectral ranges make the SE method unsuitable to the silicon epi-layer measurements. Recently, spectroscopic ellipsometry in the infrared has become possible by combining infrared spectrometry and ellipsometry with the use of FTIR. In the second portion of this thesis, infrared spectroscopic ellipsometry (IRSE) is specialized to the problem of epitaxial silicon using the extensions of the models and algorithms developed in the first half of the thesis. It is shown that IRSE retains the FTIR advantages associated with operating in the infrared portion of the spectrum while improving the accuracy and sensitivity of the measurements by another order of magnitude, making possible monolayer measurements with sub-monolayer sensitivity.

Although silicon epi-layers are the focus of this study, the methods developed here are applicable to other semiconductor structures where optical contrast exists due to the differences in the doping levels. Using finite element methods, it is shown that ultra-shallow junctions can be accurately characterized by these techniques. Other structures of interest may include variety of ion implanted or diffused profiles, and selectively grown epitaxial films. The methods are also suitable for in-line and in-situ applications.

Thesis Supervisor: L. Rafael Reif
Title: Professor, Department of Electrical Engineering and Computer Science
Director, Microsystems Technology Laboratories

Acknowledgments

This thesis would be incomplete if I failed to thank those who, directly and indirectly, aided me in my work, and helped me make it a success. First, I wish to thank Professor Reif, my thesis advisor, for the confidence he always expressed in me and my ideas, and encouragement he provided throughout my stay in graduate school. When, in the beginning of this project, the ideas on which this thesis rests received a great deal of skepticism, having gone against the conventional wisdom, he did not hesitate for a moment. It is fair to say that without his support, this work would not have happened.

I would also like to thank Professor Hank Smith, who made me explore deeper into the optics of stochastic light and seek connection between optics and systems and stochastic processes, which turned out so important in this work. I am grateful to Professor Boning for agreeing to be on the thesis committee and for reading through this manuscript. I also want to thank the outstanding members of the M.I.T. faculty under whose influence I came during the academic portion of my graduate school. My understanding of and approach to solving problems in the diverse areas of solid state and device physics, microfabrication, optics, communication theory and signal processing undoubtedly bears their mark.

I thank Dave Simmons of SEMATECH for assisting with samples, and Dr. Krishnan of Bio-Rad Laboratories and Dr. Peter Rosenthal of Advanced Fuel Research for useful discussions and assisting with measurements, and J-C. Fouere of SOPRA for making available IR ellipsometer.

My gratitude goes to my colleagues, past: Zhen Zhou, Ken Liaou, Julie Tsai, Andy Tang and Weize Chen, and present members of our research group: Rajan Naik, Simon Karecki, Laura Pruette, Andy Phan, and my trusty office companion Mingao Qi. I thank our former secretary Carolyn Zaccaria and the assistants to our busy professor, Dianne Hagopian and Sam Crooks.

My very special thanks go to my friends Ilya and Farhad, and my cousin Brian, for being there to take the load off, share a joke or simply staying in touch.

I thank my parents for raising me and stimulating my interest in science and technology, and I am grateful to my aunt for always being ready to help.

And last, but most important of all, my dear grandparents. My grandfather, who is no longer with us, but whose kindness, good humor, and optimistic outlook on life shall remain with me always. And my grandmother, a most tremendous woman, whose beauty, creative ability, and great strength have been inspiration to me throughout my life.

Table of Contents

List of Figures

Tables

Thesis Organization

This thesis is organized in 6 chapters. Chapter 1 is an introduction. The use of silicon epitaxy in the IC fabrication process is described and the need for non-destructive means of thin epi characterization is explained. The history and the existing techniques for epi-layer measurements are reviewed. Ellipsometry and FT-IR are presented as the natural techniques for thin epi analysis. Advantages and disadvantages of each conventional method are discussed.

Chapter 2 develops the FT-IR theory from the statistical signal processing point of view. The IR source is treated as a random process with randomly distributed phases and polarizations passing through a series of shaping filters. The property of the Michelson interferometer as autocorrelator of the random process is established. The parasitic frequency responses of the electronic and optical components of the FT-IR are considered and the overall linear system model for the combined FT-IR/epi-substrate system is derived. The advantages of performing measurements in the frequency mode are discussed and the techniques for minimizing the influences of the parasitic frequency responses are presented.

Chapter 3 deals with the issues of reflection and transmission of chaotic light in the dispersive media of heavily doped silicon substrate at non-normal angle of incidence as well as in the film-on-dispersive-substrate system. The effects of native oxide are considered. The Fresnel reflection and transmission coefficients are determined using hypothetical complex refractive index and the overall reflectance is obtained. The required complex refractive index of heavily doped silicon is considered next. The Drude model is used to obtain the substrate conductivity, and the refractive index and the extinction coefficient are obtained phenomenologically from the complex Maxwell equations.

Chapter 4 discusses FT-IR measurements in the reflectance mode. Combining the linear system model of the FT-IR/epi-substrate system and physical model of silicon optical properties in the infrared with methods in non-linear optimization, the parameters of interest are obtained by

optimizing the model parameters for the best fit against the experimental data. The effects of the epi-substrate transition layer on the measurements is discussed and the conditions for obtaining the dopant profiles are determined. The results of the extensive SIMS characterization are presented and compared with the measurement predictions. The applications of the methods to other structures of importance in the current and future IC fabrication are discussed with one such structure, ultra-shallow junction, considered in more detail.

Chapter 5 discusses the application of infrared spectroscopic ellipsometry to thin epi-layer characterization. IRSE is presented as the natural extension of the FT-IR spectrometry. The methods previously developed for FT-IR are further evolved to take advantage of the IRSE capabilities. The ellipsometric measurements of thin epi-layers are presented, and the measurement predictions are compared against the results of SIMS characterization as well as those obtained by FT-IR. The pros and cons of IRSE vs. FT-IR techniques are discussed and potential improvements to the experimental IRSE hardware are suggested.

Chapter 6 concludes the thesis. The achievements of the work thus presented are summarized, and the discrepancies are pointed out with some suggestions for addressing the latter. Recommendations for future research opportunities in this area, some of which very promising, are suggested. These include *In-situ* measurements and extensions of the methods to patterned structures. Application of IRSE to *In-situ* measurements in the emission mode appears particularly promising.

Chapter 1.

Introduction

1.1 Silicon Epitaxial Films in IC Fabrication

Silicon epitaxy is a process where a thin layer of crystalline silicon is grown on a crystalline substrate. It is one of the most common steps in the modern IC fabrication process, used to manufacture analog and digital, discrete and integrated devices in CMOS, BiCMOS and bipolar technologies. The reasons for using epitaxy in the IC fabrication are many and varied, but the great majority of cases include growing lightly doped or undoped epi-layer on a heavily doped (> 1E18 cm^{-3}) silicon substrate [1]. Modern CMOS and BiCMOS processes use heavily doped substrate to improve resistance to latch-up, while the lightly doped oxygen- and carbon-free epi preserves high mobility and low leakage currents necessary for good device performance. In the discrete and analog bipolar processes, the lightly doped epi is used to improve the collector breakdown voltage of the device while heavily doped buried layer improves the collector resistance [2]. Today

Year technology	1997 250 (nm)	1999 180	2001 150	2003 130	2006 100	2009 70	2012 50
Epi (um)	2-5 ±5%	2-4 ±4%	2-4 ±4%	2-4 ±4%	1-3 ±3%	1-3 ±3%	1-3 ±3%
Elev. S/D (nm)	-	-	-	-	20-40	15-30	15-30
Shallow J. (nm)	50-100	36-72	30-60	25-52	-	-	-

Table 1: Characteristics of epitaxial-like structures in future IC technology. National Technology Roadmap for Semiconductors, 1997 [3]. Epi characteristics (first row) refer to mainstream blanket epitaxial wafers. Other devices use epi-layers in the 0.5 – 1 um range

the majority of logic ICs, including virtually all high-performance devices, as well as a considerable fraction of DRAMs employ thin epitaxial wafers as the silicon starting material [4]. This trend is expected to continue well beyond the year 2000, with percentage of epitaxial wafers increasing towards 50% of all silicon wafer market [5]. The low end of epi film thickness in the modern CMOS IC process currently stands at 0.5 um - 1 um. Continuing lateral and vertical scaling of the IC features will undoubtedly cause this number to decrease. The costs of processing epitaxial wafers are substantial: at 200 mm, epi wafers double the substrate cost, to $200 from $100 [6]. The current price for 300 mm blank silicon slices is upward $1000 [7]. To combat the high costs of blanket epi wafers, some manufacturers are studying alternative techniques, such as MeV implantation [8]. Such techniques are complementary to silicon epitaxy, and are not meant to replace it, certainly not selective epitaxy. However, the need to control the end product of these alternative steps, *epitaxial quality* silicon on heavily doped burried layer, still remains. In addition, advanced device structures for 100 nm-class MOSFETs are expected to employ very thin silicon epi-layers. One such structure, elevated sorce/drain MOSFET utilizing sub-100 nm epi-layers, is shown in Figure 1 [9-11]. Another important future technology utilizing ultra-thin epi-layers is epitaxially deposited hyper-abrupt channel structures for sub-100 nm MOSFETs. Such structures are expected to provide an answer to the conflicting requirements of increased

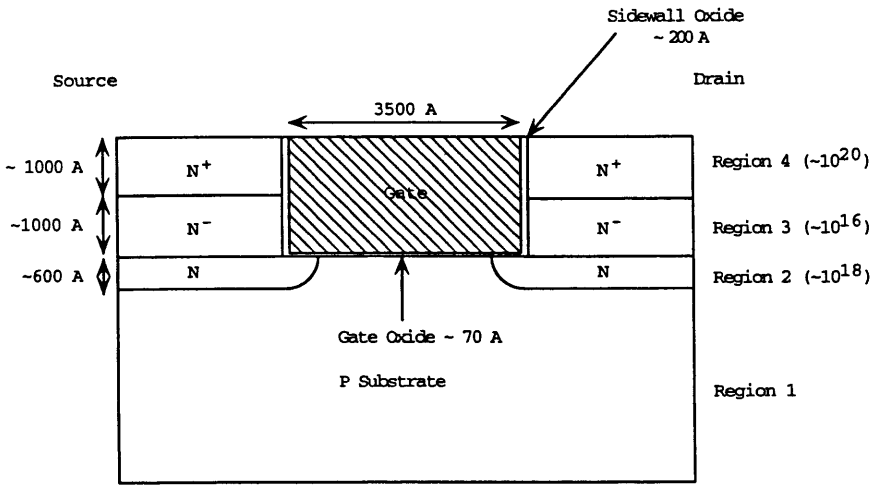

Figure 1: Elevated Source/Drain MOSFET: N^- and N^+ regions are created via selective epitaxy

doping in the channel while achieving abrupt dopant profile [12]. Both elevated S/D MOSFETs and hyper-abrupt channel structures are specifically included in the 1997 issue of The National Technology Roadmap for Semiconductors. Even before these devices come on stream, IC devices are utilizing shallow junction technology for source/drain fabrication, where a very thin heavily doped layer is implanted into moderately doped substrate [13]. Shallow junction technology is one of the most difficult doping applications for the IC industry, noted by the 1997 Roadmap as one of the five most difficult challenges for pre-2006 front-end fabrication processes. Although not an epitaxial technology, formation of the shallow junction results in the thin film structure on top of silicon substrate of different doping level, where the control over the film thickness and doping level is crucial to the device performance. The characteristics of these structures are summarized in Table 1. As the traditional IC devices continue to shrink and advanced structures emerge from the research environment, accurate control, *in-situ* and real-time, of epitaxial quality silicon thickness, both for the reasons of performance and economics, becomes increasingly important. In order to achieve this, an accurate fast non-destructive method of characterizing epitaxial quality silicon is necessary.

1.2 Traditional Methods of Epi Thickness Measurement, Their Limitations, and Alternative Techniques

Non-destructive determination of silicon epitaxial film thickness has been the subject of interest in the material science community for the last 30 years. Early interest was motivated by the emerging technology of epitaxial bipolar transistors, where device characteristics were improved by utilizing relatively lightly doped epitaxial collector structure grown on top of a heavily doped layer diffused into the starting substrate [14]. Later, as emerging CMOS technology adopted thin epitaxial wafers grown on top of heavily doped substrate as the solution to the latch-up problem with the added benefit of improved structural and electrical perfection [15], the need to be able to accurately measure and control the epi-layer thickness in a non-destructive fashion became prominent.

The solution to the immediate need of the epi-thickness measurement was sought in using two forms of infrared interference. The general method relies on the fact that optical properties of doped silicon in the far to mid-IR are strongly influenced by the presence of free carriers, resulting in the presence of optical contrast between layers of different doping level [16]. Figure 2 and Figure 3 show simulated optical constants (n and k) in the mid-IR spectral range (250 –4500 wavenumbers, or 40 um – 2.5 um wavelength, respectively) for several values of the substrate dopant concentration. It is readily seen that such optical contrast is restricted to far to mid-IR spectral range, and declines rapidly with the doping level. Infrared interference measurements have been carried out via two techniques: Infrared reflectance and FT-IR interferometry.

1.2.1 Infrared Reflectance

The initial thickness measurements were carried out by Spitzer and Tanenbaum in the frequency domain using dispersive spectrophotometry[17]. They observed the interference fringes present in the reflected spectra of relatively thick (> 7 um) epi-layers and estimated film thickness from the

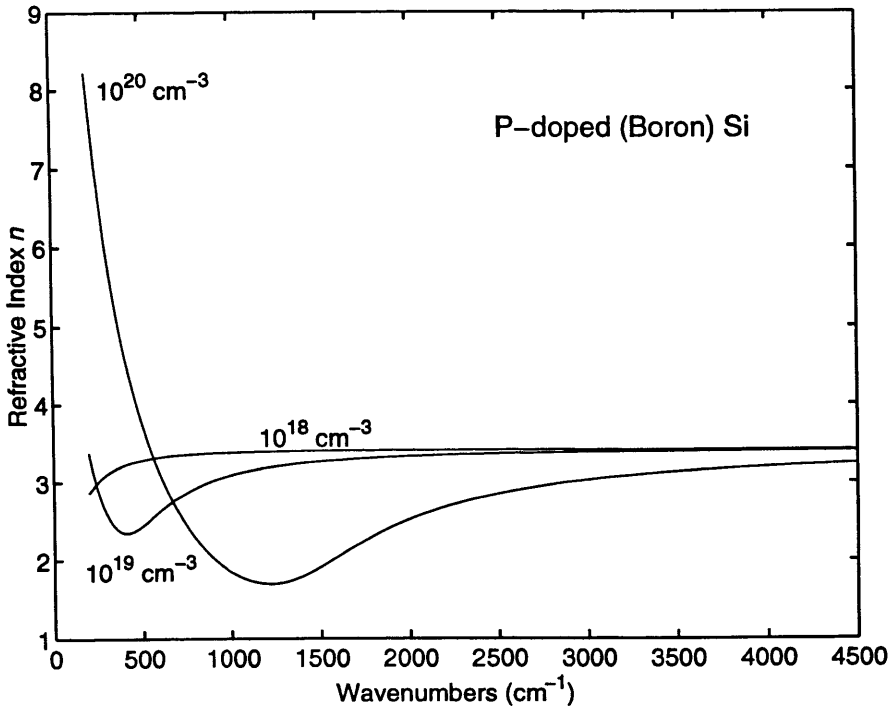

Figure 2: Refractive index n as a function of doping. Refractive index of undoped silicon is 3.42.

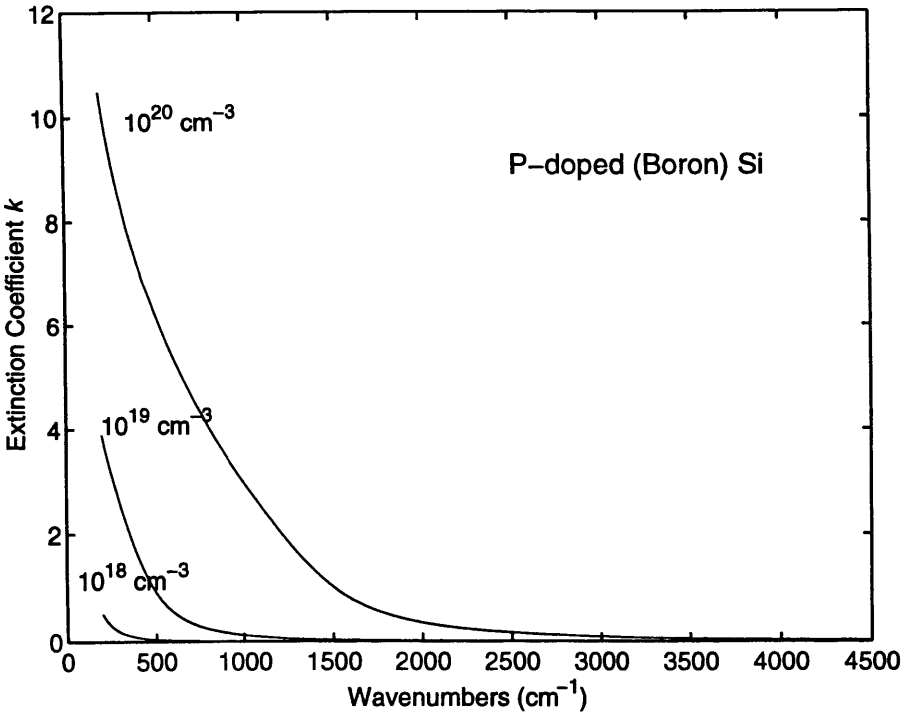

Figure 3: Extinction coefficient k as a function of doping.

position of the fringes. The technique, with some variations, has been adapted as ASTM Test for Thickness of Epitaxial Layers of Silicon on Substrates of the Same Type by Infrared Reflectance (F95) [18]. The main disadvantage of such technique is that the interference fringes are only visible for relatively thick (> 1 um) epi-layers, making the method unsuitable for sub-um films. Even when the fringes are observable, their position and amplitude are strongly influenced by the plasma absorption in the substrate, making the thickness estimates uncertain. In consequence, ASTM method is restricted to layer thickness greater than 2 um, with substrate dopant concentration exceeding 10^{19} cm^{-3}. There have been attempts to improve the technique by accounting for the phase changes upon the reflection at the epi/substrate interface. Schuman *et al.* developed a theory to calculate such changes using classical Boltzmann statistics, however the computations failed to agree with experiments across broad IR frequency range (5-40 um) [19-20]. They also failed to agree with experimental results by Severin who found that the phase shift correction is particularly significant for thin epi-layers[21]. Senitzky and Weeks also attempted to extend IR reflectance technique to thin (0.5 um) epi-layers by comparing Drude model with that of Shuman [22]. They found that Drude model is more applicable to epi-layers on heavily doped substrates (2E19 cm-3) while Schuman model is more accurate for the lower doping levels (5E18). Neither model was able to adequately describe both cases.

1.2.2 FT-IR Interferometry

This technique, due to Flournoy, was introduced in 1972 for measurements of thin polymer films [23], and has since been adopted as the standard method for epi thickness measurement [24]. The method uses FT-IR spectrometer in the interferogram mode. The schematical description of a typical FT-IR set-up as used for epi thickness measurement is shown in Figure 4. As an instrument, FT-IR consists of a Michelson interferometer coupled to a computer system [25]. A Michelson interferometer divides a beam of radiation from an incoherent infra-red source into two paths and recombines them at the detector after a path difference has been introduced,

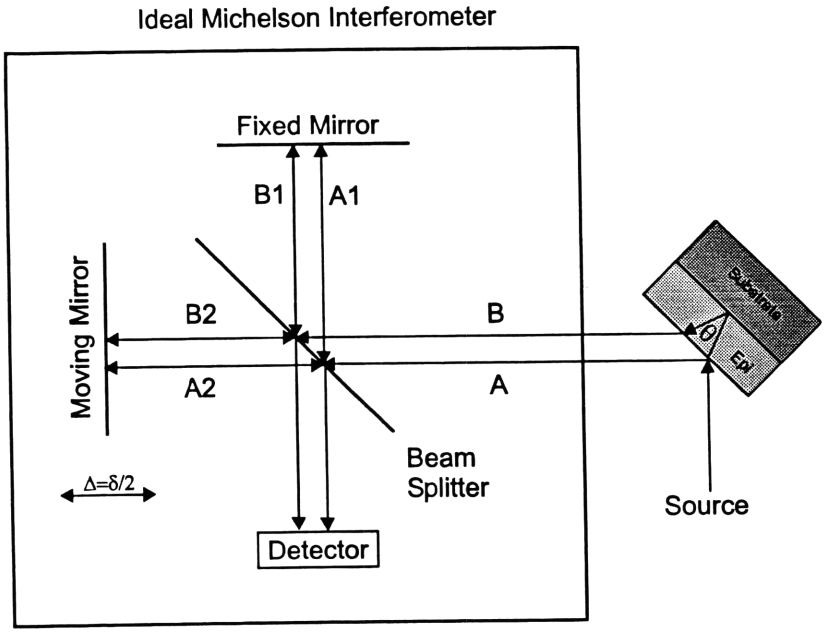

Figure 4: Typical FT-IR Epitaxial Thickness Measurement Set-up

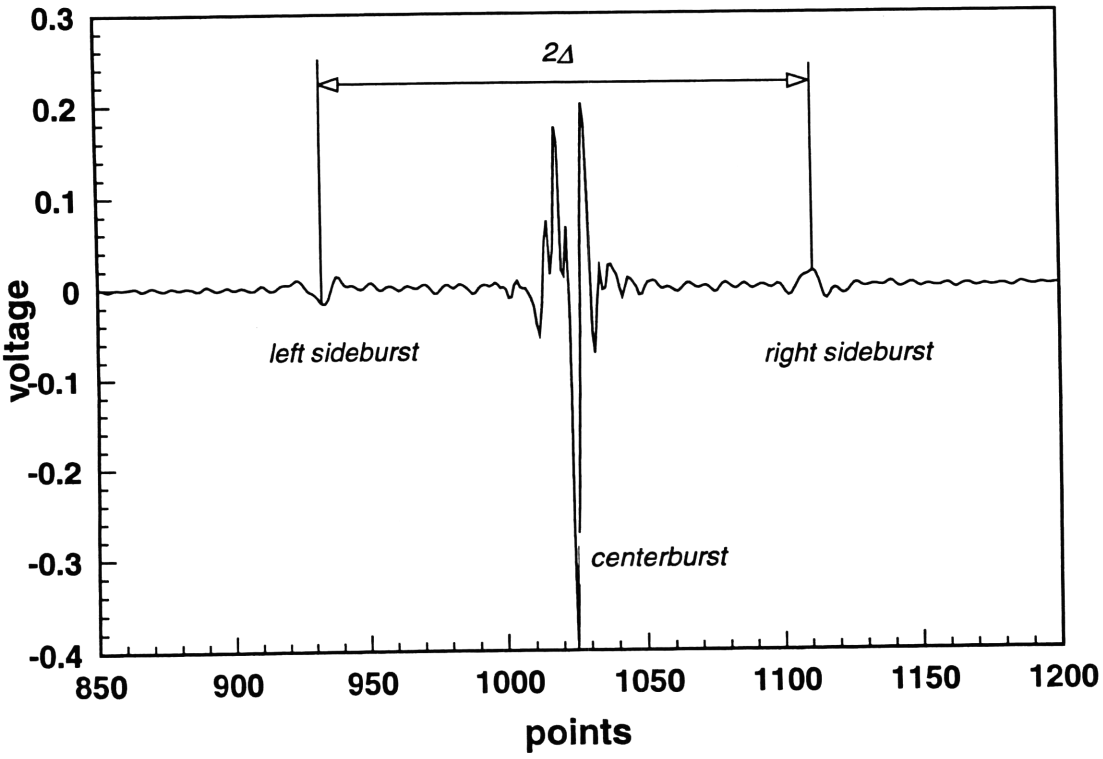

Figure 5: Interferogram of 7 um Epi film

creating a condition under which an *interference* between the two beams can occur. The intensity variation as a function of the path difference is captured by the detector and results in the *interferogram.*

The typical interferogram of a relatively thick epi film on substrate is shown in Figure 5. The interferogram consists of a strong center burst and two similar smaller bursts positioned symmetrically to the sides of the center burst. The shape of the interferogram, including the bursts, can be understood on the qualitative level as follows: referring to the Figure 4, it is seen that incoherent IR light reflected from the sample consists of two primary components: beam A, which is reflected from the surface, and beam B, which is reflected from the epi-substrate interface. The two beams are further divided by the beam splitter into roughly equal components (1 and 2) which are phase shifted with respect to each other. The phase shift is controlled by the position of the scanning mirror, Δ, which is arranged so at $\Delta=0$ the two mirrors are equidistant from the beam splitter. The combined radiation thus reaches the detector, where interference of the four beams takes place. It is a well-known property of statistical optics that a pair of initially correlated beams, when interfered, will create an interference maximum if the path difference between them is zero [26].[1] Assuming the epi-layer thickness d and index of refraction n, and the angle of incidence in the epi-layer θ, the condition for maximum interference will be satisfied at three positions of the scanning mirror:

- At $\Delta=0$, the beams A1 and A2 as well as B1 and B2 arrive at the detector in phase, creating the center peak
- At $\Delta = +2nd\cos\theta$, the beams A1 and B2 arrive at the detector in phase, creating the leftmost peak

[1] This is different from the well-known result for coherent light, which allows the path difference be an integer multiple of $2\pi/\lambda$.

- At $\Delta = -2nd\cos\theta$, the beams A2 and B1 arrive at the detector in phase, creating the rightmost peak.

Thus, observing the peaks one may determine the epi-layer thickness as

$$d = \frac{\Delta}{2n\cos\theta} \tag{1.1}$$

where 2Δ is the distance between the two side-bursts in the interferogram. The particular shape of the peaks is due to the non-ideal behavior of the electronic and optical components of FT-IR as well as the frequency-dependent optical properties of the material under investigation (for example, epi-substrate system). Compared with alternative optical techniques, FT-IR interferometry has a number of advantages:

- Interferogram collection is fast: an interferogram is typically collected in less than a minute, making it suitable for in-situ applications
- The instrument has high optical throughput[2] due to all the radiation being collected at the detector, as opposed to the dispersive methods. This leads to substantially increased signal to noise ratios
- The film thickness is primarily a function of the sidebursts' position rather than their shapes, leading to a relatively simple thickness readout
- The instrument is mechanically robust, with the only moving element being the scanning mirror; relatively inexpensive (a top quality FT-IR is listed at $59K), and, as measurements are typically carried out at low angle of incidence (15-30 degrees), relatively insensitive to alignment errors and polarization effects.

---

[2] Optical throughput is typically defined as the product of the area of the beam at its focus point and its solid angle [25].

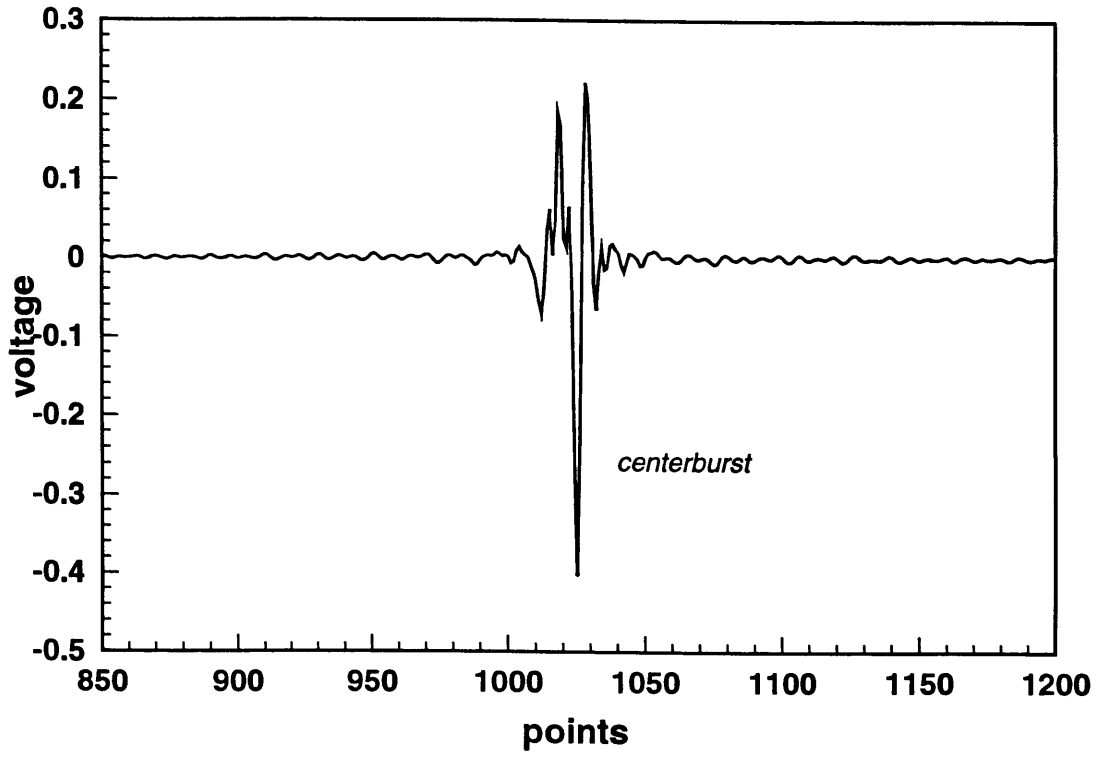

Figure 6: Interferogram of 0.5 um Epi film illustrating absence of characteristic sidebursts

FT-IR has served as the traditional tool in the semiconductor industry for epi thickness measurements.

Despite these benefits, FT-IR suffers from serious disadvantages which limit its applicability to relatively thick (> 1 um) epi-layers. The main disadvantage lies in the non-ideal behavior of the electronic and optical components of FT-IR, such as the source, detector, and beam splitter, as well as the frequency dependent nature of the optical properties of the material under investigation (epi-substrate system), which are collectively responsible for the shape of the peaks. As the film thickness is reduced, the side-bursts move closer together until they overlap with the center burst. As the side-bursts are much weaker than the center-burst, which is made up of the interference of the two primary beams, when overlapped with the center-burst, they will no longer be detectable. Such overlap typically takes place as the film thickness is reduced below 1 um. Figure 6 shows an interferogram of 0.5 um (nominal) epi-layer. It is seen that the side-bursts are

no longer visible in this case. There have been numerous efforts to extend the FT-IR method to sub-um epi films. The main technique attempts to eliminate the center peak by subtracting an inteferogram of a matched substrate from the that of the epi-layer. However, this subtraction, while able to extenuate the side-bursts, can not cancel out the main peak completely, since, as shown earlier, the main peak is composed of the epi surface reflections as well as reflections from the epi-substrate interface. In addition, a perfectly matched substrate is impossible to find, and small differences in the substrate doping levels lead to significant subtraction artifacts. In addition to the subtraction technique, several FT-IR manufacturers offer proprietary algorithms of reducing the center peak effects, which are claimed to extend the FT-IR performance to about 0.35 um level. Such claims should be taken with a degree of skepticism, since, even if the center burst is completely eliminated, this still does not account for the frequency responses of the electronic and optical components of FT-IR, nor is the frequency dependence of the epi-substrate reflectivity taken into consideration. These items create phase shifts in the interferogram, which influence the shape and absolute and relative position of the sidebursts. Even in the cases where the film thickness is sufficient for the sideburst identification, these phase shifts cause enough of an error to make film thickness measurements approaching 1 um increasingly uncertain [27-28].

Another important limitation of the interferogram mehod is that it is limited to the thickness determination only. However, an interferogram is a function of and contains information on a number of additional material parameters, such as substrate dopant concentration and profile, scattering rates and mobility, and even surface roughness. By focusing on the side-burst identification, interferogram domain measurements throw this potentially valuable information away.

1.2.3 Spectroscopic Ellipsometry

Spectroscopic Ellipsometry (SE) has traditionally been utilized for non-destructive analysis of

very thin films and multi-layer stacks on a variety of substrates [29-31]. The technique is based on a principle of light changing its state of polarization upon reflection from or transmission through a medium. A typical picture of ellipsometric measurement is presented in Figure 7. Ellipsometry, as applied to thin film analysis, measures two quantities: $tan\Psi$ is the ratio of the amplitudes of the reflected *p* (parallel) and *s* (perpendicular) polarized electric fields; and Δ: the phase difference of the above *p*- and *s*- polarized fields. The combined complex quantity is expressed as

$$\tan \Psi * e^{i\Delta} \qquad (1.2)$$

Spectroscopic ellipsometry has a number of features, which make it very attractive in material analysis:

- As Ψ and Δ are wavelength-dependent functions of the optical properties of the film-substrate system, their measurement over a range of frequencies contains valuable information on both single- and multi- layer film thickness and material composition
- As opposed to the interferometric measurement, ellipsometry directly provides information on real and imaginary portions of the spectrum, without needing to resort to Kramers-Kronig analysis
- SE is inherently a double-beam method, where the measurement is a ratio of two field components. This serves to minimize the extraneous effects of the main electronic and optical components of the instrument[3], as well as account for their polarizing effects
- The change in the phase difference Δ can be detected very accurately, making possible extremely fine thickness measurements (sub-monolayer sensitivity is sometime claimed for dielectric films)

[3] Ratioing will not eliminate these effects completely, since some of these effects are polarization-

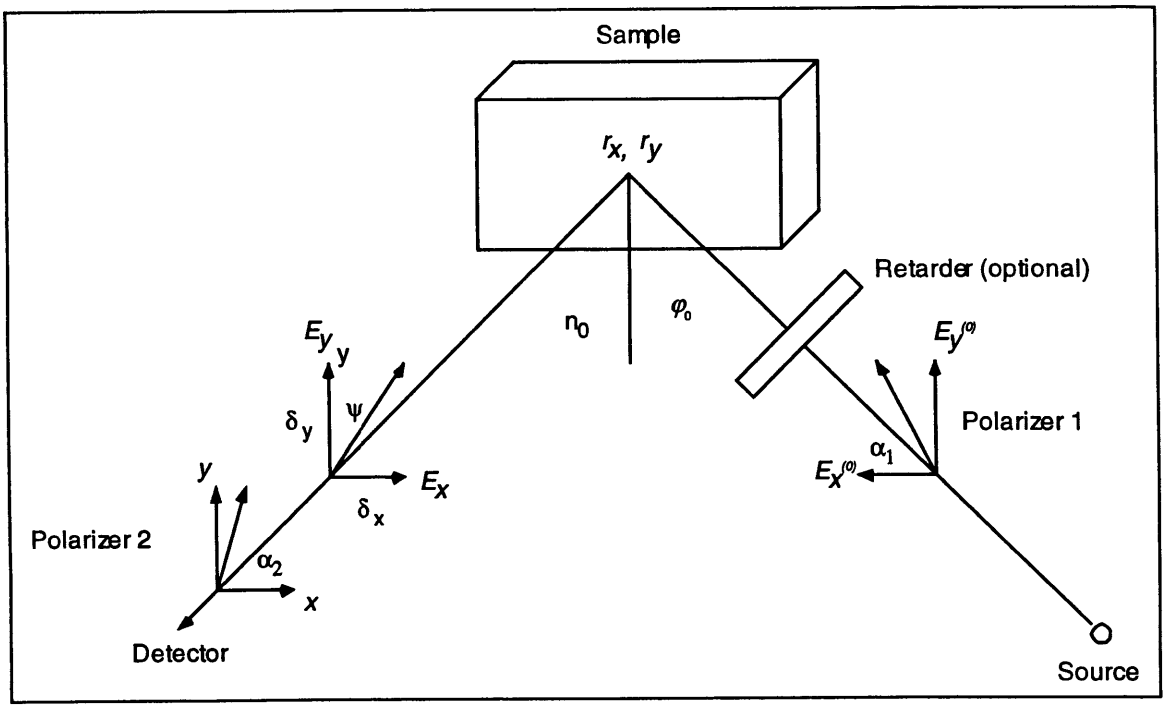

Figure 7: Ellipsometric Measurement Set-up

Despite these advantages, the established SE suffers from main limitation, which makes it unsuitable to silicon epi-layer measurements. Due to the nature of components making up the optical train of the typical spectroscopic ellipsometer system (primarily gratings or prisms used to perform spectral decomposition), SE has been restricted to the UV, visible and near-IR spectral range. Operating in these spectral ranges, SE is unable to detect the optical contrast between the epi-layer and the substrate. Although advantages of doing ellipsometry in the infrared were recognized early enough, SE was not extended into the IR despite some published work in the field [32]. The difficulties lay with relatively low power of the incident radiation (compared with visible and near-IR), as well as ability to make suitable monochromaters for spectral decomposition.

Recently, however, SE in the infrared (will be referred to as IRSE from now on) has taken a significant step forward due to the work of Arnulf Röseler [33-34]. The resulting instrument, a

---

dependant

form of an interferometric ellipsometer, is a combination of the established principles of ellipsometry with FT-IR spectrometry. Although interferometric ellipsometers have been proposed in the 70th [35], the method suffered from precision problems due to the polarization properties of interferometer and possibly the detector, and, therefore, required development of accurate correction, alignment and calibration techniques. For these reasons the interferometric ellipsometry was not adopted in the traditional (near-IR to UV) spectral ranges.

Currently, infrared ellipsometers based on Röseler's principles are available in a few research laboratories around the world. IRSE is a developing technique, whose advantages and limitations are still being understood. As better components, such as IR polarizers and compensators, are developed, and calibration and correction techniques are improved, IRSE could become a valuable tool in material analysis, promising to bring the advantages of spectroscopic ellipsometry to infrared, and, therefore, become a valuable alternative to FT-IR.

Chapter 2.

Linear System Theory of FT-IR

Fourier Transform Infrared Spectrometry has been the subject of a number of books and scientific articles. Most of these, however, have been written by and for practicing material scientists, chemists, and physicists, and focus on spectroscopic studies of various media, and, as such, do not devote much attention to the instrumental abilities and limitations, as well as the signal processing aspects of FT-IR measurements. In the instances where such attention is given, the treatment usually focuses on the frequency domain using monochromatic source as the input, and extending to the polychromatic case through Fourier integral. Thus the stochastic nature of the actual source used in practice is ignored, and the interferogram domain results are presented as rather an afterthought through inverse Fourier transform. On the other hand, the stochastic properties of white light are treated in a number of standard texts on optics. However, this is usually done either in a somewhat qualitative manner, or in the form which does not lend itself

easily to incorporating actual electronic and optical components used in real instruments. The Michelson Interferometer, which forms the heart of the FT-IR instrument, is usually mentioned briefly, and on the qualitative, physical level. Yet, as was stated earlier (Chapter 1.2.2), these components exert undesirable influences on the measurements, and become especially important when the instrument is being pushed to the limit of its resolving ability.

In this chapter we develop the theory of FT-IR measurements from the signal processing point of view. As opposed to the traditional treatment, we begin in the spatial, or, interferogram, domain, and include the stochastic properties of partially coherent light early in the discussion. The treatment is based on the powerful ideas of signal processing designed to deal with problems in communication and information theory. As will be shown, these techniques are directly relevant to the optics and linear transformations of white light, as well as the dispersive properties of the propagation media. This method of treatment also lends itself rather nicely to incorporating the undesirable effects of the optical and electronic components of the instrument, as well as point the way to minimize these influences[4], thereby extending the useful limit of the instrument by several orders of magnitude. This will be done in three parts. In part A) the stochastic source is introduced, and FT-IR with ideal components is considered, where its property as auto-correlator is established. In part B) the parasitic responses of the electronic and optical components are considered, frequency response of the material sample is included, and the overall linear system model of the source/FT-IR/sample is presented. Part C) discusses the limitations caused by these components in the inteferogram mode as well as by the polarization properties of FT-IR, and presents the techniques for overcoming these in the frequency domain. These will be born out by experimental results, illustrating the high resolving ability of the instrument utilized in that manner.

[4] As will be shown, these effects can not be completely removed from the measurements

Linear System Theory of FT-IR

A. FT-IR with Ideal Components

A schematical representation of a typical FT-IR measurement set-up is shown in Figure 8. This picture is a modified version of the schematic shown in Figure 4 in the Introduction, with the sample shifted to the output of the interferometer. While the two versions are equivalent, the latter scheme is more suitable for the purpose of the discussion, allowing uncoupling the properties of the instrument from those of the material sample under investigation.

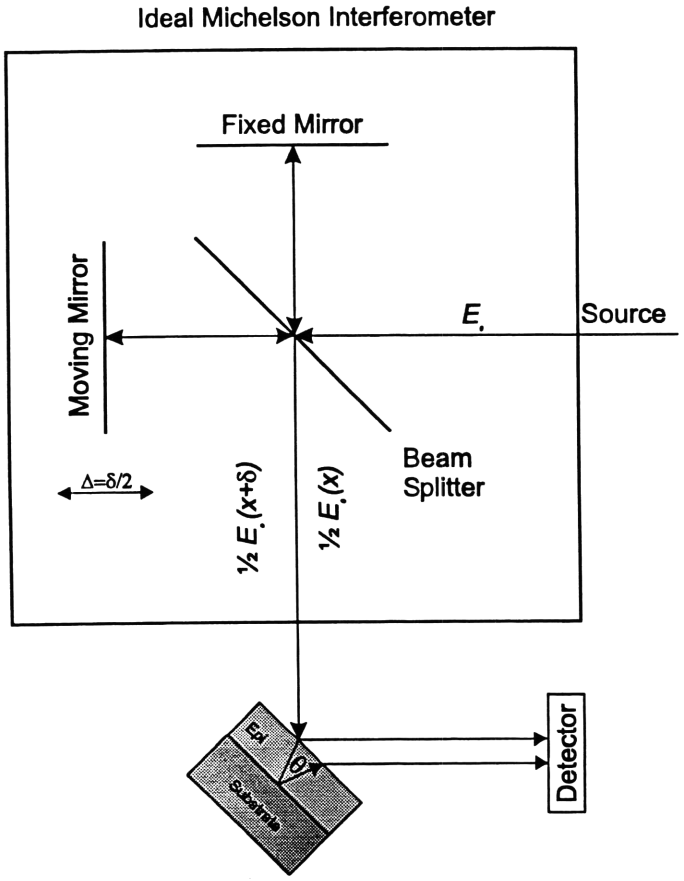

Figure 8 Schematic of FT-IR measurements set-up

The beam splitter of the Michelson interferometer divides the incident electric field $\mathbf{E}_0$ into the components $\mathbf{E}_1$ and $\mathbf{E}_2$. The field component $\mathbf{E}_1$ is reflected off the fixed miror, and the component $\mathbf{E}_2$ is reflected off the moving mirror, which results in the phase shift of 2Δ between the two field components upon the radiation's exit from the interferometer. Here Δ indicates the

position of the moving mirror with respect to its equillibrium point. At $\Delta = 0$ both field components are in phase. Assuming the ideal beamsplitter (non-ideal case is discussed in the next section) the resulting electric field exiting the interferometer is given by

$$\mathbf{E}_t(x) = \mathbf{E}_1(x) + \mathbf{E}_2(x) = \frac{1}{2}\mathbf{E}_0(x) + \frac{1}{2}\mathbf{E}_0(x-\delta) \tag{2.1}$$

where $\delta = 2\Delta$

and the total intensity as the function of displacement is

$$\begin{aligned} I(\delta) &= \left\langle 1/4\left|\mathbf{E}(x) + \mathbf{E}(x-\delta)\right|^2 \right\rangle \\ &= 1/4\left\langle \left|\mathbf{E}(x)\right|^2 + \left|\mathbf{E}(x-\delta)\right|^2 + 2\,\mathrm{Re}\left[\mathbf{E}(x)\mathbf{E}(x-\delta)^*\right] \right\rangle \end{aligned} \tag{2.2}$$

where the angled brackets indicate time averaging.

Statistical Properties of White Light

The chaotic light (also known as stochastic, white, incoherent or partially coherent) can be thought of as resulting from radiation of a number of oscillators at a variety of frequencies whose phases and/or amplitudes are statistically distributed random variables. An example of chaotic light is the gas discharge lamp, where the different atoms are excited by the electronic discharge and emit their radiation independently of one another. The shape of the resulting intensity is a function of the statistical distribution of the atomic velocities and the occurrence of collisions. Other examples of chaotic light include thermal cavity and the filament lamp. The IR source for a typical FTIR, the high temperature cooled ceramic source, is an example of the latter. The mechanisms governing the stochastic behavior of chaotic sources belong to an extended field of study [36-37]. However, the electric field produced by many of these, including the FT-IR source, can be modeled as [37-38]

$$\mathbf{E}_s(x,t) = E_0(t)e^{-j(\omega t - kz - \varphi(t))} \tag{2.3}$$

where the amplitude $E_0(t)$ and the phase $\varphi(t)$ are random processes. One particular example is illustrated in Figure 9 and shows an electric field due to a single atom which undergoes random collisions, where the collision times are Poisson distributed. The amplitude is constant in this case, and the phase after collision is uniformly distributed.

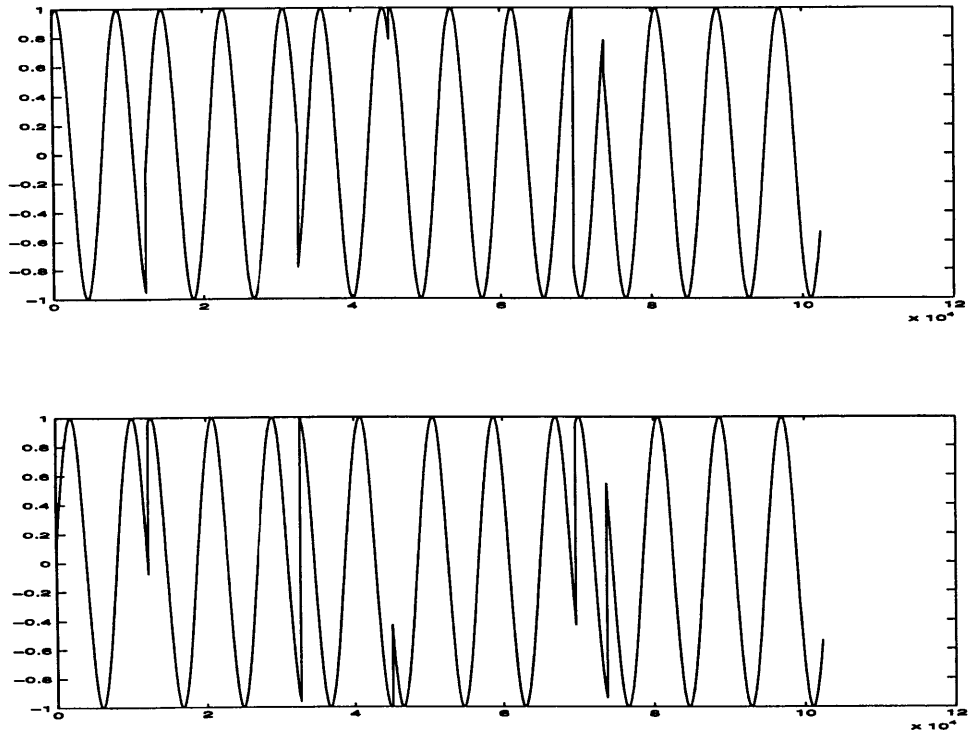

Figure 9: Electric field amplitude of an oscillator experiencing random collisions The two paths illustrate two of infinite possibilities of outcomes. Phase changes are introduced by collisions, and the mean collision time is a measure of the process correlation, or coherence.

The theory of random processes is well-developed and can be looked up in a number of excellent references [39-41]. As a random process, the electric field of a chaotic source is characterized by the joint probability density of all its (complex) values in time:

$$P_{E(t1),E(t2),\ldots,E(tn)}(\mathbf{E}_1,\mathbf{E}_2,\ldots\mathbf{E}_n) \tag{2.4}$$

For the case of white light the items of interest are the process mean

$$m_E(t) = \int \mathbf{E}(t) p_E(\mathbf{E}) d\mathbf{E} \tag{2.5}$$

and covarience (or autocorrelation)[5]

$$\begin{aligned} K_{xx}(t,s) &= \iint X(t)*X^*(s)*p_{x(t),x(s)}(X(t),X(s))dX(t)dX(s) \\ &= \overline{X(t)*X^*(s)} \end{aligned} \tag{2.6}$$

where the overbar indicates statistical averaging. If the operating conditions and the environment in which the source operates do not change with time, or change slowly on the time scale of the measurements, the random process can be classified as *Wide Sense Stationary* (WSS) and *Ergotic*. WSS property means that the mean and covarience are only functions of relative time separation τ, and ergoticity enables to replace statistical averaging with time averaging. Thus Eq. 2.6 can be replaced with

$$K_{EE}(t,s) = K_{EE}(\tau) = \int_{-\infty}^{+\infty} \mathbf{E}(t)\mathbf{E}^*(t-\tau)dt = \left\langle \mathbf{E}(t)\mathbf{E}^*(t-\tau) \right\rangle \tag{2.7}$$

Noting that the time separation τ is equivalent to the spacial separation $\delta = c\tau$, where c is the speed of light in vacuum, and comparing Eq.2.7 with Eq.2.2, it is seen that the first two quantities in the equation 2.2 are equal and constant, and the third quantity is proportional to the real part of the autocorrelation function of the corresponding r.p. In fact, the constant terms in Eq.2.2 are of no particular consequence, and are easily removed from the measurement, leaving only the third term, defined as the interferogram, $I(\delta)$.

Fourier Transformations via Michelson Interferometer: Power Spectral Density

Power Spectral Density of a random process, or $S_{xx}(i\omega)$ is the amount of energy contained in the process at frequency ω. It is also mathematically defined as the varience of the random process when filtered by the bandpass filter whose frequency response $H(j\omega)$ is

$$\begin{aligned} H_\varepsilon(j\omega) &= \sqrt{2\pi/\varepsilon} \quad \text{for } |\omega - \omega_0| < \varepsilon/2 \\ &0 \qquad\qquad \text{otherwise} \end{aligned} \tag{2.8}$$

The connection between the output of the Michelson interferometer in the form of the

[5] Normalized autocorrelation function is sometimes known as *coherence* in optics.

autocorreleation function $K_{EE}(\tau)$, and the frequency spectrum in the form of the power spectral density $S_{EE}(\omega)$ (also known as the spectral intensity $I(j\omega)$) is provided by the Wiener-Khintchine theorem. Wiener-Kinchine theorem states that Power Spectral Density $S_{xx}(j\omega)$ of a WSS process X(t) is the Fourier Transform of its covarience function $K_{xx}(\tau)$:

$$S_{xx}(j\omega) = \int_{+\infty}^{-\infty} K_{xx}(\tau) e^{-j\omega\tau} d\tau \tag{2.9}$$

which is equivalent to

$$S_{EE}(k) = \int_{-\infty}^{+\infty} K_{EE}(\delta) e^{-ik\delta} d\delta \tag{2.10}$$

where the wavevector k is defined as $k = \omega/c$.

As $K_{EE}(\tau)$ is a conjugate-symmetric function, only positive τ need be considered, and Eq.2.10 can be re-written as

$$S_{EE}(\omega) = 2\int_{0}^{+\infty} K_{EE}(\tau) e^{-j\omega\tau} d\tau \tag{2.11}$$

The automatic consequence of the conjugate-symmetry property is that the spectral intensity $I(j\omega)$ is a real quantity, which in turn allows to represent the interferogram as

$$I(\delta) = \frac{1}{4\pi}\int_{-\infty}^{+\infty} I(k)\cos(k\delta) dk \tag{2.12}$$

Therefore the spectral intensity of the IR source is easily obtained from the interferogram $I(\delta)$ by performing a Fourier Transform. It also becomes clear why this technique is called Fourier Transform Infra-Red Spectroscopy: the power spectrum and the interferogram are the Fourier Transform pairs.

Spectral Factorization of the IR Source: Ideal White Noise Process

Thus far the particular spectral shape of the IR source has not been considered. It is expected,

however, that the typical source, such as globar used in FT-IR, would generally resemble the Plank's law for black body radiation [37]:

$$I_t(\omega) = \frac{\hbar\omega^3}{\pi^2 c^3} \frac{1}{\exp(\hbar\omega/k_b T) - 1} \tag{2.13}$$

A plot of $I_t(\omega)$ versus $\hbar\omega/k_b T$ for several values of T is given in Figure 10.

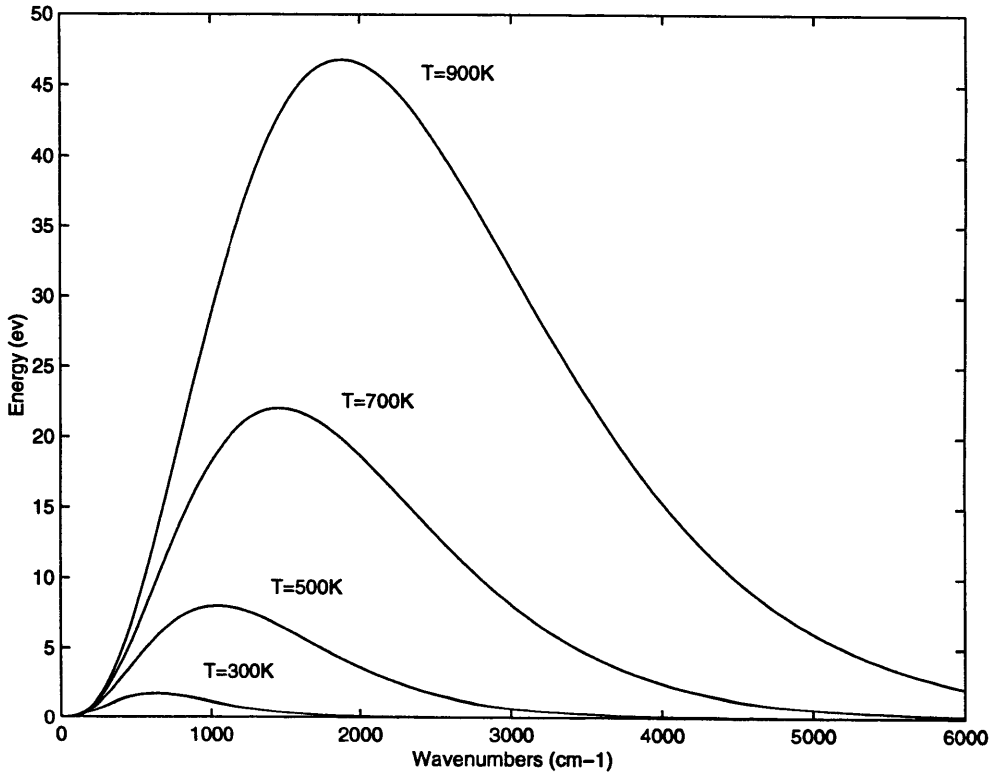

Figure 10: Black Body radiation

This, however, is only an approximation, the exact shape being dependent on the details of the line-broadening processes in the source. Such details could be uncoupled from the otherwise ideal model of FT-IR considered here using the concept of the Ideal White Noise process[6], and applying Paley-Wiener theorem.

[6] White Noise process may also be called White Light in optics, and is a useful model of the electromagnetic field produced by totally incoherent (temporally) source. We shall use White Noise and

A class of processes X(t) is called White Noise process if

$$K_{xx}(\tau) = \delta(\tau) \tag{2.14}$$

where $\delta(\tau)$ is the Dirac delta function. Applying the Wiener-Kinchine theorem, it's easy to see that the Power Spectral Density $S_{xx}(j\omega)$ of a White Noise process is uniform unit amplitude everywhere.

Paley-Wiener theorem allows to represent a WSS process X(t) with a non-uniform S_{xx} as a response of a certain filter $H(j\omega)$ to a White Noise process subject to the constraint

$$\int_{-\infty}^{+\infty} \left| \frac{\ln S_{xx}(j\omega)}{1+(\omega/2\pi)^2} \right| d\omega < \infty \tag{2.15}$$

The filter response $H(j\omega)$ is given by

$$H(j\omega)H(j\omega)^* = |H(j\omega)|^2 = S_{xx}(j\omega) \tag{2.16}$$

The above formalism, known in stochastic signal processing as spectral factorization, is useful as it allows to model the IR source as the output of the filter $H(j\omega)$ driven by the ideal white noise. In particular, the electric field of the IR source in the time domain is given by

$$E_s(t) = \int_{-\infty}^{+\infty} h(t-\tau)E_w(\tau)dt = h(t) \otimes E_w(t) \tag{2.17}$$

where $E_w(t)$ is modeled as the ideal white noise. One needs to bear that the Equation (2.16) does not uniquely determine the particular form of E_w, as there are a number of processes belonging to the *white noise* class (any process whose values in time are uncorrelated with each other). Similarly, the choice of the spectral factor, or system function $H_s(j\omega)$ generally is not unique, either. It can, however, be uniquely determined, if one requires $H_s(j\omega)$ be *minimum phase*[7], thereby restricting it to be causal and stable, and have causal and stable inverse.

White Light terms interchangeably.

[7] Minimum phase system has all its poles and zeros in the left-half plane.

Nevertheless, the technique of spectral factorization will prove to be very useful to the future discussion, as it enables to relegate the spectral properties of the actual source to the system function $H(j\omega)$, and allows to deal with the input to the FT-IR in terms of spectral intensity of white noise, which assumes a particularly simple form:

$$I_w(j\omega) = 1 \tag{2.18}$$

Thus the output of the ideal FT-IR subject to illumination by the non-ideal source is given in the frequency domain as

$$I_d(j\omega) = \left|H_s(j\omega)\right|^2 I_w(j\omega) \tag{2.19}$$

More relevantly, if the magnitude square of $H_s(j\omega)$ can be determined as part of the measurements or the instrument calibration, then the dependence of the measurements on the particular characteristics of the source can be eliminated.

B. FT-IR with Non-ideal Components

Polarization Properties of Coherent Light

Thus far in our discussion of white light we have not considered its polarization properties. As will become apparent shortly, these properties, and particularly the influence of the main components of FT-IR on them, bare important implications for the measurements, and need to be addressed. Consider the incidence of plane wave as may emerge from the output of FT-IR on the surface of the sample, illustrated in Figure 7. The electric field vector $\boldsymbol{E}$ can be resolved into two orthogonal components defined with respect to the plane of incidence: $\boldsymbol{E}_x$, or *p*-polarized is oriented parallel to the plane, and $\boldsymbol{E}_y$, or *s*-polarized, is oriented perpendicular to the plane. State of polarization for *monochromatic* wave refers to the shape which the tip of the electric field vector $\boldsymbol{E}$ will trace on the plane perpendicular to the direction of propagation, and is defined by the phase difference between the two field components and their amplitudes. Let the electric field vector $\boldsymbol{E}$ be given as

$$\mathbf{E} = \mathbf{E}_0 e^{j(\tau-\delta)} \tag{2.20}$$

where $\tau = kz - \omega t$, and δ is initial phase. Then the real field components are given as

$$E_x = E_{0x}\cos(\tau - \delta_x) \tag{2.21}$$

$$E_y = E_{0y}\cos(\tau - \delta_y) \tag{2.22}$$

We rewrite the equation by expanding and normalizing as

$$\frac{E_x}{E_{0x}} = \cos\tau\cos\delta_x + \sin\tau\sin\delta_x \tag{2.23}$$

$$\frac{E_y}{E_{0y}} = \cos\tau\cos\delta_y + \sin\tau\sin\delta_y \tag{2.24}$$

We can eliminate the phasor argument τ by further re-writing the equations as

$$\frac{E_x}{E_{0x}}\sin\delta_y - \frac{E_y}{E_{0y}}\sin\delta_x = -\cos\tau\sin(\delta_x - \delta_y) \tag{2.25}$$

$$\frac{E_x}{E_{0x}}\cos\delta_y - \frac{E_y}{E_{0y}}\cos\delta_x = \sin\tau\sin(\delta_x - \delta_y) \tag{2.26}$$

and squaring and adding, obtaining

$$\frac{E_x^{\,2}}{E_{0x}^{\,2}} + \frac{E_y^{\,2}}{E_{0y}^{\,2}} - 2\frac{E_x E_y}{E_{0x}E_{0y}}\cos\Delta = \sin^2\Delta \tag{2.27}$$

where $\Delta = \delta_x - \delta_y$.

The expression 2.27 describes an ellipse, whose major and minor axis are rotated by an angle θ with respect to the coordinate axes. This becomes apparent if one considers the picture shown in Figure 11.

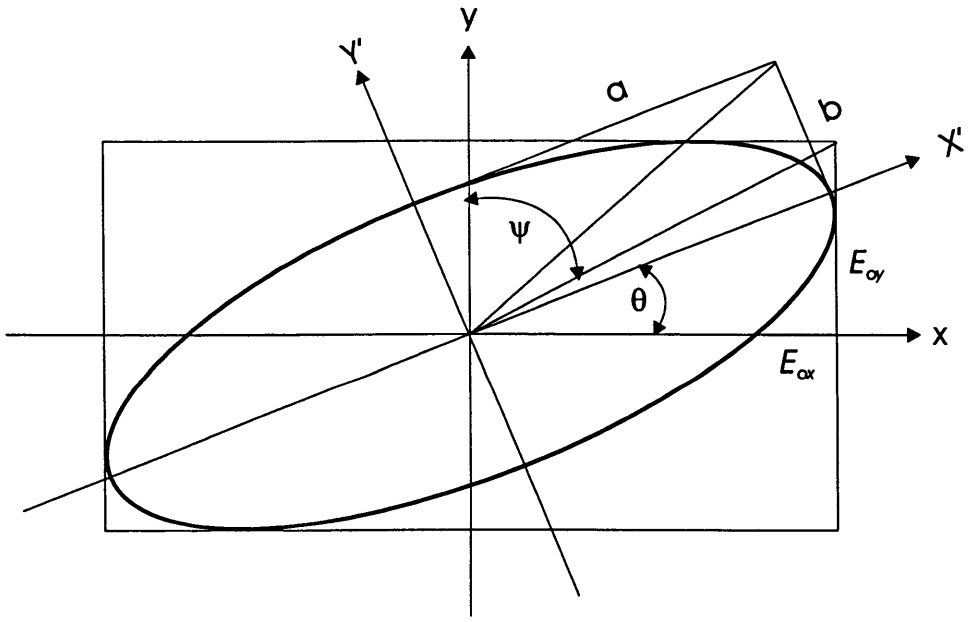

Figure 11: Coordinate Transformation of Polarization Ellipse

A baseline ellipse described in terms of the system **X** and oriented along the main axes as

$$\frac{E_x^{\,2}}{a^2} + \frac{E_y^{\,2}}{b^2} = 1 \tag{2.28}$$

may be rotated by an angle θ through the following transformation:

$$\begin{bmatrix} x' \\ y' \end{bmatrix} = \begin{bmatrix} \cos\theta & \sin\theta \\ -\sin\theta & \cos\theta \end{bmatrix} \begin{bmatrix} x \\ y \end{bmatrix} \tag{2.29}$$

which produces the following expression for the rotated ellipse:

$$E_x^2\left[\frac{\cos^2\theta}{a^2}+\frac{\sin^2\theta}{b^2}\right]+E_y^2\left[\frac{\sin^2\theta}{a^2}+\frac{\cos^2\theta}{b^2}\right]-2E_xE_y\sin\theta\cos\theta\left[\frac{1}{b^2}-\frac{1}{a^2}\right]=1 \tag{2.30}$$

Comparing the equations 2.27 and 2.30, the following identities are obtained:

$$a^2+b^2 = E_{0x}{}^2 + E_{0y}{}^2 \tag{2.30a}$$

$$(a^2-b^2)\cos 2\theta = E_{0x}{}^2 - E_{0y}{}^2 \tag{2.30b}$$

$$(a^2-b^2)\sin 2\theta = 2E_{0x}E_{0y}\cos\Delta \tag{2.30c}$$

$$ab = E_{0x}E_{0y}\sin\Delta \tag{2.30d}$$

Defining the ellipsometric parameter Ψ as

$$\tan\psi = \frac{E_x}{E_y} \tag{2.31}$$

equations 2.30 b,c produce

$$\tan 2\theta = -\tan 2\psi\cos\Delta \tag{2.32}$$

The two special cases of polarization are:

a) $\Delta = 0$ produces linearly polarized light oriented at $\theta = 90° - \psi$

b) $\Delta = \pm\pi/2$ produces elliptical polarization oriented along the main coordinate system, which becomes circular in the case of $a=b$.

Polarization Properties of Stochastic Light

As the state of polarization implies a definite phase relationship between the *s*- and *p*-components of the electric field, *monochromatic, or coherent, light is always polarized.*

On the other hand, incoherent, or white, light may have the degree of polarization which varies

from 100% polarized to totally unpolarized, and anything in between. Mathematically, we may describe polarization properties of white light using the quantity known as cross-correlation, and covariance matrix.

Let X and Y be (complex) scalar random processes. The cross-correlation function $K_{xy}(t,s)$ is defined

$$\begin{aligned} K_{xy}(t,s) &= \iint X(t)*Y^*(s)*p_{x(t),y(s)}(X(t),Y(s))dX(t)dY(s) \\ &= \overline{X(t)*Y^*(s)} \end{aligned} \tag{2.33}$$

where $p_{x(t),y(s)}(X(t),Y(s))$ is the joint probability density for X and Y.

We can transform to the frequency domain through

$$S_{xy}(j\omega) = \int_{+\infty}^{-\infty} K_{xy}(\tau)e^{-j\omega\tau}d\tau \tag{2.34}$$

Covariance matrix is the vector analogue of the autocorrelation function. Let $\boldsymbol{X}(t)$ be a (complex) vector quantity. Then covariance matrix $K_{XX}(\tau)$ is given as a cross product

$$K_{XX}(\tau) = \overline{\mathbf{X}(t)\mathbf{X}^*(t-\tau)^T} \tag{2.35}$$

More specifically, let $$\mathbf{E}(t) = \begin{pmatrix} E_x(t) \\ E_y(t) \end{pmatrix}$$

Then covariance matrix for $\boldsymbol{E}$ is given by

$$\mathbf{J}(\tau) = \begin{pmatrix} K_{E_xE_x} & K_{E_xE_y} \\ K_{E_yE_x} & K_{E_yE_y} \end{pmatrix} \tag{2.36}$$

The polarization properties of **E** are given by **J**, which holds for both monochromatic (coherent) and stochastic case. For example, the state of polarization for the coherent light is given as

$$\mathbf{J}(\omega) = \begin{pmatrix} E^2{}_{0x} & E_{0x}E_{0y}e^{i\Delta} \\ E_{0x}E_{0y}e^{-i\Delta} & E^2{}_{0y} \end{pmatrix} \tag{2.37}$$

The matrix **J** is known as the Jones matrix. We can see that the covarience matrix is Hermitian, and

$$Det(\mathbf{J}) = 0 \tag{2.38}$$

Particularly, the Equation 2.38 can serve to specify completely polarized light.

The intensity of the radiation is given as

$$I(j\omega) = Trace(\mathbf{J}) \tag{2.39}$$

For the totally unpolarized incoherent light the matrix is

$$\mathbf{J} = J_0 \begin{pmatrix} 1 & 0 \\ 0 & 1 \end{pmatrix} \tag{2.40}$$

Unpolarized light has the property that its x and y components are equal in magnitude and uncorrelated with each other. Physically this translates in the property that the light intensity along any direction perpendicular to the propagation vector is the same. Unpolarized light is sometimes referred to as *natural light.*

In between the two (ideal) extremes of completely polarized and completely unpolarized light lies the real-world case of partial polarization. Partially polarized light is still characterized by a covariance (Jones) matrix, but it no longer satisfies the conditions 2.37 , 2.28, or 2.40.

However, the covariance matrix $\mathbf{J}$ of a partially polarized light wave can always be uniquely represented as a sum of covariances of two *independent* waves, one of which is totally polarized, and the other is totally unpolarized [26][8].

$$\mathbf{J} = \mathbf{J}^P + \mathbf{J}^u \tag{2.41}$$

where $\mathbf{J}^P$ satisfies 2.37-38 and $\mathbf{J}^U$ satisfies 2.40. If $\mathbf{J}^P$ and $\mathbf{J}^U$ are given as

$$\mathbf{J}^P = \begin{pmatrix} B & D \\ D^* & C \end{pmatrix} \text{ and } \mathbf{J}^U = \begin{pmatrix} A & 0 \\ 0 & A \end{pmatrix} \tag{2.42}$$

then their components are given by

[8] Variance of the sum of two independent (or uncorrelated) random variables is equal to the sum of their variances. Same holds when one of the two is a deterministic variable.

$$A = \frac{1}{2}(J_{xx} + J_{yy}) - \frac{1}{2}\sqrt{(J_{xx} + J_{yy})^2 - 4|\mathbf{J}|} \tag{2.43a}$$

$$B = \frac{1}{2}(J_{xx} - J_{yy}) + \frac{1}{2}\sqrt{(J_{xx} + J_{yy})^2 - 4|\mathbf{J}|} \tag{2.43b}$$

$$C = -\frac{1}{2}(J_{xx} + J_{yy}) + \frac{1}{2}\sqrt{(J_{xx} + J_{yy})^2 - 4|\mathbf{J}|} \tag{2.43c}$$

$$D = J_{xy}, \quad D^* = J_{yx} \tag{2.43d}$$

where J_{ij} are the components of $\mathbf{J}$ and $|\mathbf{J}| = Det(\mathbf{J})$.

The degree of polarization P is defined as the ratio of the intensity of the polarized component of the total wave to the total intensity.

$$I_{tot} = J_{xx} + J_{yy} \tag{2.44}$$

$$I_{pol} = B + C = \sqrt{(J_{xx} + J_{yy})^2 - 4|\mathbf{J}|} \tag{2.45}$$

and P is given as

$$P = \sqrt{1 - \frac{4|\mathbf{J}|}{(J_{xx} + J_{yy})^2}} \tag{2.46}$$

It is easy to see that for totally unpolarized wave P = 0, and for totally polarized wave P = 1. Also, if the two electric field components are totally uncorrelated (J_{xy}=0), but $J_{xx} \neq J_{yy}$, the degree of polarization is given by

$$P = \left| \frac{J_{xx} - J_{yy}}{J_{xx} + J_{yy}} \right| \tag{2.47}$$

The importance of polarization for FT-IR measurements arises from the fact that the reflectivity of a typical material being investigated is a function of the polarization state of the incident light beam. This can be seen in the Figure 12, which shows reflectivity of heavily doped Si substrate for *s*- and *p*- polarized field components. Thus in order to be able to accurately model the total intensity reflected from the sample, the degree of polarization of the light impinging on the sample must be known. Even assuming that the initial beam emitted from the source is unpolarized (which may not be completely true), the beam at the output of FT-IR emerges

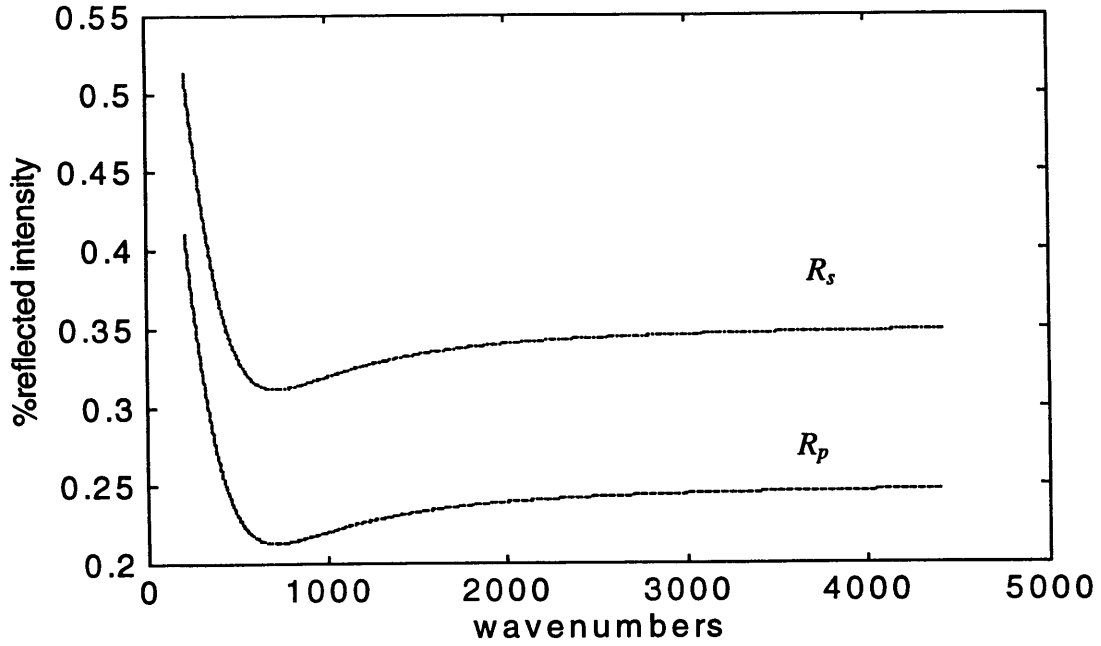

Figure 12 Reflectance spectrum from doped silicon substrate for *s*- and *p*- polarized components

partially polarized, due mainly to the properties of the beam splitter.

The beam splitter is one of the most important components of FT-IR and one that bares a considerable influence on its performance [25][9]. Although several types are available, a typical IR beam splitter can be modeled as a dielectric film characterized by its reflectivity and transmissivity *R* and *T*. As these differ for *s*- and *p*- polarizations, the effect of the beam splitter is to weigh the original beam by the respective *s*- and *p*- factors, thus changing its polarization properties.[10] The techniques for determining the polarizing properties of FT-IR will be dealt with in the section on minimizing the effects of non-idealities.

[9] Polarizing properties of beam splitter will be dealt with in more depth in the Chapter on IR ellipsometry.

[10] These are frequency-dependant quantities due to the dispersive nature of the index of refraction of the beam splitter.

Linear System Model of FT-IR with Non-ideal Components

The non-ideal components of FT-IR can be broken down in two categories: polarization-dependent and independent. Such components as mirrors and detector[11] can be assigned to the polarization-independent group. On the other hand, the effects of the beam splitter and the material sample to be measured are strongly polarization dependent, and must be modeled according to the polarization state of the incident radiation. The effects of these non-idealities can be accounted for by treating them as transformations of stochastic processes through linear system.

Let **X**(t) be (complex) stochastic process, applied as an input to a linear system characterized by an impulse response $h(t)$. Then the output of the system is a stochastic process **Y**(t) given by

$$Y(t) = \int_{-\infty}^{+\infty} h(t,\tau)X(\tau)d\tau \tag{2.48}$$

whose covariance $K_{yy}(t,s)$ is given by

$$K_{yy}(t,s) = \int_{-\infty-\infty}^{+\infty+\infty} h(t,\tau)h(s,k)K_{xx}(\tau,k)d\tau dk \tag{2.49}$$

In the case of wide-sense stationary (WSS) stochastic process, and linear time invariant system (LTI), the argument t,s is replaced by $\tau = t\text{-}s$. Applying the Wiener-Khintchine theorem to 2.49 through Fourier transformation, the frequency domain expression is obtained

$$S_{yy}(j\omega) = H(j\omega)H^*(j\omega)S_{xx}(j\omega) = \left|H(j\omega)\right|^2 S_{xx}(j\omega) \tag{2.50}$$

Let H_d be the system function of the detector, H_m the system function of the rest of polarization-independent components of the FT-IR, and $H_{bls,p}$ and $R_{s,p}$ the polarization-dependent system functions of the beam splitter and material, where the subscripts s and p denote perpendicular and parallel components of the incident radiation. Then applying (2.50) to each individual component,

and recalling results from spectral factorization, the output of the FT-IR with non-ideal components can be represented as

$$I_d(\omega) = I_w(\omega)\left|H_s(j\omega)\right|^2\left|H_m(j\omega)\right|^2 H_d(j\omega)\{\left|H_{bls}(j\omega)\right|^2 R_s(j\omega) + \left|H_{blp}(j\omega)\right|^2 R_p(j\omega)\} \quad (2.51)$$

where $I_w(\omega)$ is the spectral intensity of the ideal white noise process[12]. This process is shown graphically in Figure 13 below.

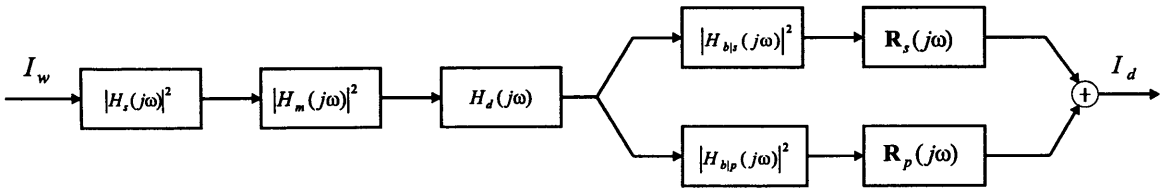

Figure 13: Linear system of FT-IR/Epi-substrate : Block Diagram

C. Minimizing the Effects of Non-idealities: Reflectance Mode Measurements

Examining Equation 2.51, it is seen that a typical interferogram as shown in Figures 5 and 6 has a fairly complicated shape which is the result of the product of the frequency responses of the optical and electronic components of the FT-IR as well as the spectral characteristics of the light source and the material being measured, which in the interferogram domain are convolved together. As the parasitic system functions due to the FT-IR non-idealities can not be known with certainty, and, indeed, exhibit considerable variations from one instrument to another, their effects must be either eliminated or reduced to a minimum. This can be done by switching from the spatial, or interferogram mode to the frequency domain and ratioing the overall intensity as

---

[11] In some cases, detector may exhibit polarization-dependant properties.

[12] This assumes that the light emitted from the source is unpolarized. In the case the light is partially polarized, its polarization properties may be absorbed into the system functions of the beam splitter.

given by Equation 2.51 to that produced by a highly conducting gold mirror. An example of such reference spectrum is shown in Figure 14. It can be contrasted to the idealized picture of black-body radiation as shown in Figure 10, and illustrates the effect of the real components on the typical measurement. Assuming ideal reference mirror, the product of such measurement, also known as *reflectance*, and denoted by $\mathbf{R}(j\omega)$, is given by

$$\mathbf{R}(j\omega) = \frac{I_d(j\omega)}{I_{gold}(j\omega)} = \frac{\left|H_{bs}(j\omega)\right|^2 R_s(j\omega) + \left|H_{bp}(j\omega)\right|^2 R_p(j\omega)}{\left|H_{bs}(j\omega)\right|^2 + \left|H_{bp}(j\omega)\right|^2} \tag{2.52}$$

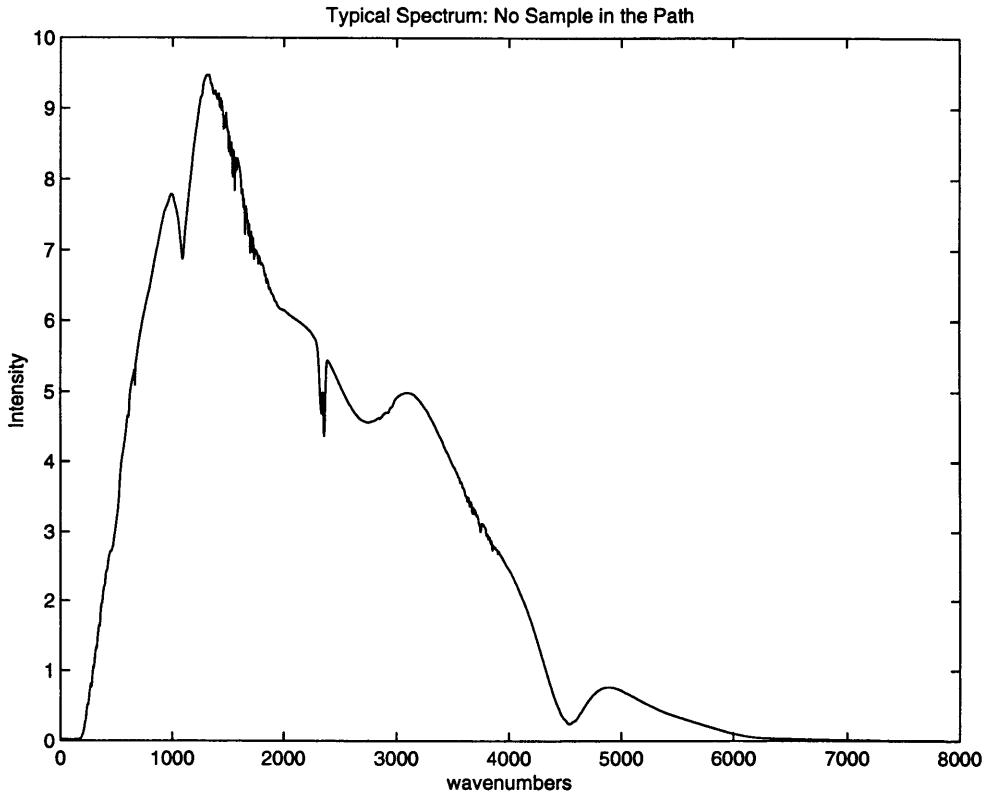

Figure 14: Reference Spectrum

Equation 2.52 shows that reflectance mode does not completely eliminate the impact of FT-IR non-idealities. However, reducing such impact to the singular dependence on the characteristics of the beam splitter makes possible to account for the residual effects. More specifically, this can be done by defining a pair of parameterized frequency-dependent functions $\xi(\alpha,\beta)$ and $\zeta(\alpha,\beta)$

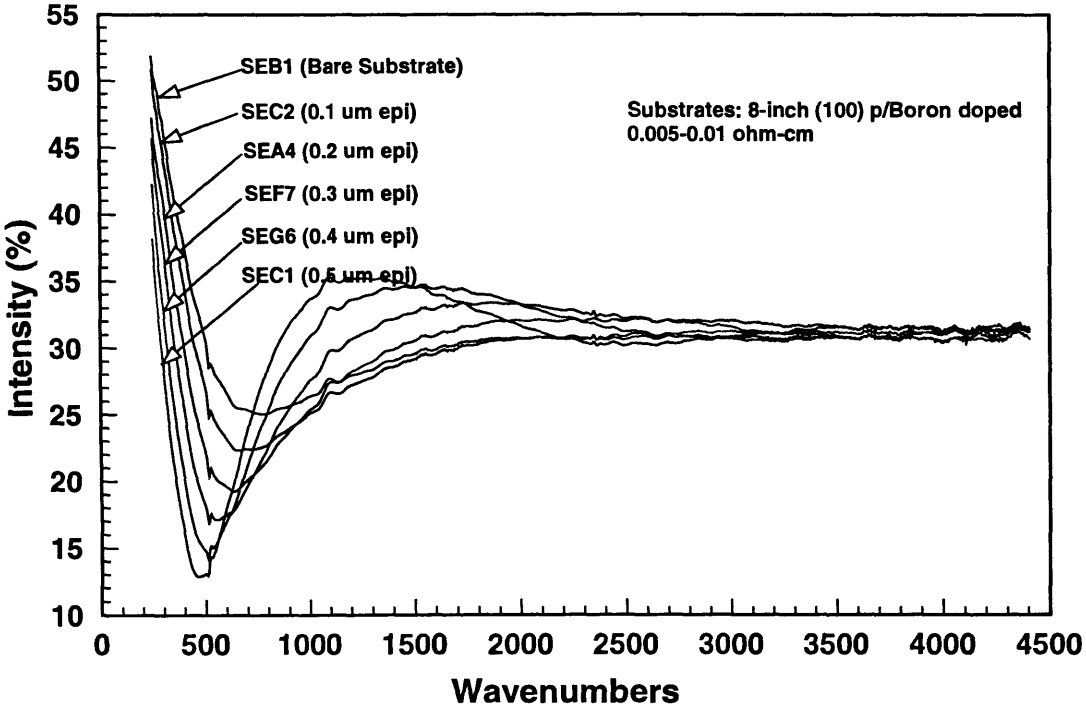

Figure 15: Reflectance spectra of thin epi-layers: Batch 1

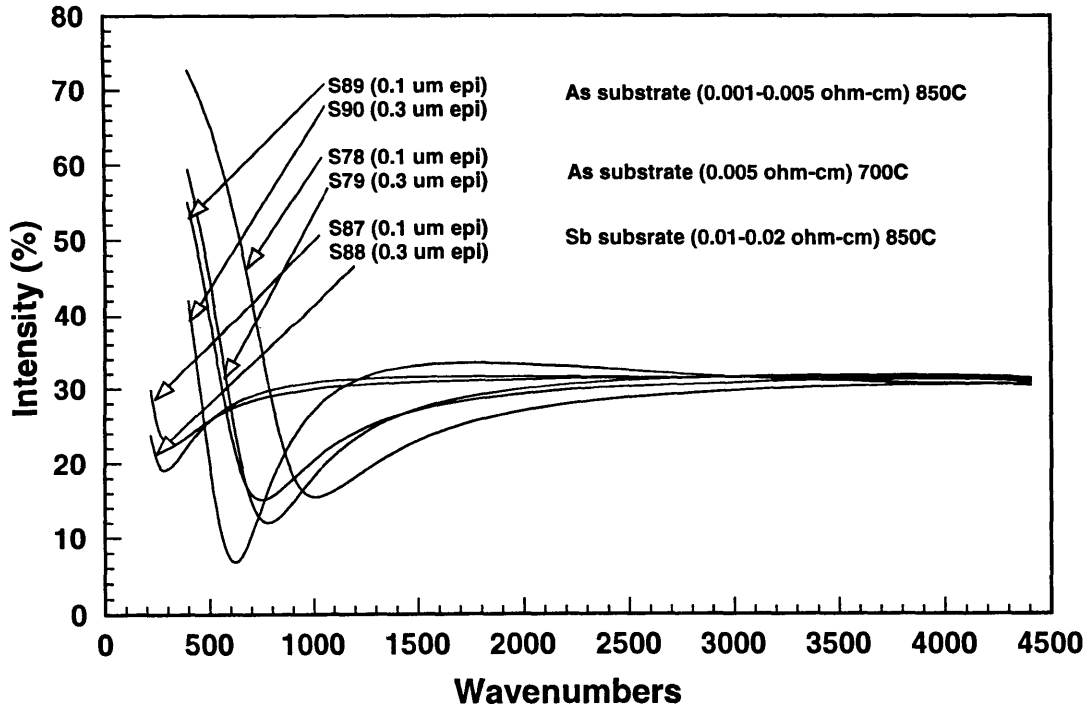

Figure 16: Reflectance spectra of thin epi-layers: Batch 2

containing the beam splitter characteristics, with the actual values α,β to be determined during the data analysis stage (see Chapter 4). Figure 15 and Figure 16 present results of reflectance measurements performed on several batches of thin epitaxial films grown on boron, arsenic and antimony susbstrates. The resolving ability of FT-IR in this mode is clearly illustrated.

Chapter 3.

Silicon Epitaxial Films in the Infrared

3.1 Introduction

In the previous chapter it was shown that the combined FT-IR/epi-substrate system can be viewed without loss of information as a linear system driven by the ideal white noise process, where the linear system is composed of the frequency responses of the electronic and optical components of the FTIR such as the source, mirrors, beam splitter, and the detector, as well as frequency response of the epi-substrate due to the frequency-dependent nature of the silicon optical constants in the infra-red. By utilizing FT-IR in the frequency mode, the effects of FT-IR non-idealities have been reduced to the dependence on the characteristics of the beam splitter, which, as will be shown later, can be accounted for during the data analysis stage. Thus we have achieved the goal of uncoupling the measurements from the characteristics of the instrument, making them dependent only on the material properties contained in the frequency-dependent quantities R_s and R_p, which contain the information on the film thickness. In the frequency, or reflectance, mode we no longer determine the film thickness by observing the peaks of the interferogram. Rather, we will depend on having sufficiently accurate parameterized model of

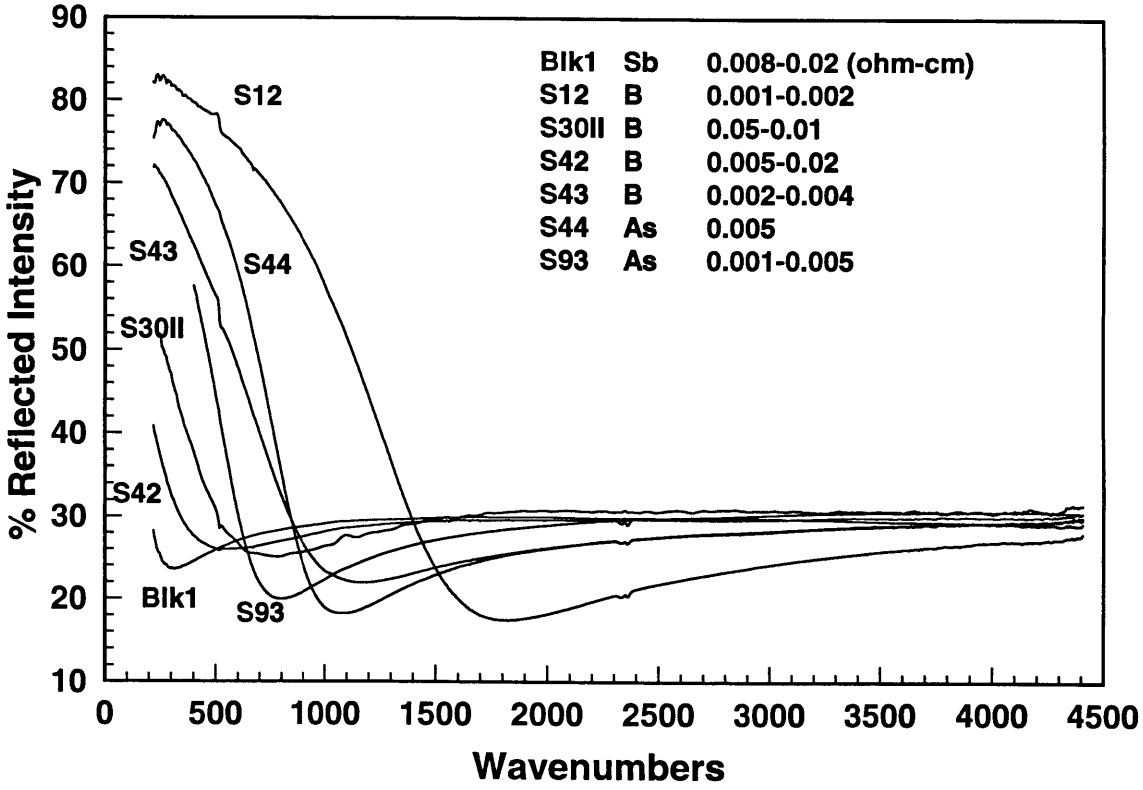

Figure 17 Reflectance spectra of doped substrates

reflectance from the epi-substrate and perform parameter optimization against experimental reflectance to determine the quantities of interest. This is clearly more involved than simply observing the peaks. However, the advantages of this method are obvious, as we no longer limited by the instrument imperfections and therefore can detect much thinner films than possible with conventional FTIR methods. In addition, frequency domain measurements are able to provide more information than just film thickness. Figure 17 displays reflectance measurements taken from a variety of substrates of different types and concentrations. As can be seen from these results, frequency domain measurements are quite sensitive to the type of dopants and their concentrations, therefore enabling one to non-destructively determine substrate resistivity. In addition, as will be shown, reflectance measurements are sensitive to the thickness and shape of the transition layer, which is invariably present between the epitaxial film and substrate. All this

makes possible simultaneous determination of these quantities from a single measurement[13], provided the existence of a suitable parameterized model of reflectance.

In this chapter, the parameterized model of epi/substrate reflectance is derived. This is done in two steps. First, the epi-layer-substrate model is constructed as either an abrupt two-layer structure or as a finite element structure taking into account the presence of a gradual transition layer between the epi-layer and the substrate. Then the dielectric function of doped silicon is obtained via the classical Drude model. The predictions of the Drude model are compared with experimentally determined results.

[13] As will be shown, certain conditions must be satisfied for the dopant profile to be determined.

3.2 Complex Maxwell Equations and Complex Index of Refraction

The complex Maxwell equations for the case of linear media are presented below [42]:

$$\begin{aligned} \nabla \times \mathbf{E} &= -j\omega\mu\mathbf{H} \\ \nabla \times \mathbf{H} &= j\omega\varepsilon\mathbf{E} + \mathbf{J} \\ \nabla \bullet \varepsilon\mathbf{E} &= \rho \\ \nabla \bullet \mu\mathbf{H} &= \mathbf{0} \end{aligned} \tag{3.1}$$

These can be combined in the wave equation:

$$\nabla^2\mathbf{E} = \omega^2\mu\varepsilon\mathbf{E} \tag{3.2}$$

The solution of the equation is a monochromatic wave:

$$\Psi(\mathbf{r},t) = \mathbf{A}e^{j(\omega t - \mathbf{k}\cdot\mathbf{r})}$$

where $\boldsymbol{k}$ is the wave vector, $\boldsymbol{r}$ is the coordinate vector, ω is the angular frequency, ε is the polarization, and μ is permittivity. One defines c the speed of light in medium as ω/k.

From the wave equation

$$c = \omega/k = 1/\sqrt{\mu\varepsilon} \tag{3.3}$$

One defines $\boldsymbol{n}$ the complex index of refraction as the ratio of the speed of light in the vacuum to that in the medium. Thus in vacuum, $\boldsymbol{n}$ is real and unity. The complex refractive index $\boldsymbol{n}$ can be written as

$$\mathbf{n} = n - ik \tag{3.4}$$

where n is the refractive index and k is the extinction coefficient. The are usually frequency dependent quantities.

3.3 Epi/Substrate System as an Abrupt Model

The schematic of the abrupt profile is shown in Figure 18. The layer of SiO_2 is shown for accuracy, as a thin native oxide layer of 10-20 Å is typically present on the surface of the epi-layer. As will be shown later, due to the long wavelength of the infrared radiation (2.5 – 40 μm) and relatively low optical contrast of the SiO_2 – Si interface, it need not be included in the modeling.

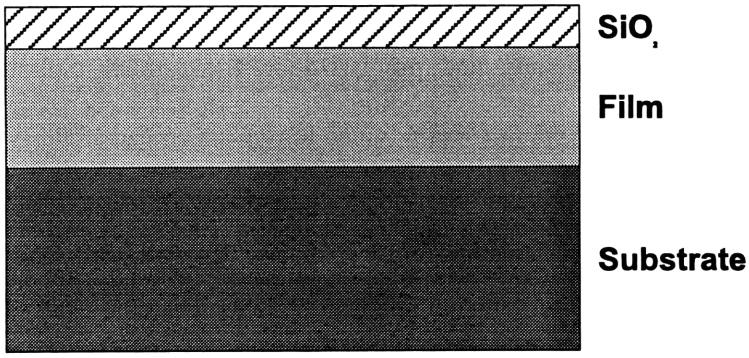

Figure 18: Abrupt Profile Model

The subject of reflection and transmission of EM waves in a layered media is treated in a number of books [43-44]. The optical characteristics of the two-layer structure as shown in Figure 19 are frequently defined in terms of the Fresnel reflection and transmission coefficients.

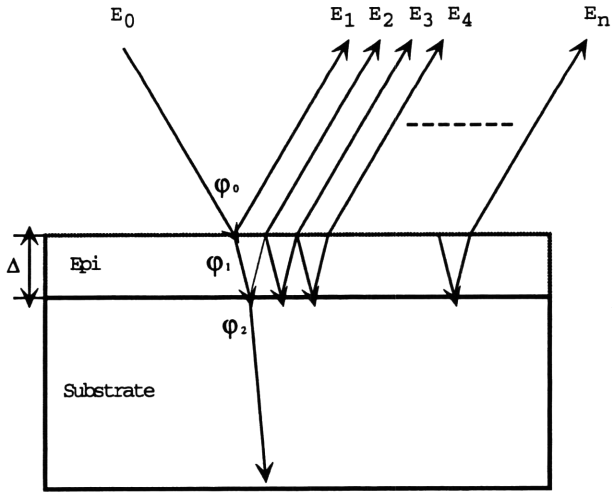

Figure 19: Reflection from a thin film structure

Let n_0, n_1, and n_2 be the corresponding indexes of refraction in the air, epi, and substrate, and φ_0, φ_1, φ_2 be their (complex) angles of incidence/refraction. The Fresnel reflection coefficient r_{jk} is defined as the ratio (complex) of the reflected electric field from the media k to the incident in the media j. Like wise, the Fresnel transmission coefficient t_{jk} is defined as the ration of the transmitted electric field in the media k to the incident in the media j. The overall Fresnel reflection coefficient r is the ratio in the reflected electric field from the overall epi-substrate system to the incident. In addition, the field polarizations must be considered as well. S-polarization stands for perpendicular, and p-polarization for parallel. Solving the Maxwell equations with the corresponding boundary conditions for the air-epi-substrate system, we get the following expressions for the overall Fresnel reflection coefficient R:

$$r_p = \frac{r_{01p} + r_{12p}e^{-j2\beta}}{1 + r_{01p}r_{12p}e^{-j2\beta}} \tag{3.5a}$$

$$r_s = \frac{r_{01s} + r_{12s}e^{-j2\beta}}{1 + r_{01s}r_{12s}e^{-j2\beta}} \tag{3.5b}$$

$$r_{01p} = \frac{n_1 \cos\varphi_0 - n_0 \cos\varphi_1}{n_1 \cos\varphi_0 + n_0 \cos\varphi_1} \tag{3.5c}$$

$$r_{12p} = \frac{n_2 \cos\varphi_1 - n_1 \cos\varphi_2}{n_2 \cos\varphi_1 + n_1 \cos\varphi_2} \tag{3.5d}$$

$$r_{01s} = \frac{n_0 \cos\varphi_0 - n_1 \cos\varphi_1}{n_0 \cos\varphi_0 + n_1 \cos\varphi_1} \tag{3.5e}$$

$$r_{12s} = \frac{n_1 \cos\varphi_1 - n_2 \cos\varphi_2}{n_1 \cos\varphi_1 + n_2 \cos\varphi_2} \tag{3.5f}$$

where $$\beta = 2\pi\left(\frac{\Delta}{\lambda}\right)(n_1^2 - n_0^2 \sin^2\varphi_0)^{1/2} \tag{3.5g}$$

is the phase difference between the incident and reflected waves due to the wave travelling in the film.

The overall system functions R_s and R_p are given as

$$R_s = r_s r_s^*$$
$$R_p = r_p r_p^* \tag{3.6}$$

and the parameterized reflectance model is given as

$$\mathbf{R}_{tot} = R_s \xi(\alpha,\beta) + R_p \varsigma(\alpha,\beta) \tag{3.7}$$

with parameters α and β to be determined during the data analysis process (see Chapter 4). Figure 20 shows simulated reflectance waveforms for several epi-substrate systems.

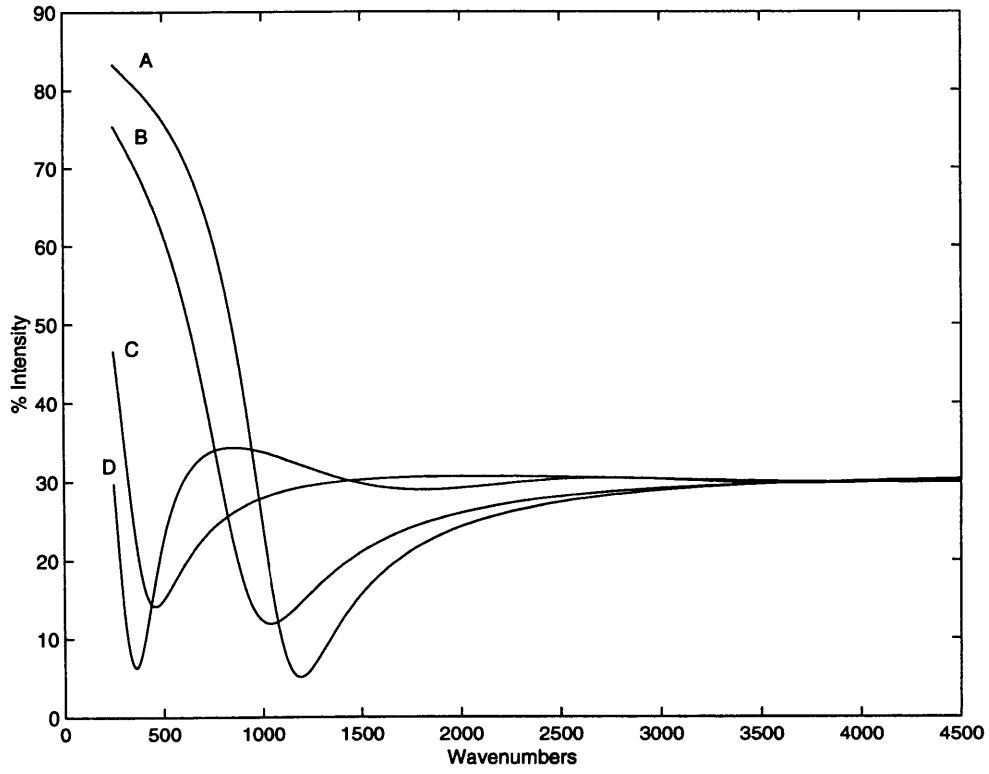

Figure 20 Reflectance characteristics of various epi-substrate structures

3.4 Modeling the Transition Layer Profile

The term *transition layer* in silicon epitaxy is used when referring to the intermediate region between the substrate and epitaxial layer. Such region, as shown in Figure 21, invariably exists in epitaxial structures, and is mainly due to the effects of autodoping. Autodoping refers to the

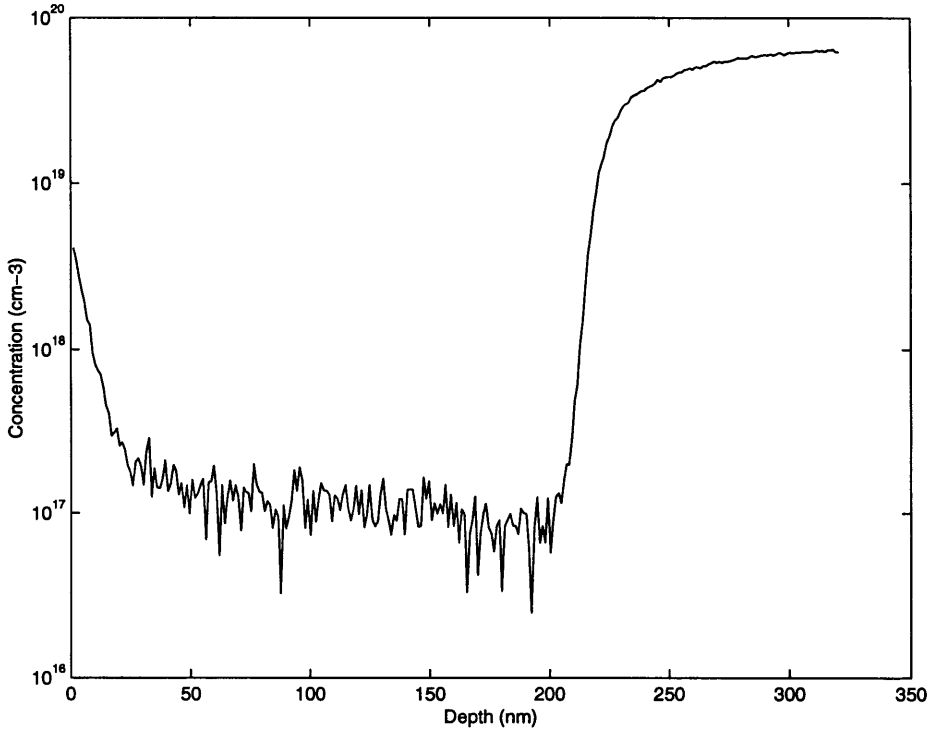

Figure 21 SIMS data for sample S52

process via which the dopants from the substrate are transferred to the epitaxial layer during deposition. This process, first discovered in 1961, has been the subject of extensive studies due to its importance in the emerging bipolar transistor technology. An extensive review of the autodoping effects in silicon epitaxy was performed by Srinivasan [45]. According to Srinivasan, the typical transition layer profile can be resolved into two regions. The region A close to the substrate-epitaxy interface is the result of solid-state out-diffusion of the dopants from the substrate. The region B, the so-called auto-doping tail, is caused by the dopant transport in the vapor phase. The commonly accepted model of the region A is based on the solution of one-dimensional linear diffusion equation by Grove *et al.* [46]. Grove solution simplifies to the complementary error function

$$C(x,t) = C_s erfc(\frac{x}{2\sqrt{Dt}}) \tag{3.8}$$

provided that

$$vt > 2\sqrt{Dt}$$

where v is the epitaxial growth rate, D is the substrate dopant diffusion constant, and t is the growth time.

Grossman [47] obtained an expression for region B by assuming that the dopant vapor reincorporates into the epitaxy with a rate which is proportional to the deposition rate and the concentration at the surface. Grossman expression for the autodoping tail is given by

$$C = C_0 e^{-\alpha KZ} \tag{3.10}$$

where K is the redistribution coefficient between the solid and the absorbed phase, Z is the epi-layer thickness, and α is a constant.

In practice, the particular shape of the transition layer is determined by a number of factors including the processing conditions such as growth temperature, pressure and deposition rate, substrate characteristics, pre-bake cycle, and the features of the reactor.

In order to calculate the reflectance characteristics of epi-substrate system utilizing the transition layer, an optical model shown in Figure 22 was constructed. Here the transition layer is modeled as a planar finite-element structure where each layer has a particular index of refraction determined by the doping level. The layers are identical thickness, and the overall number is subject to the user input. Although several techniques exist for calculating the reflectance characteristics of such stratified structure, the general methods developed by Abeles [48] are particularly attractive due to their suitability for computer implementation.

According to Abeles, each layer of the structure is defined by its characteristic matrix **M** which for *s*-polarized wave is given by

$$\mathbf{M}_s = \begin{bmatrix} \cos\delta & -\frac{i}{p}\sin\delta \\ -ip\sin\delta & \cos\delta \end{bmatrix} \tag{3.11}$$

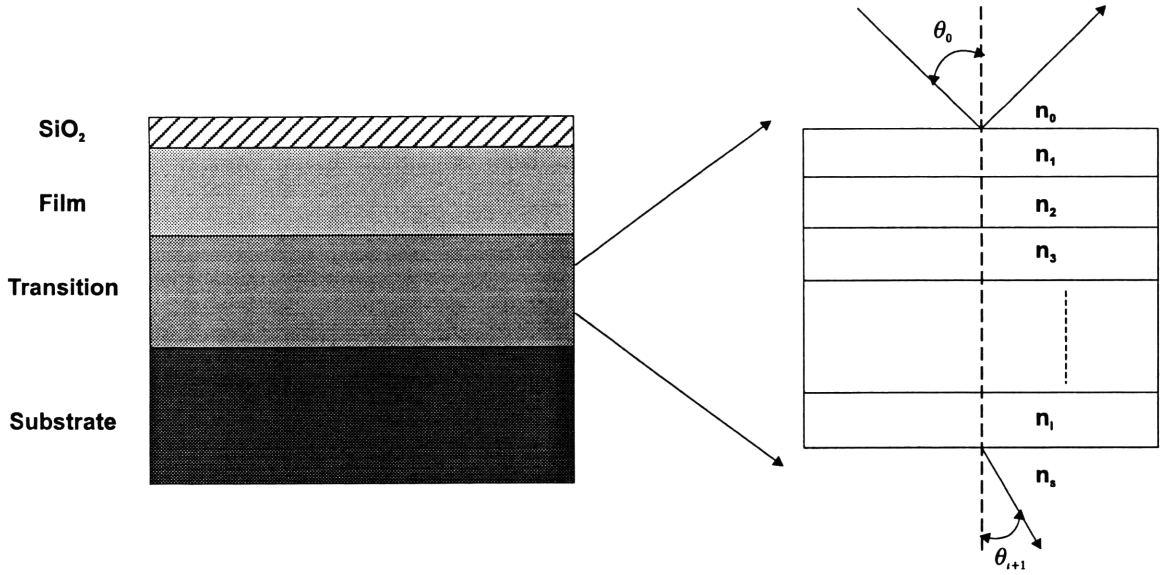

Figure 22 Finite element structure for model with doping profile

and for *p*-polarization is

$$\mathbf{M}_s = \begin{bmatrix} \cos\delta & -\frac{i}{q}\sin\delta \\ -iq\sin\delta & \cos\delta \end{bmatrix} \tag{3.12}$$

where

$$\begin{aligned} \delta &= 2\pi k(\mathbf{n}\cos\theta)z \\ p &= \mathbf{n}\cos\theta = \sqrt{\mathbf{n}^2 - (\mathbf{n}_0\sin\theta_0)^2} \\ q &= \frac{\cos\theta}{\mathbf{n}} \end{aligned} \tag{3.13}$$

Here k is the wavenumber in cm^{-1}, θ is (complex) angle of propagation in the slab, z is the thickness of the slab, and $\mathbf{n}$ is (complex) index of refraction of the slab. The overall characteristic matrix for the transition layer is given by the product of the individual matrices:

$$\mathbf{M}_{slp} = \prod_{i=1}^{n}\mathbf{M}_i = \begin{bmatrix} m_{11} & m_{12} \\ m_{21} & m_{22} \end{bmatrix}_{slp} \tag{3.14}$$

Then the reflection coefficients from the sample are given by for *s*- polarization as

$$r_s = \frac{(m_{11} + m_{12}p_s)p_0 - (m_{21} + m_{22}p_s)}{(m_{11} + m_{12}p_s)p_0 + (m_{21} + m_{22}p_s)} \tag{3.15}$$

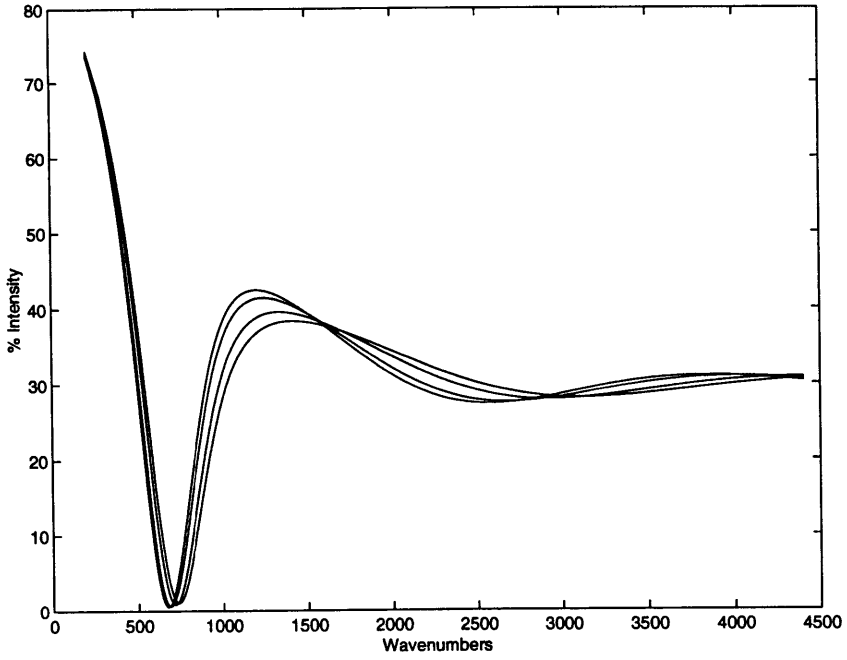

Figure 23: Calculated reflectance characteristics of several graded profiles

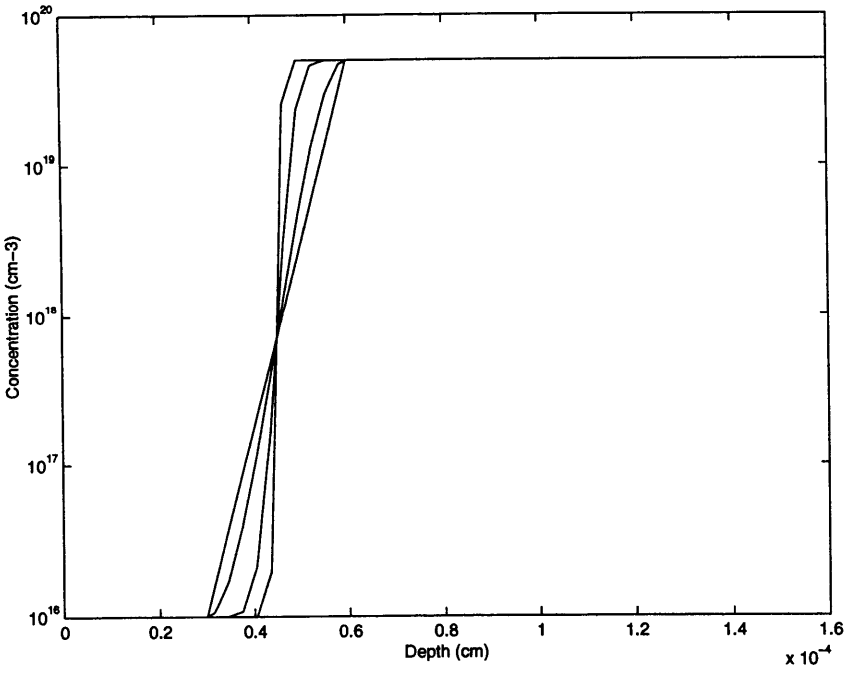

Figure 24: Graded profiles for figure 23

And for p-polarization

$$r_p = \frac{(m_{11} + m_{12}q_s)q_0 - (m_{21} + m_{22}q_s)}{(m_{11} + m_{12}q_s)q_0 + (m_{21} + m_{22}q_s)} \tag{3.16}$$

with p_0 and p_s for the incident medium (air) and substrate, respectively. The s- and p-polarized reflectances are given as before by Equations 3.6 and 3.7:

$$R_s = r_s r_s^*$$

$$R_p = r_p r_p^*$$

$$R_{tot} = R_s \xi(\alpha, \beta) + R_p \varsigma(\alpha, \beta)$$

Figure 23 and Figure 24 show calculated reflectance characteristics of several epi-substrate systems employing different transition profiles.

3.5 Dielectric Properties of Heavily Doped Silicon

Optical properties of intrinsic silicon have been extensively investigated due to the material's obvious importance in the electronics industry and the information which optical measurements provide on the material's bandstructure. Because of the value of the energy bandgap of silicon (E_g = 1.12 eV) and the nature of the optical measurement techniques, majority of the studies have been performed in the visible spectral range. In the IR studies have also been performed, since silicon may be used as optical material for wavelength beyond about 1.1 um. However, since main interest in silicon as infrared optical material was primarily related to its use as an infrared window material, investigations mainly focused on intrinsic silicon. The contribution of dopants to the optical properties of silicon were first considered by Spitzer and Fan [49], using reflectivity and absorption measurements in the region 5 to 35 um. They also obtained solution for the free carrier contribution to the dielectric function, which can be shown to simplify to [50]

$$\varepsilon' = n^2 - k^2 = \frac{\varepsilon_L}{\varepsilon_0} - \frac{\sigma_0 e}{\mu_0 \varepsilon_0 m^*}\left\langle \frac{\tau^2}{1+\omega^2\tau^2} \right\rangle \tag{3.17}$$

$$\varepsilon'' = 2nk = \frac{\sigma_0 e}{\omega \mu_0 \varepsilon_0 m^*}\left\langle \frac{\tau}{1+\omega^2\tau^2} \right\rangle \tag{3.18}$$

where $\sigma_0 = \frac{Ne^2\tau}{m}$ is the DC conductivity, τ is the free carrier relaxation time due to ionized impurity and acoustic phonon scattering, m^* is the electron/hole effective mass in silicon, N is the free carrier concentration, and ε_L is the dielectric constant of intrinsic silicon. The terms in brackets designate an averaging over the electron energy distribution[14]. Subsequent works produced some simplifications and refinements to these results. Schumann [19] used classical Boltzmann statistics and ionized impurity scattering with $E^{3/2}$ energy dependence to obtain an

[14] Relaxation time is usually an energy-dependant quantity

analytical expression in terms of Bessel functions. This was shown to be more accurate at shorter wavelength (5 um) and lower doping levels (mid-10^{18} cm^{-3}). Borghesi and Stella have investigated the effects of Si conduction band non-parabolicity and bandgap narrowing at the high-doping levels on the electron effective mass and concluded that electron effective mass exhibited systematic increase for doping levels above 10^{20} cm^{-3}[51]. Barta [52] performed Kramers-Kronig analysis of IR spectra of heavily doped *n*- and *p*- type silicon crystals and found the electron effective mass to be in agreement with accepted value (0.26), while the hole effective mass was systematically smaller. She found that this decrease could be accounted for by including the contribution of the interband transitions[15]. Hava and Auslander [53] used quantum statistical procedure to calculate the relaxation time $\tau(E)$ and compared the results to those of Eqn 3.17 and 3.18. They found that the quantum statistical predictions generally resembled the conventional model, but showed deviations at higher doping levels ($> 10^{19}$) and shorter wavelength (< 25 um).

In this work, we calculate infrared optical constants of doped silicon via relatively simple parameterized Drude model, and overcome the involved calculations as mentioned above by using the relaxation time as a free parameter, to be determined during the data analysis stage. This model, as will become evident in Chapter 4, will prove to be remarkably successful and particularly suitable to numerical implementation. In addition, this will also allow to determine electron/hole mobility and resistivity.

We begin by going back to the Maxwell equations (Eqn. 3.1). Specifically, replacing the term **J** in the second equation by

$$\mathbf{J} = \sigma\mathbf{E} \tag{3.19}$$

we obtain for the second equation:

---

[15] We will discuss this in chapter 4

$$\begin{aligned}\nabla\times\mathbf{H} &= j\omega\varepsilon\mathbf{E}+\sigma\mathbf{E}\\ &= j\omega\varepsilon(1-j\sigma/\omega\varepsilon)\mathbf{E}\end{aligned} \tag{3.20}$$

and we can define complex dielectric constant ε as

$$\varepsilon=\varepsilon(1-j\sigma/\omega\varepsilon) \tag{3.21}$$

and the previous solutions to the Maxwell equations including our expressions for the reflection coefficients and reflectance hold true with the new ε.

The AC conductivity $\sigma(j\omega) = Ne\mathbf{v}/\mathbf{E}$ is determined from the equation of motion

$$m\frac{d\mathbf{v}}{dt}+\frac{m\mathbf{v}}{\tau}=e\mathbf{E}e^{j\omega t} \tag{3.22}$$

Defining the DC conductivity as

$$\sigma_0=\frac{ne^2\tau}{m} \tag{3.23}$$

we obtain the AC conductivity as

$$\sigma=\frac{\sigma_0}{1+j\omega\tau} \tag{3.24}$$

Substituting (3.24) into (3.21) we obtain the dielectric function as

$$\frac{\varepsilon}{\varepsilon_0}=\varepsilon'-j\varepsilon''=\{\varepsilon(\omega)-\frac{\tau}{1+\omega^2\tau^2}\frac{\sigma_0}{\varepsilon_0}\}-j\{\frac{\sigma_0}{\varepsilon_0\omega}\frac{1}{1+\omega^2\tau^2}\} \tag{3.25}$$

Using the above expression and remembering that

$$\mathbf{n}=n-jk=\sqrt{\varepsilon} \tag{3.26}$$

we obtain the refractive index

$$n^2=\frac{1}{2}(\sqrt{\varepsilon'^2+\varepsilon''^2}+\varepsilon') \quad \text{and} \quad k^2=\frac{1}{2}(\sqrt{\varepsilon'^2+\varepsilon''^2}-\varepsilon') \tag{3.27}$$

Figures 2 – 3 earlier showed simulated optical constants of silicon for several doping levels.

3.6 Experimental Investigations of Si Refractive Index and Comparison with Model Predictions

Due to the extent of the spectral range in the far to mid-IR, the methods available for determining the refractive index of silicon are rather limited. These can be divided into "hard" and "soft" techniques.

The hard method utilizes dispersive spectrophotometry or FT-IR spectrometry at normal to near-normal angle of incidence[16] to measure both reflectance and transmittance spectra. For semi-infinite substrate, the equations 3.5a-g simplify to

$$R = \frac{(n-1)^2 + k^2}{(n+1)^2 + k^2} \tag{3.28}$$

The transmission T through a sample of finite thickness d is obtained as

$$T = \frac{(1-R)^2 e^{-\alpha d}}{1 - R^2 e^{-\alpha d}} \tag{3.29}$$

where α is the absorption coefficient defined as

$$\alpha = \frac{4\pi k}{\lambda} \tag{3.30}$$

and the reflectance spectrum r of the sample of finite thickness is obtained as

$$r = R(1 + Te^{-\alpha d}) \tag{3.31}$$

The reflection-transmission measurements (R-T) are problematic, since they depend on the sample thickness d to be known precisely in advance. The sample also must be rather thin (typically a few μm) in order to get reasonable transmission. The requirement for normal angle of incidence limits experimental flexibility and sensitivity as well, as shown later. In practice these measurements are sensitive to experimental variations and must be taken with a degree of caution.

---

[16] Normal angle of incidence is required to avoid polarization effects as discussed in Chapter 2.

The soft measurements mainly consist of Kramers-Kronig analysis (KKA). KKA is based on causality of the dielectric function and Hilbert Transform relations, which allow the imaginary part of a function to be determined from its real part, and vice versa [26]. For causal complex $H(t)$[17]

$$H(t) = H^{(r)}(t) + iH^{(i)}(t)$$

$$H^{(r)}(t) = -\frac{1}{\pi} P \int_{-\infty}^{\infty} \frac{H^{(i)}(t')}{t'-t} dt' \tag{3.32}$$

and

$$H^{(i)}(t) = \frac{1}{\pi} P \int_{-\infty}^{\infty} \frac{H^{(r)}(t')}{t'-t} dt' \tag{3.33}$$

where P is the Cauchy principal value.

In practice the equations 3.32-33 can be replace by the symmetry/anti-symmetry arguments which allow the KKA analysis to be efficiently implemented via DSP techniques [54][18].

Thus Eqns 3.32-33 allow one to determine the amplitude from the phase and vise versa. As the amplitude information is contained in the reflectance spectrum, both real and imaginary components of the refractive index become readily available.

KKA analysis, while conceptually elegant and highly suitable to numerical implementation, depends on the reflectance (or transmittance) spectrum being known over the infinite frequency range. Since only a small portion of the spectral range is obtained during the measurement, assumptions are made to fill in the blanks. Thus KKA methods do not enjoy particular popularity for high-precision studies. In addition, the measurements must be performed at normal angle of incidence for the same reasons as previously stated. In a number of instances, it is very advantageous to perform optical studies at highly oblique angles of incidence to obtain high-

[17] *H(t)* is often called *analytic signal* in communication and signal processing

[18] Surprisingly, many physicists and material scientists are not aware of this, and perform KKA using the tedious integrals.

sensitivity results. For example, extremely sensitive studies can be done at Brewster angle of a given material, where the reflectivity of *p*-polarized radiation is reduced to zero. Brewster angle of undoped silicon is 73.7 degrees, and of glass is 56.40 degrees.

Yet another soft method sometimes reported in the literature is to fit a particular model (for example, generalized Drude to the obtained reflectance spectrum. This method is even less popular than the above techniques, due to the physicist's inherent dislike for fitted parameters.

In this work, we use infrared ellipsometry (IRSE) to determine the optical constants of several highly doped silicon samples. Ellipsometry in the near-IR, visible and UV (SE) has been most popular technique for determination of refractive index. Since SE measures amplitude and phase components, both n and k refractive index components are directly provided. Since normal incidence is no longer required, very sensitive measurements, including Brewster angle, are possible.

As mentioned earlier, IRSE has recently emerged via coupling of FT-IR and polarizing components, and due to the development of methods which allow the measurements to be made with imperfect components. IRSE will be discussed in more detail in Chapter 5. Here we utilize one of a few commercially available IRSE instruments at near- Brewster angle of doped silicon to take advantage of the high sensitivity accorded by this arrangement[19]. As mentioned earlier (Equation 1), IRSE produces measurements in terms of $tan\psi$ - the amplitude ratio, and Δ - the phase difference. From these, the real and imaginary components of the dielectric function are obtained as [55]

$$\varepsilon' = n^2 - k^2 = (n_0 \sin\varphi_0)^2 \left(1 + \frac{\tan^2\varphi_0(\cos^2 2\psi - \sin^2 2\psi \sin\Delta)}{(1+\sin 2\psi\cos\Delta)^2}\right) \qquad (3.34)$$

$$\varepsilon'' = 2nk = \frac{-(n_0 \sin\varphi_0 \tan\varphi_0)^2 \sin 4\psi \sin\Delta}{(1+\sin 2\psi\cos\Delta)^2} \qquad (3.35)$$

[19] Brewster angle of doped silicon declines from its intrinsic value due to the decrease in n

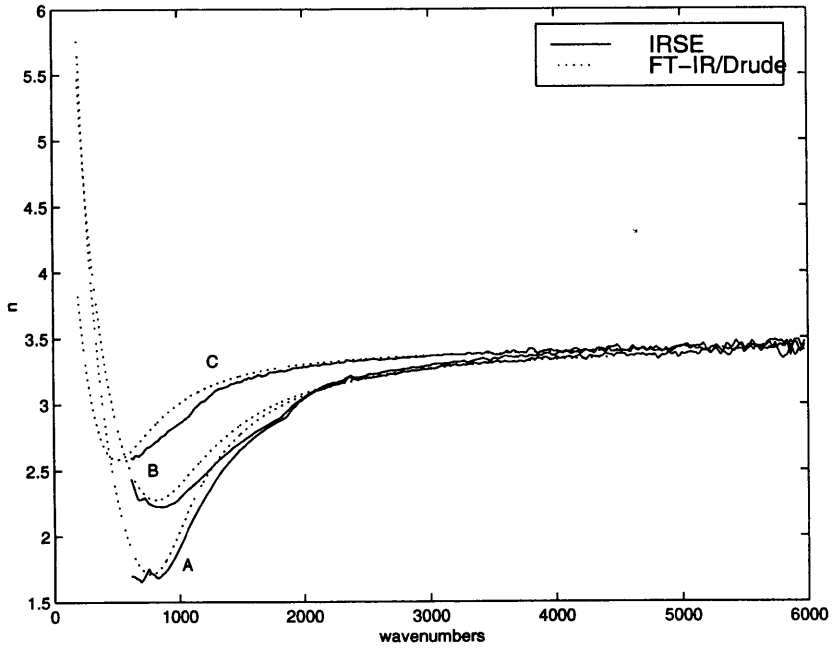

Figure 25: Real part of refractive index *n*. Obtained by infrared ellipsometry vs. fitted by Drude model using FT-IR reflectance spectrum of doped substrates. Sample A boron doped, N=4.4E19. Sample B arsenic doped, N=3.0E19. Sample C boron doped, N=1.53E19

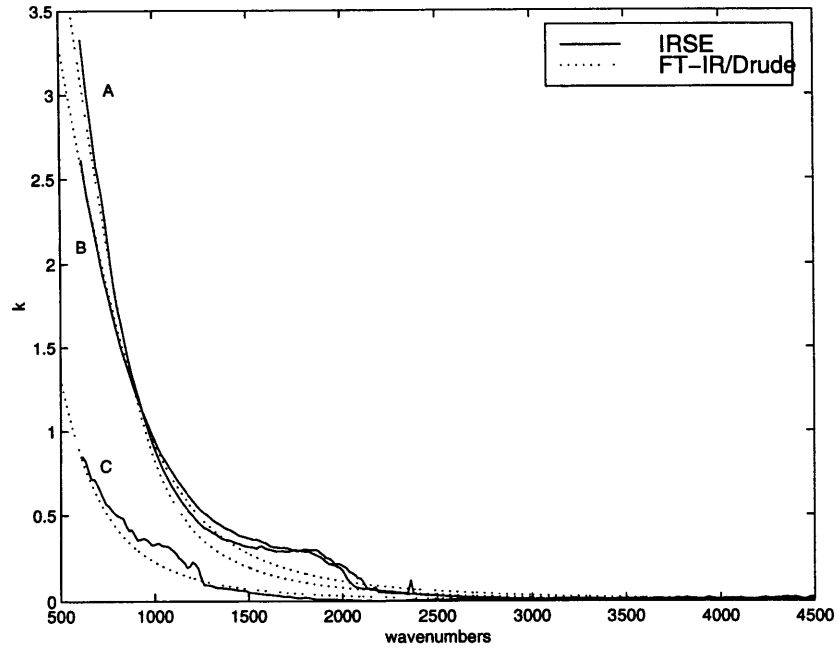

Figure 26: Extinction coefficient *k* for samples A,B, and C.

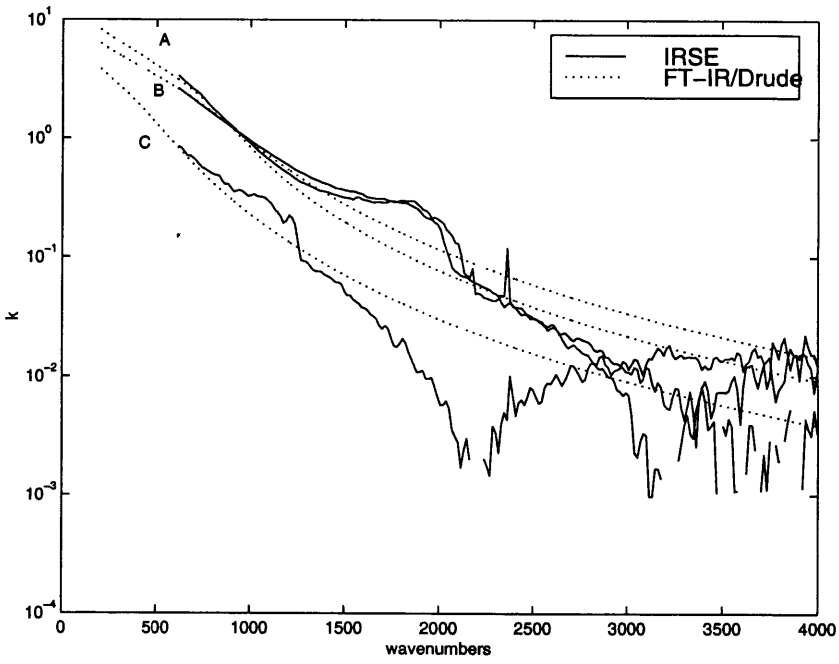

Figure 27 Imaginary part of refractive index *k* on a semilog scale

Figure 25, Figure 26 and Figure 27 show optical constants for 3 doped substrates as determined by IRSE For comparison, optical constants of the same samples were determined from the FT-IR reflectance spectra .

3.7 Effects of the native oxide.

A very thin layer of native oxide (up to a few nm) is usually present on the epi [3]. The optical properties of thin native oxide on silicon in the infrared have been investigated by Wong and Yen [56-57]. The question of whether this layer effects the measurements must be considered. From the previously derived expression for the film phase difference β, consider SiO_2 film thickness of 1 nm, and wavenumber *k* of 4500 (extreme case). A quick calculation produces β = 3.02E-2, which results in $e^{-j2\beta} = 1$. Substituting this into the expressions for the total reflection coefficients, it's a simple exercise to show that native oxide has negligible effect on either the

measurements or on simulations as long as the requirement $e^{-j2\beta} = 1$ is satisfied.

Physically, this means that as long as there is no interference between the wave reflected from the air-oxide interface and the oxide-epi interface (the two waves are in phase), light emerges from the oxide un-attenuated and undisturbed.

Chapter 4.

Measurements, Data Analysis and Results.

4.1 Introduction

This chapter presents the results obtained from the reflectance measurements. We first describe the sample set employed in the measurements, the data analysis methods employed to extract the items of interest from the measurement data, and characterization methods used to compare the measurement predictions to the characterization data. We then present the results of the measurements from a variety of samples, starting with blank substrates, and followed by thin films on $p+$ and $n+$ wafers employing abrupt junction and transition layer model. We consider the measurement results in the light of the characterization data, and discuss the limits on thickness and concentration these measurements are capable of achieving.

4.2 Wafer Matrix and Material Characterization

In order to validate the methods and models developed in this thesis, a comprehensive wafer matrix was constructed which included a variety of samples of varying film thickness, substrate dopant concentration and types, and different processing conditions. Overall about 100 samples obtained from different sources were employed, with films ranging from about 40 nm to several μm in thickness, and substrates of B, As, and Sb in the ranges of 10^{18} to 10^{20} cm^{-3}. Deposition temperatures employed were 700, 850 and 900 degrees C. The listing of the samples can be found in Appendix A.

When it comes to the methods for characterizing thin silicon epi-layers, the options are very limited. This is illustrated in Figure 28, showing a high-resolution XTEM cross-section of an epi-layer sample typical of the measurements. Even though the TEM employed is a state-of-the-art instrument, capable of 3 Å resolution, the difference between the epitaxial region and the substrate is not detectable. This, of course, is not surprising as even for the highly doped substrate of 10^{20} cm^{-3}, dopants constitute fewer than 1% of the atomic population.

The only tool capable of addressing thin epi requirements of measuring the dopant profiles in silicon is Secondary Ion Mass Spectrometry (SIMS). SIMS belongs to the class of measurements known as ion beam techniques, where a beam of ions is used to bombard the sample surface causing ion-solid interaction from which various material properties can be inferred. Other examples of ion-beam technique include Ion Scattering Spectrometry (ISS), and Ratherford Back-scattering (RBS). In SIMS, the beam energy is increased to reach the onset of sputtering, which causes a variety of species present in the material to be emitted. These include such dopants as boron, phosphorus, arsenic and antimony, and contaminants as oxygen, carbon, iron and copper. These can be identified according to their masses, and their concentration can be measured down to fairly low level: typically 10^{15} for most species. SIMS is capable of high depth resolution, as the depth profiling is correlated with sputtering rate and time, which are typically a few hundred

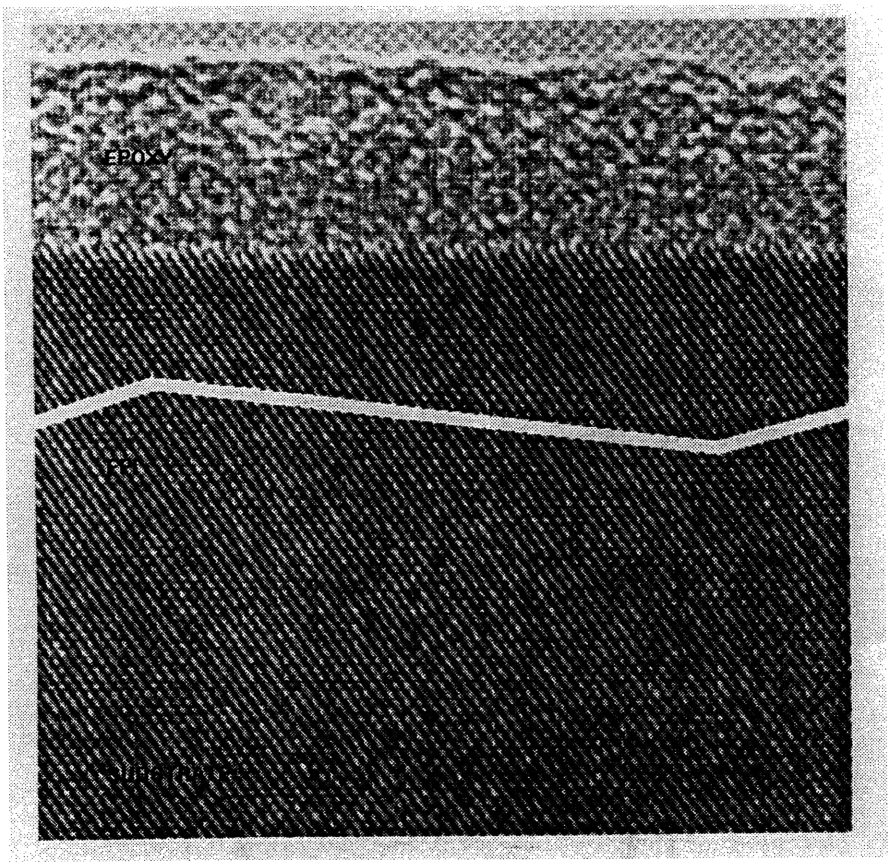

Figure 28 XTEM of a typical sample in the wafer matrix.

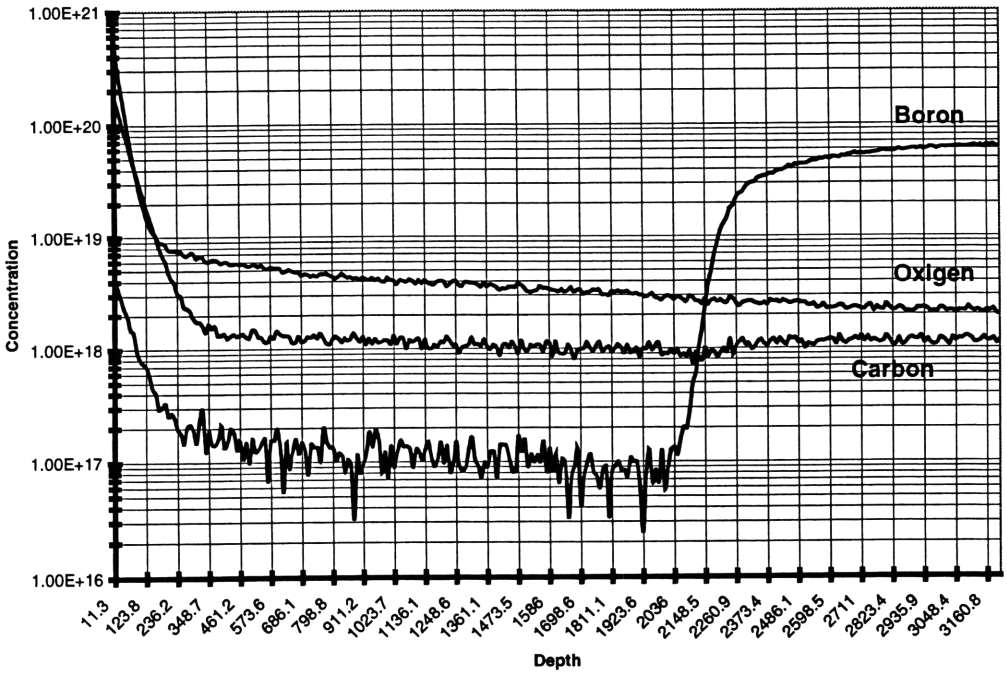

Figure 29 SIMS characterization for sample SEA4

Å/min. It is also sensitive to the chemical species making up the material composition, although it requires the use of standards for each material. On the other hand, SIMS is known to be affected by artifacts and atomic mixing [58]. These can cause a loss of depth resolution and secondary ion collection efficiency. The precision of the technique is a problem as well – 15-20% variation in measurements is not uncommon. Another feature of SIMS is that unlike the electrical and optical techniques which measure free carrier concentrations due to activated dopants, SIMS detects ionized impurities. These factors must be born when making comparisons between the methods. SIMS technology has been substantially improved over the past 10 years, and today is being utilized to measure such challenging structures as ultra-shallow junctions formed in the near-surface of silicon (2-100 nm). A good review of the state-of-the-art in SIMS measurements is available from Chason *et al.* [59]. In this thesis, extensive SIMS characterization was undertaken using the facilities of Evans East and Phillips Semiconductor. Figure 29 shows SIMS profile of a typical sample utilized in the study. As seen from the figure, the sample is of good quality, with relatively steep epi-substrate transition and carbon and oxygen concentration not exceeding specifications.

4.3 Data Analysis

Once the epi-layer/substrate structure has been constructed and the parameterized model of reflectance defined as $\mathbf{R}_{mod}(\mathbf{z})$, where the parameter vector $\mathbf{z}$ contains material properties of interest (film thickness, dopant concentration, relaxation time and profile shape) and the instrument parameters (α and β), the desired quantities are obtained by optimizing the values of $\mathbf{z}$ for the best fit against the experimentally obtained reflectance as shown in Figures 15 and 16. While the error criteria may assume a number of forms, the traditional mean-square error (MSE) was found to be adequate, where MSE is defined as

$$MSE = \sum_{k} [R_{exp} - R_{mod}(\mathbf{z})]^2 \qquad (4.1)$$

The task of finding the optimum parameter vector **z** belongs to the class of problems known as non-linear regression. Here a guess $\mathbf{z}^{(0)}$ is made at the parameter vector, and the Eqn. 4.1 is linearized around the guess as

$$\begin{bmatrix} \frac{\partial R_{\mathrm{mod}}(k_1)}{\partial z_1} & \cdots & \frac{\partial R_{\mathrm{mod}}(k_1)}{\partial z_M} \\ \vdots & \cdots & \vdots \\ \frac{\partial R_{\mathrm{mod}}(k_N)}{\partial z_1} & \cdots & \frac{\partial R_{\mathrm{mod}}(k_N)}{\partial z_M} \end{bmatrix} * \begin{bmatrix} z_1^{(0)} - z_1^{(1)} \\ z_2^{(0)} - z_2^{(1)} \\ \vdots \\ z_M^{(0)} - z_M^{(1)} \end{bmatrix} = \begin{bmatrix} R_{\mathrm{exp}}(k_1) - R_{\mathrm{mod}}(k_1) \\ \vdots \\ R_{\mathrm{exp}}(k_N) - R_{\mathrm{mod}}(k_N) \end{bmatrix} \quad (4.2)$$

The Equation 4.2 is an over-determined linear system $Ax = b$, whose solution vector x minimizes the error $\|Ax - b\|^2$ and is given by the solution of the normal equations $A^T Ax = A^T b$ [60]:

$$x = (A^T A)^{-1} A^T b \quad (4.3)$$

Solving the linear system (4.2) according to (4.3) provides the guess at the corrected parameter vector $\mathbf{z}^{(1)}$, and the procedure may be repeated until the MSE error (4.1) is minimized. Several variations on the basic procedure exist which address specific preferences on the speed of convergence and stability. In this thesis we follow the Levenberg-Marquardt procedure [61].

4.4 Study of Heavily Doped Substrates

As was shown earlier, reflectance measurements exhibit sensitivity to the level of doping in the substrate. Thus dopant concentration may be obtained non-contact for heavily doped (>10^{18} cm^{-3}) substrates. Mobility and resistivity are obtained as well via the relaxation time τ:

$$\mu = \frac{\tau e}{m^*} \quad (4.4)$$

Figure 30- Figure 33 show the results of reflectance studies of heavily doped *n*+ and *p*+ substrates.

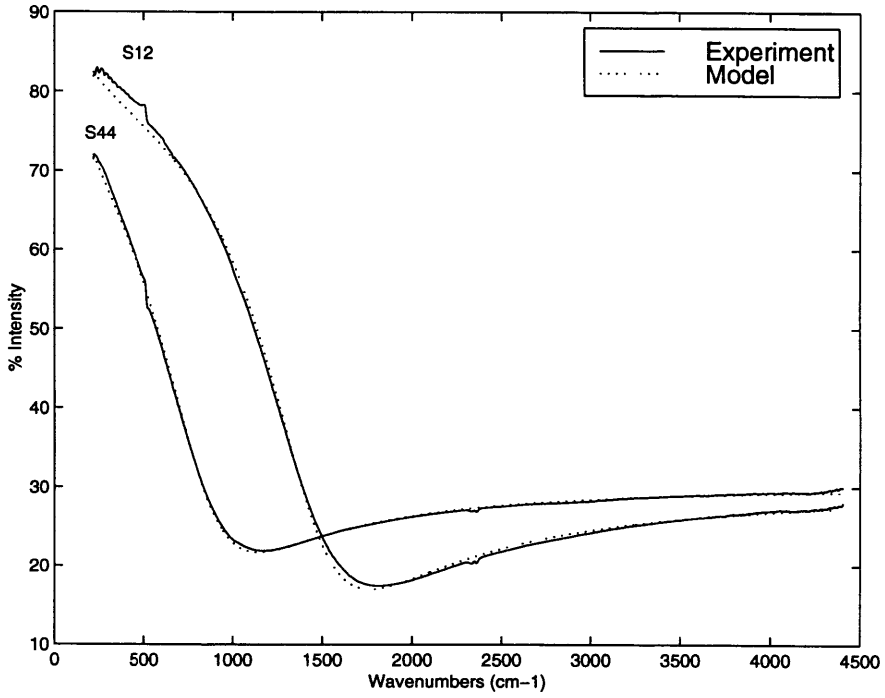

Figure 30: Reflectance spectra of highly doped P^+ substrates

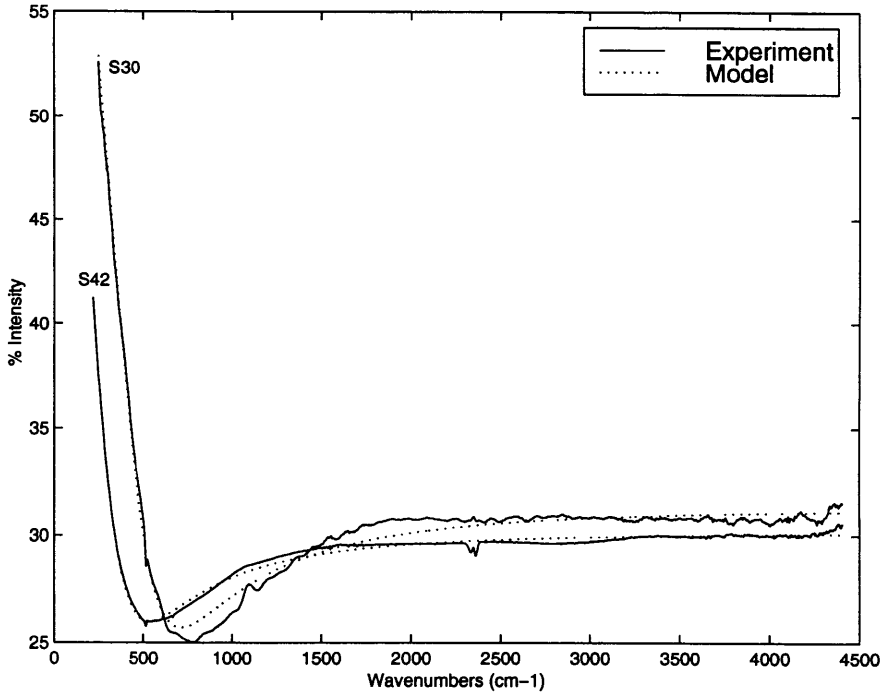

Figure 31: Reflectance spectra of P^+ substrate with intermediate doping level

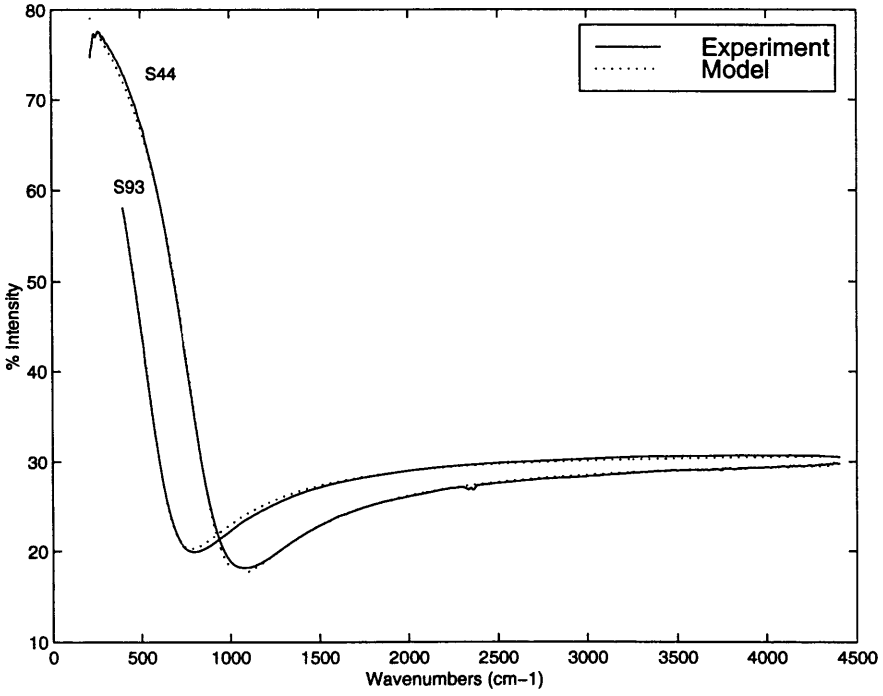

Figure 32: Reflectance spectra of As doped substrate

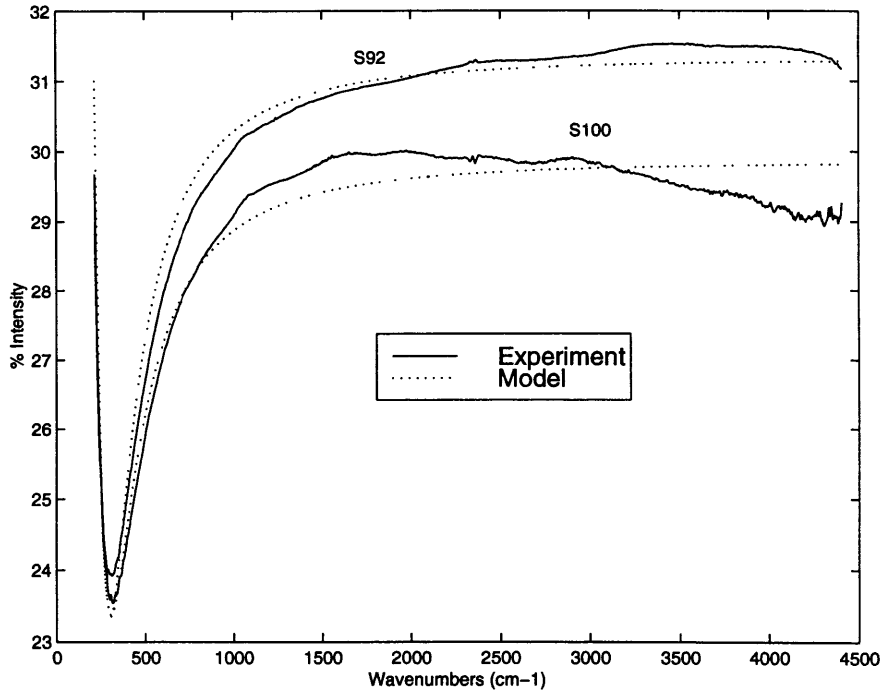

Figure 33: Reflectance spectra of Sb doped substrate

Here the dielectric constant of doped silicon was obtained according to Equations 3.27. The electron effective mass of silicon was assumed 0.26, and hole 0.37, according to [62]. The optimization vector **z** included substrate dopant concentration N_{sub}, relaxation time τ, and the FT-IR polarization parameters α and β. The results of the study were compared with measurements performed via 4-Point probe, and are summarized in Table 2.

Sample	Concentration N (10^{18} cm^{-3})	Concentration 4-Pt Probe	Relaxation τ (10^{-15} sec)	Mobility μ (cm^2/Vsec)	Resistivity (mΩ-cm)
BLK1 (Sb) (S100)	1.99	1.87	25.1	169	18.5
S92 (Sb)	2.06	1.99	29.5	200	15
S44 (As)	30.5	29.9	12.9	87	2.3
S93 (As)	15.5	14.7	14.7	99.4	4.1
S42 (B)	7.33	4.88	10.8	51.3	16.6
SEB1 (B)	15.2	10.1	7.8	49.9	8.2
S12 (B)	120	79	7.8	37	1.4
S43 (B)	43.8	34	8.2	39	3.7

Table 2: Measurements of doped substrates

It is seen that very good agreement between the model and experiment is achieved for N^+ substrates and heavily doped P^+ samples. Even for Sb samples with relatively low doping, measurements do not present particular difficulties, and the accuracy is good. Measurements on N^+ samples correlate well with results obtained via 4-Pt probe measurements. On the other hand, the doping level is overestimated in the case of P^+ substrates. This suggests that some additional absorption mechanism may take place, as perhaps the interband transitions into the split-off band, as suggested by Barta [53].

4.5 Studies of Thin Epitaxial Layers: Results Using Abrupt Layer Model

When the combined thickness of the epitaxial film and its transition layer is less than approximately 1 um, it was found that such thin-film samples are well described by the abrupt profile model of Figure 18. A variety of sub-um epi-layer samples were investigated. These were grown on Boron, Arsenic, and Antimony substrates.

Case 1: Silicon Epi-layers on P^+ Doped Substrates

Figure 34 - Figure 44 display the reflectance spectra from the FT-IR measurements, and obtained via the optimization for a set of 9 thin epitaxial wafers grown on Boron substrates. The samples shown are representative of the wafer matrix, and are chosen based on the quality of the characterization data rather than the closest model fit. The corresponding SIMS profiles are displayed as well. The results of the study are summarized in Table 3.

Sample	Concentration N (10^{18} cm^{-3})	d_{epi} (nm)	Relaxation τ (10^{-15} sec)	Mobility μ (cm^2/Vsec)	Resistivity (mΩ-cm)
S74	42.4	198	7.58	36	4
S52	104	245	8.12	38.5	1.6
S75	103	104	7.89	37.5	1.6
S66	113	288	8.03	38.2	1.45
S76	94	289	7.73	36.7	1.81
S61	93	62	8.56	40.7	1.83
S73	48	73	7.7	36.7	3.96
Sec2	18	143	8.24	39.2	10.0
Sea4	19	281	7.3	34.7	10.2

Table 3: Epitaxial Films on Boron Substrates

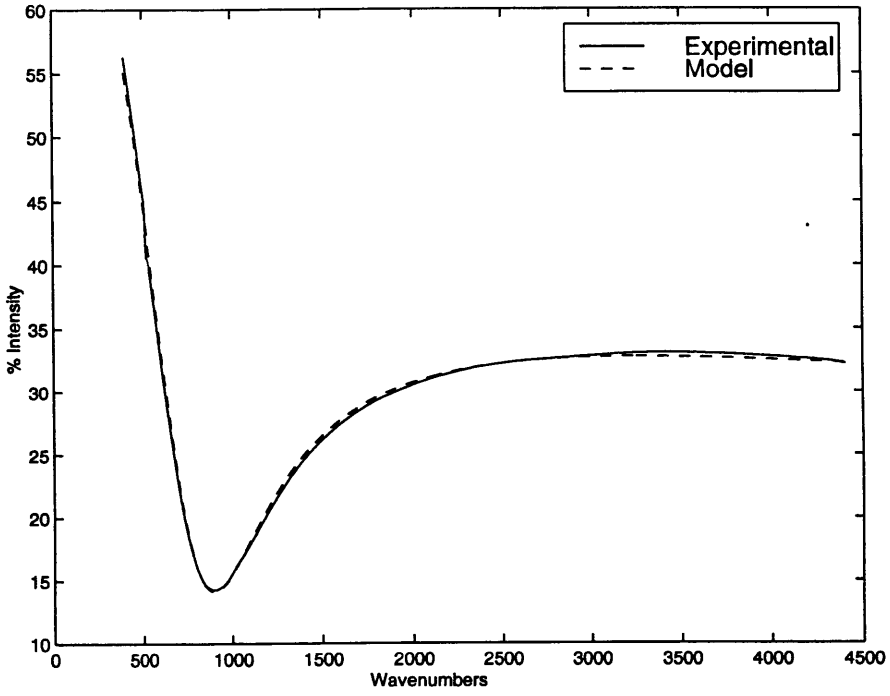

Figure 34 Sample S74: Opimized vs. experimental results

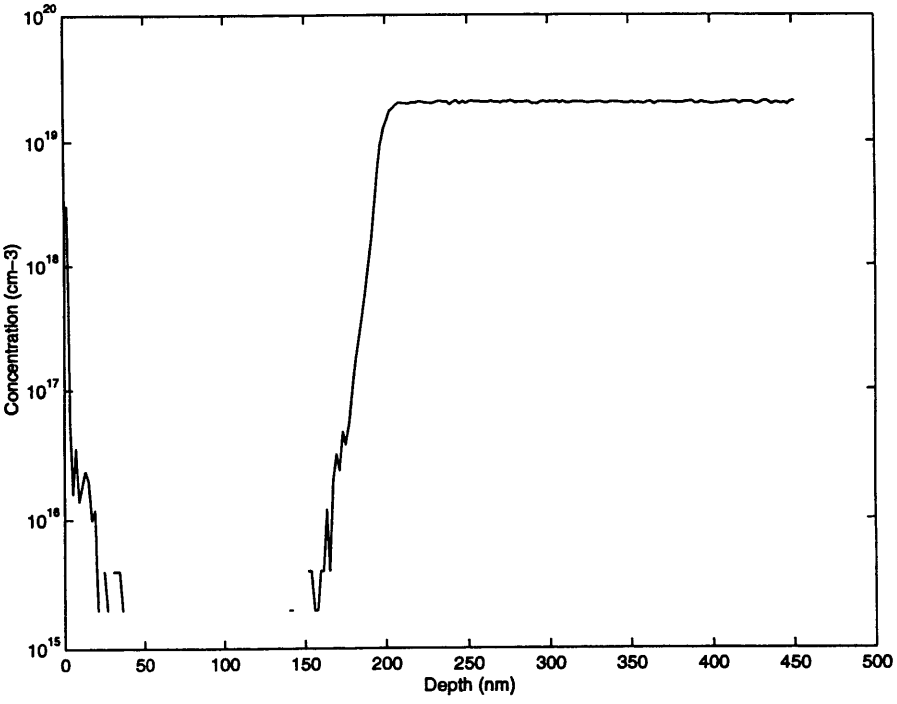

Figure 35 Sample S74: SIMS characterization

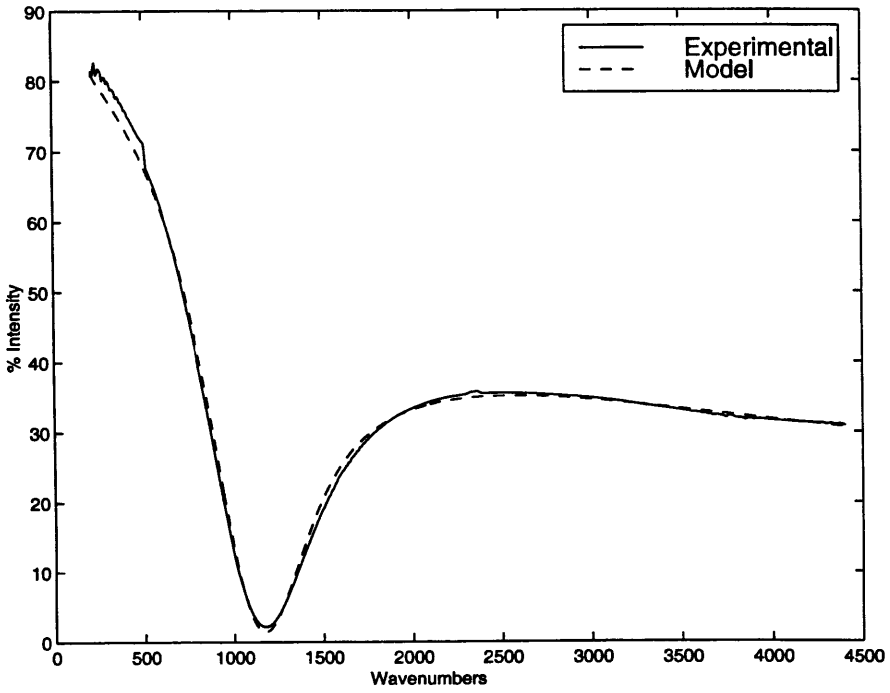

Figure 36 Sample S52: Opimized vs. experimental results

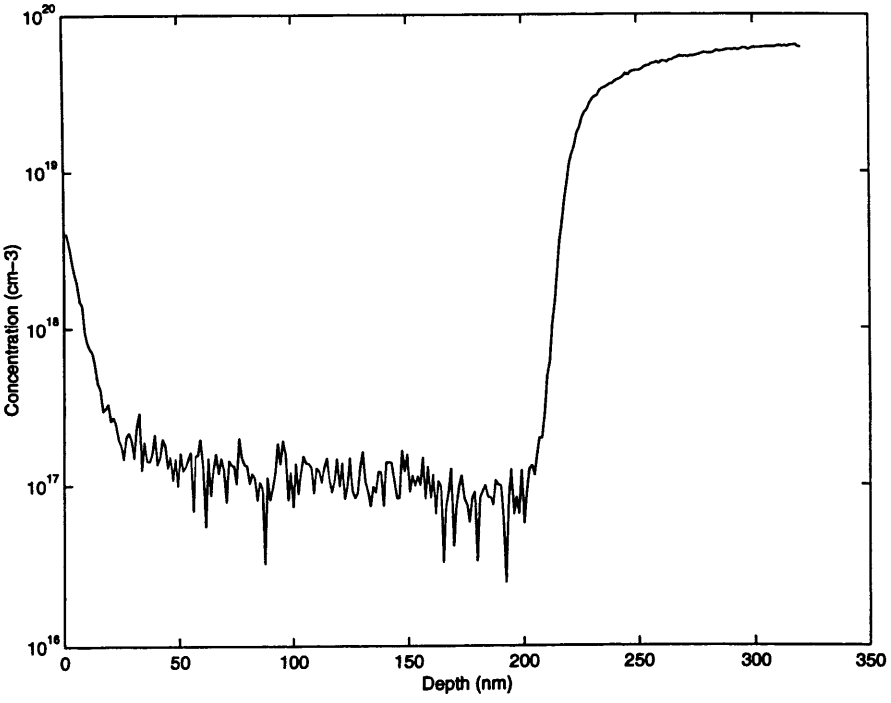

Figure 36: SIMS Sample S52

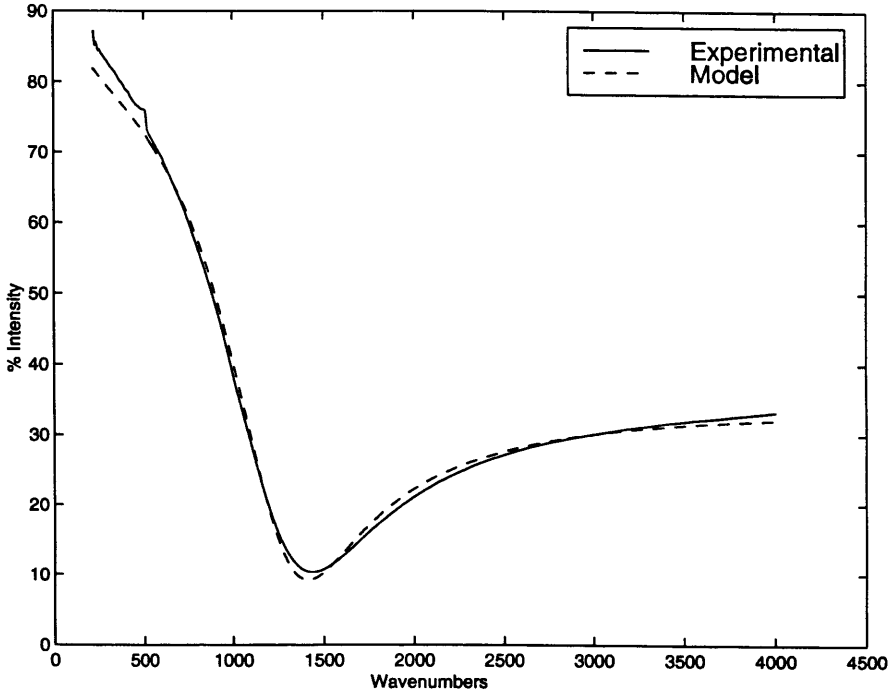

Figure 37: Sample S75: Opimized vs. experimental results

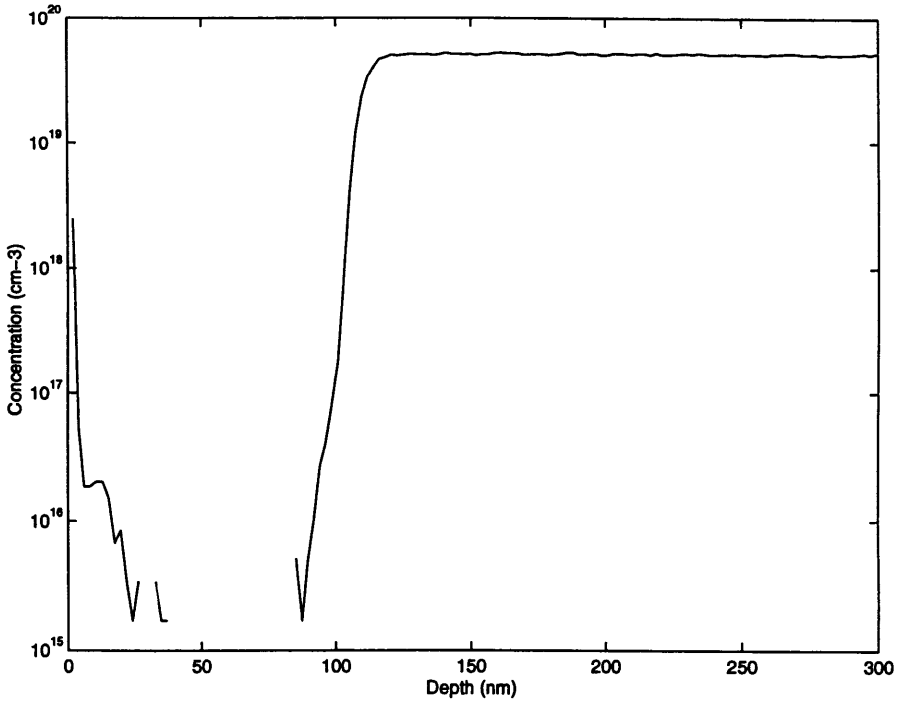

Figure 38: SIMS Sample S75

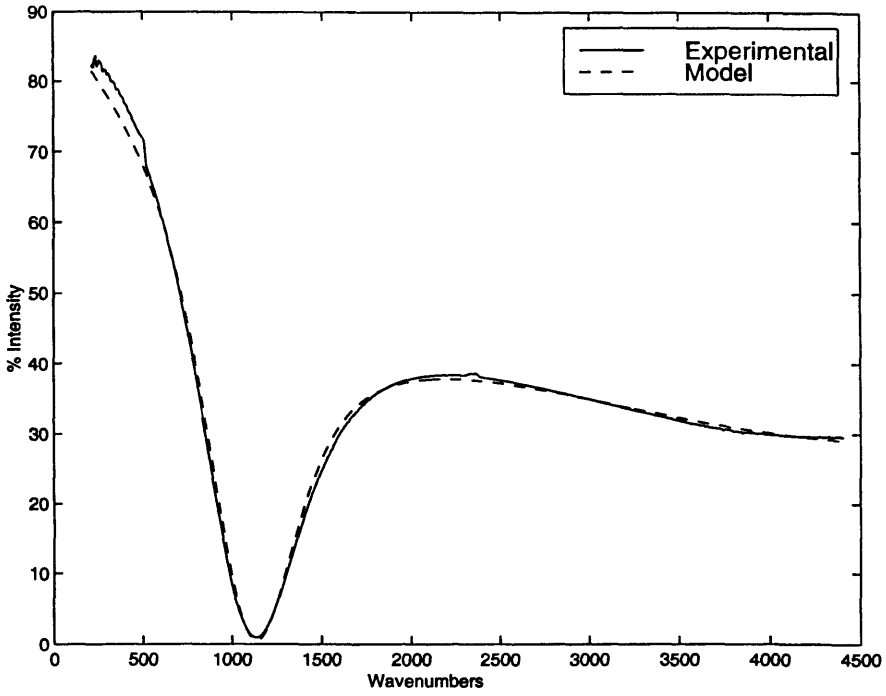

Figure 39: Sample S66: Opimized vs. experimental results

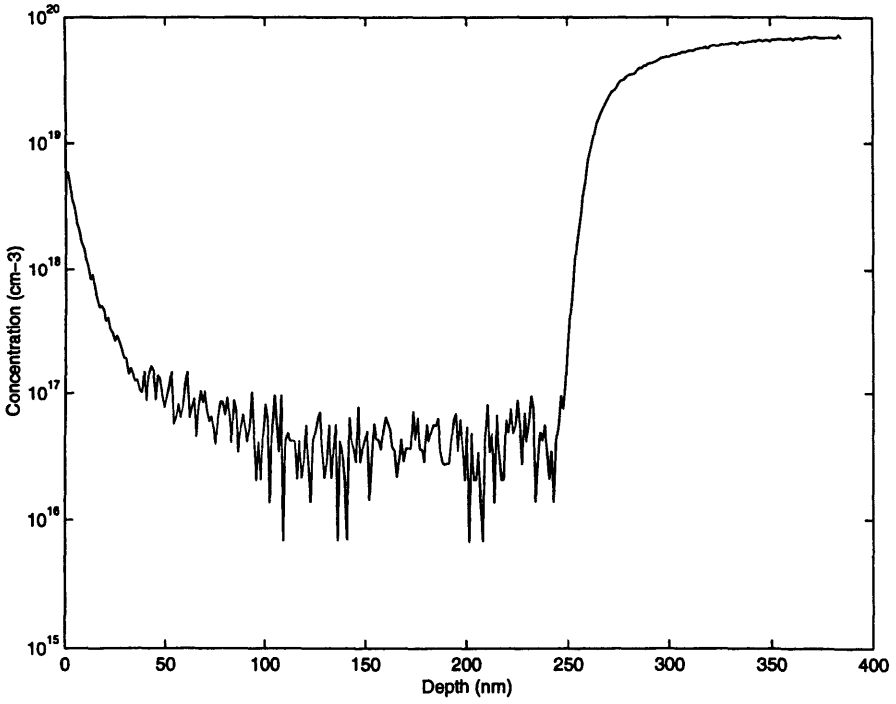

Figure 40: SIMS Sample S66

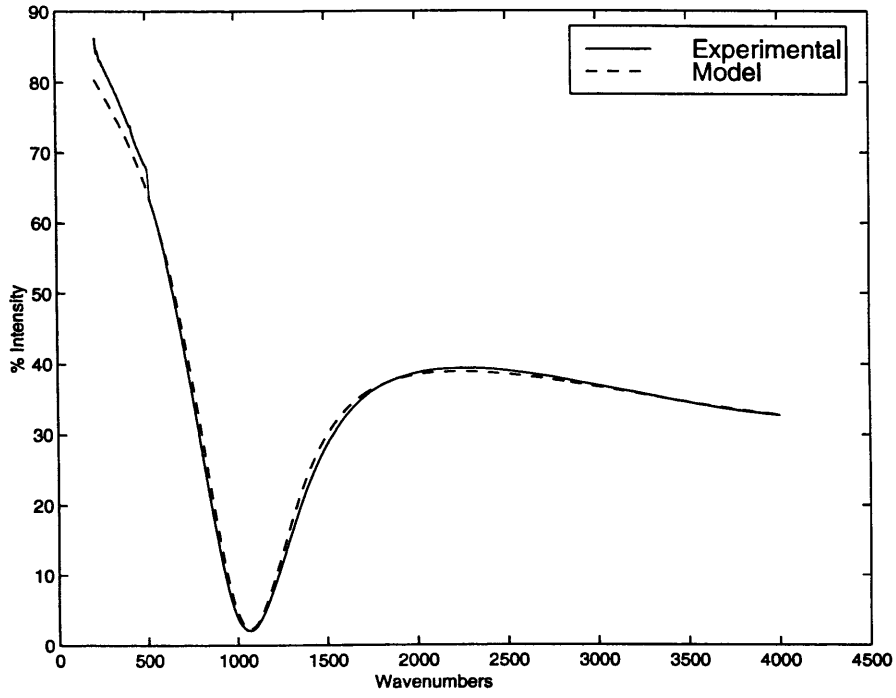

Figure 41: Sample S76: Opimized vs. experimental results

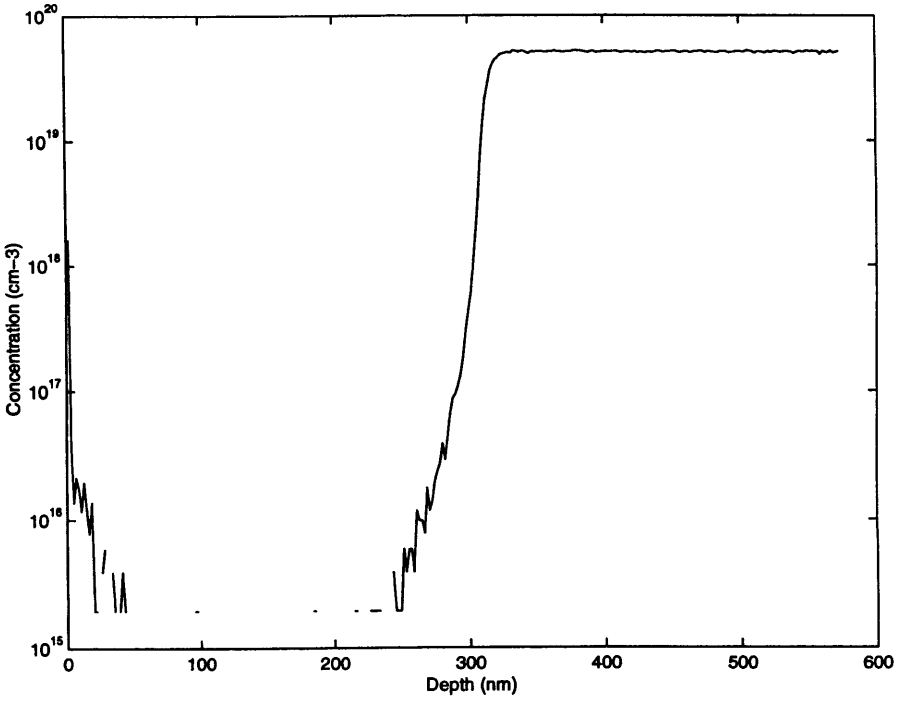

Figure 42: SIMS Sample S76

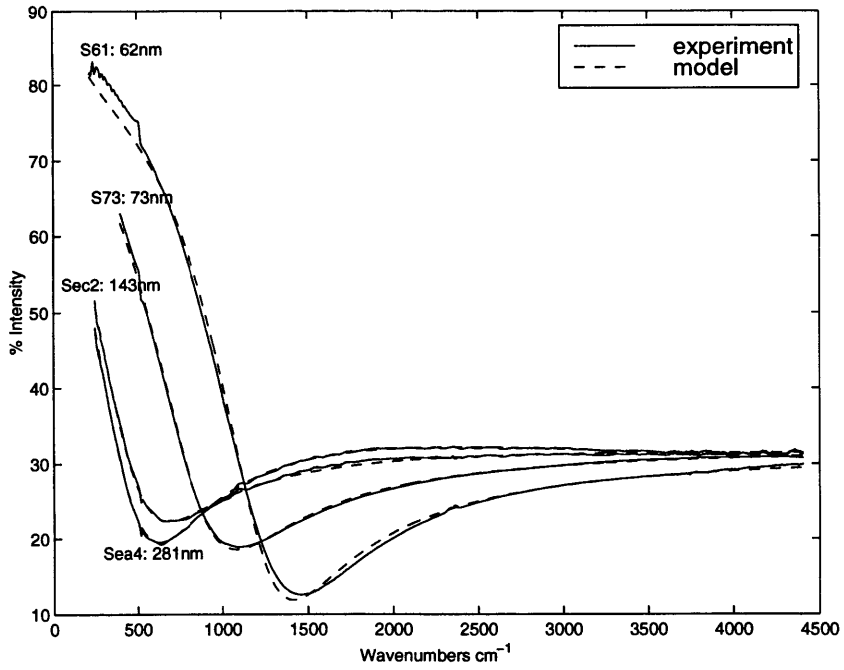

Figure 43: Reflectance spectra of thin epi-layers on Boron doped substrates: Opimized vs. experimental results

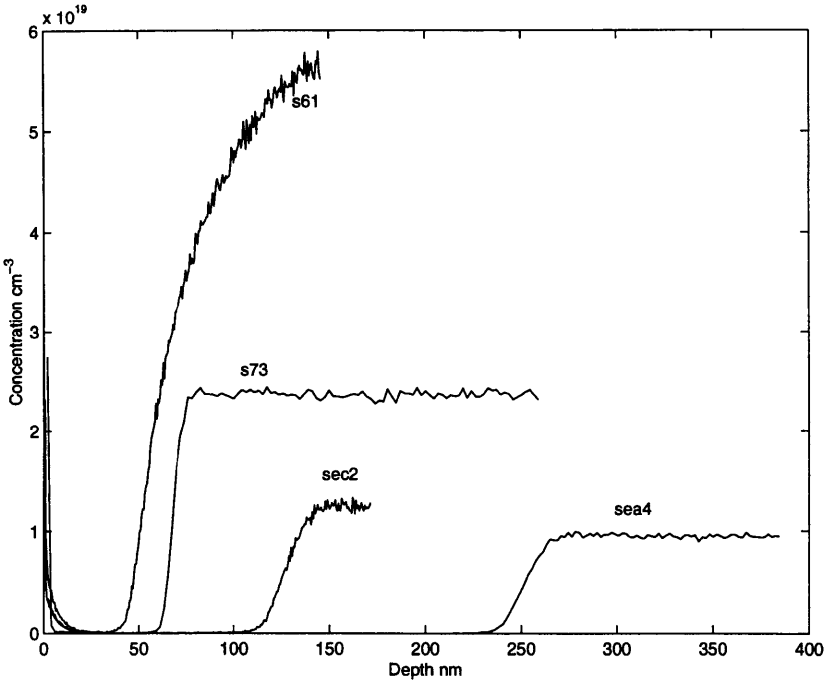

Figure 44: SIMS characteristics

As seen from the results, a good agreement is obtained between the model and the experimental measurements for thin epi-layers on P+ substrates, and film thickness as obtained with this method correlates well with SIMS data. Accurate film thickness determination is achieved on films as thin as 60+ and 70+ nanometers quite easily, which is at least one order of magnitude better than what is possible with conventional FT-IR methods. On the other hand, the doping level in the substrate is over-estimated, which is consistent with the results obtained from the study of heavily doped substrates. This discrepancy could be resolved by utilizing more involved model of P^+ type silicon, as discussed in Section 4.4, or, perhaps less sophisticated but more practical, having a table of conversion between the optical and electrical measurements.

A natural concern in doing optimization process as performed here is whether the final optimization vector $\mathbf{z}_0$ is unique. As the calculated reflectance R_{mod} is a highly non-linear function of its parameter variables, it is generally not possible to prove this rigorously. However, a good indication is obtained from a 2-D grid simulation as displayed in Figure 45. Here various combinations of film thickness and dopant concentration are plotted against the *MSE* for one of the samples in the study. As can be seen, a pronounced *MSE* minimum exists for a unique combination of N_{sub} and d_{epi}. Since, by necessity, the rest of the parameters in the $\mathbf{z}$ vector were held constant, this minimum is not as pronounced as in the full optimization process. Nevertheless, the thickness and concentration as obtained from the grid simulation correlate quite well with the results of Table 3.

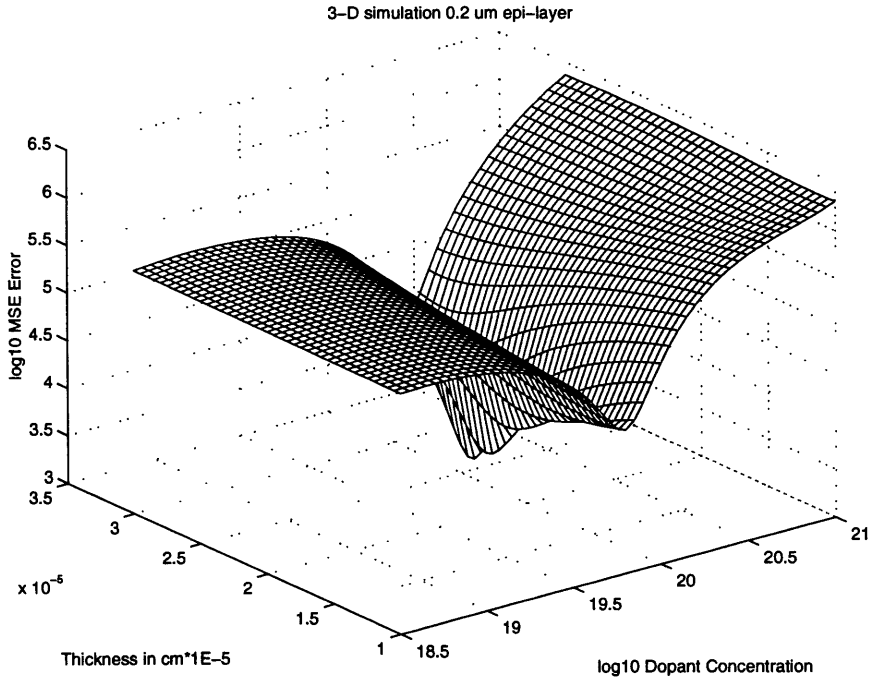

Figure 45: 2-D grid simulation for sample S52, showing strong minimum in mean square error

Case 2: Silicon Epi-layers on N^+ Doped Substrates

For the study of thin silicon epi-layers, arsenic and antimony-doped wafers were utilized. The measured and optimized waveforms along with SIMS data are shown in Figure 46 - Figure 49. The results of the optimization are displayed in Table 4.

Sample	Concentration N (10^{18} cm^{-3})	d_{epi} (nm)	Relaxation τ (10^{-15} sec)	Mobility μ (cm^2/Vsec)	Resistivity (mΩ-cm)
S78 (As)	34	47	13	88	2.6
S89 (As)	15	123	13	87.9	4.4
S90 (As)	15	358	13	88	4.6
S87 (Sb)	1.8	126	22	149	16.2
S88 (Sb)	1.4	330	27	183	15.6

Table 4: Epitaxial Films on As and Sb Substrates

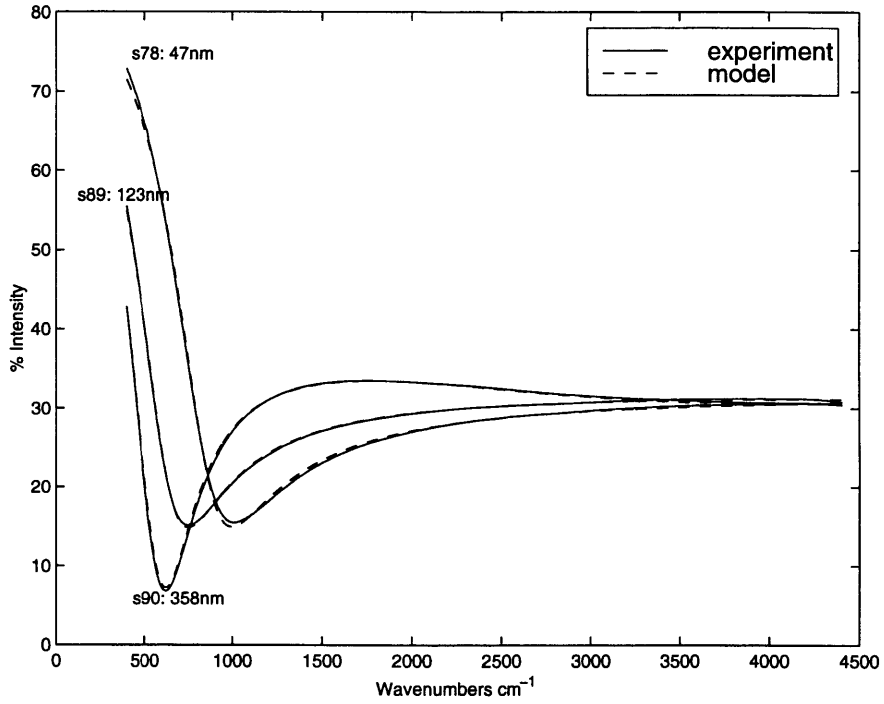

Figure 46: Reflectance spectra of thin epi-layers on As doped substrates: Opimized vs. experimental results

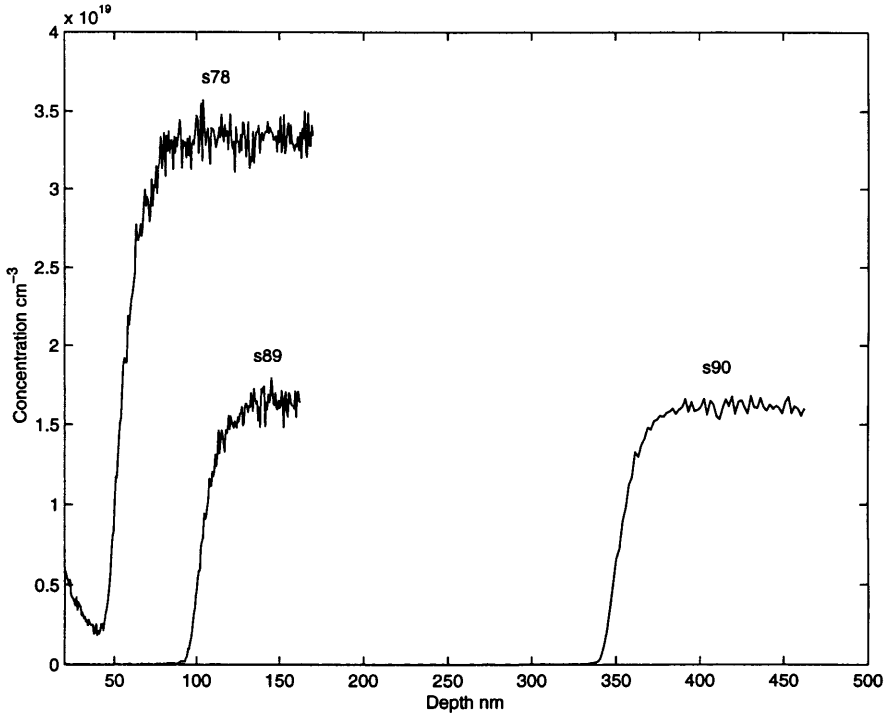

Figure 47: SIMS characteristics

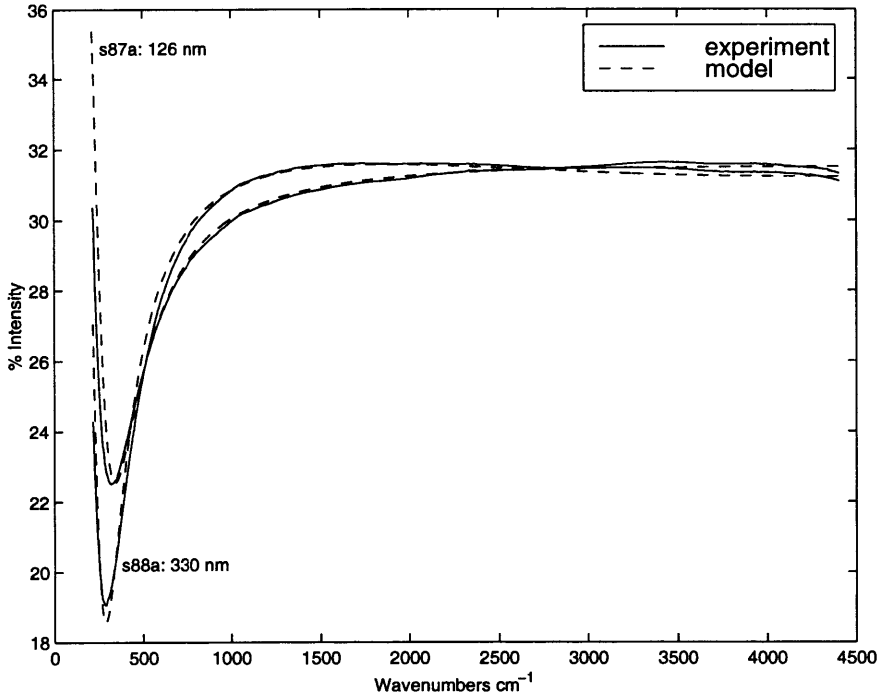

Figure 48: Reflectance spectra of thin epi-layers on Sb doped substrates: Opimized vs. experimental results

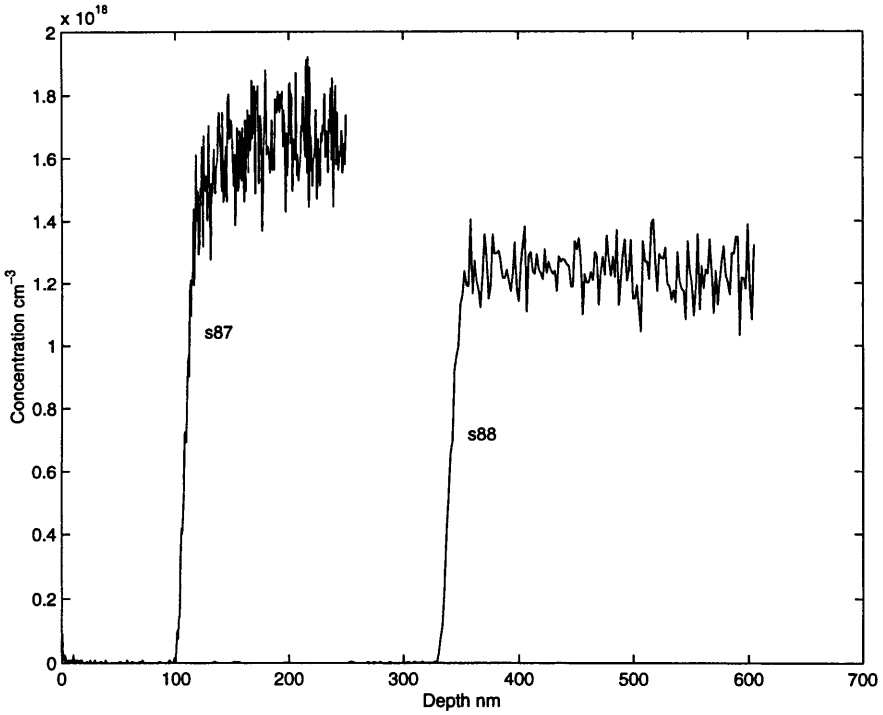

Figure 49: SIMS characteristics

As seen from the results of the study, the agreement between the model and experiment is very excellent for As samples, with sub-50 nm sample not presenting any difficulties. The agreement is also quite good for Sb. It is also seen that the doping level is accurately determined in N^+ wafers. In fact, the results achieved on Sb wafers are of particular significance due to the difficulty they present in characterization by optical means. Sb-doped epitaxial wafers are rather important in the IC industry due to the fact that they significantly reduce the vertical and lateral autodoping effects [63]. The steepness of the doping profile for Sb is apparent when comparing the SIMS data of Figure 49 to the As and particularly B-doped wafers. However, the resistivity of Sb wafers is limited on the lower level: 0.01 Ω-cm as compared to 0.0005 Ω-cm for Boron and 0.005 for As and P. At the typical doping level of 10^{18} cm^{-3}, little optical contrast exists between the intrinsic epi and the substrate, essentially eliminating the side-bursts of even relatively thick epitaxial wafers from the traditional FT-IR interferogram measurements. In fact, the author is not aware of any other non-destructive technique capable of measuring 100 nm-class epitaxial films on Sb-doped substrates.

4.6 Results Using Gradual Profile Model: Effects of Transition Layer

As was seen from the previous section, thin sub-0.5 um epi-layer are well described by the abrupt transition model. It would, however, be useful to investigate under what conditions the transition layer profile can be resolved. Thus effects of various profiles on the FT-IR reflectance spectra were studied using a combination of experimental measurements and modeling techniques. To investigate the issue in more detail, a finite element model based on principles described in Section 3 was created, and used to simulate a variety of profiles along with their associated reflectance spectra. Optimization routines using abrupt model were run to determine the effects of the transition profiles. These results are shown in Figure 50 and Figure 51. It is seen from these that the effect of the transition layer profiles becomes apparent when the combined epi-layer/transition region approach and exceed 1 um in thickness, and manifests itself in the

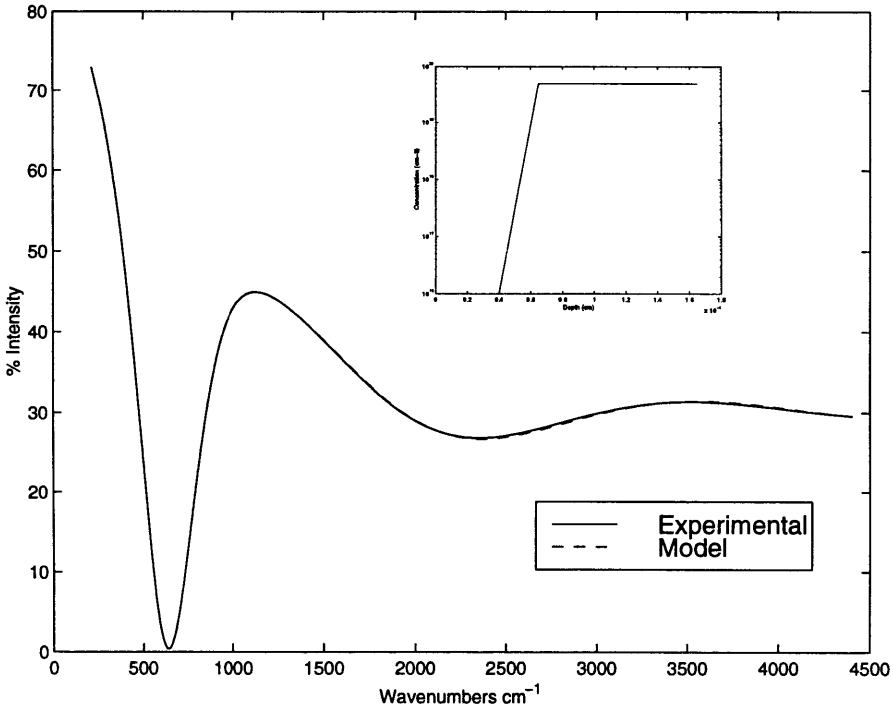

Figure 50: Finite element reflectance spectrum of 0.4 um epi-layer with 0.3 um transition profile

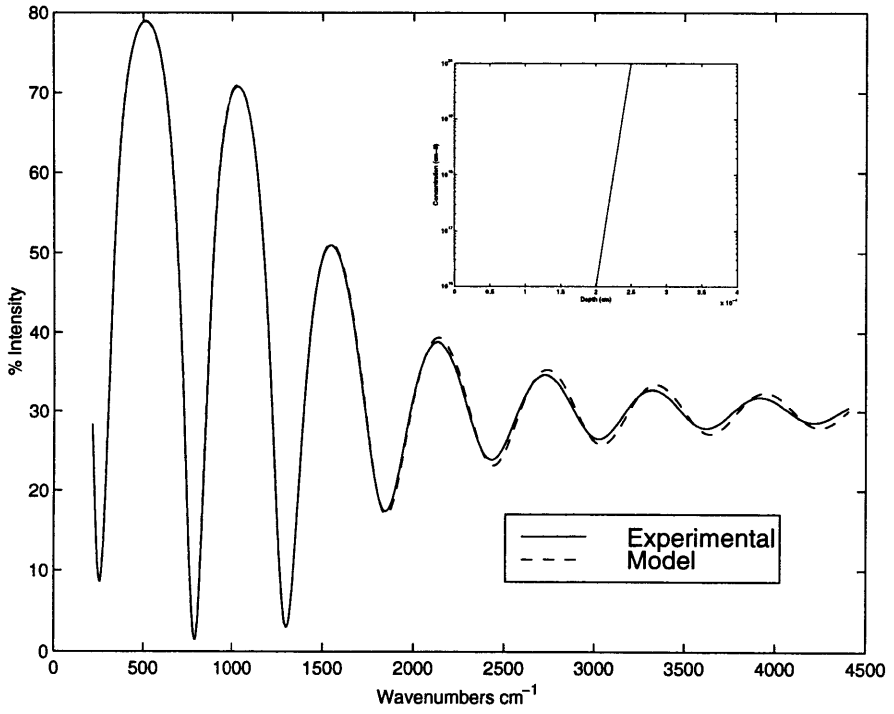

Figure 51: Finite element reflectance spectrum of 2 um epi-layer with 0.4 um transition profile

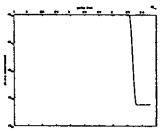

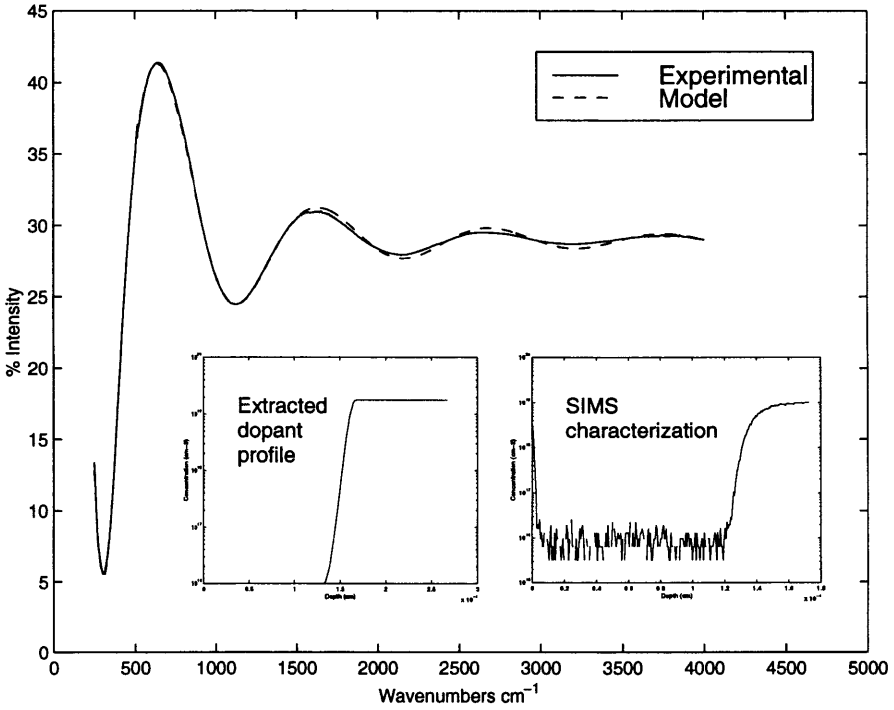

Figure 52: Profile extraction for sample SEC1

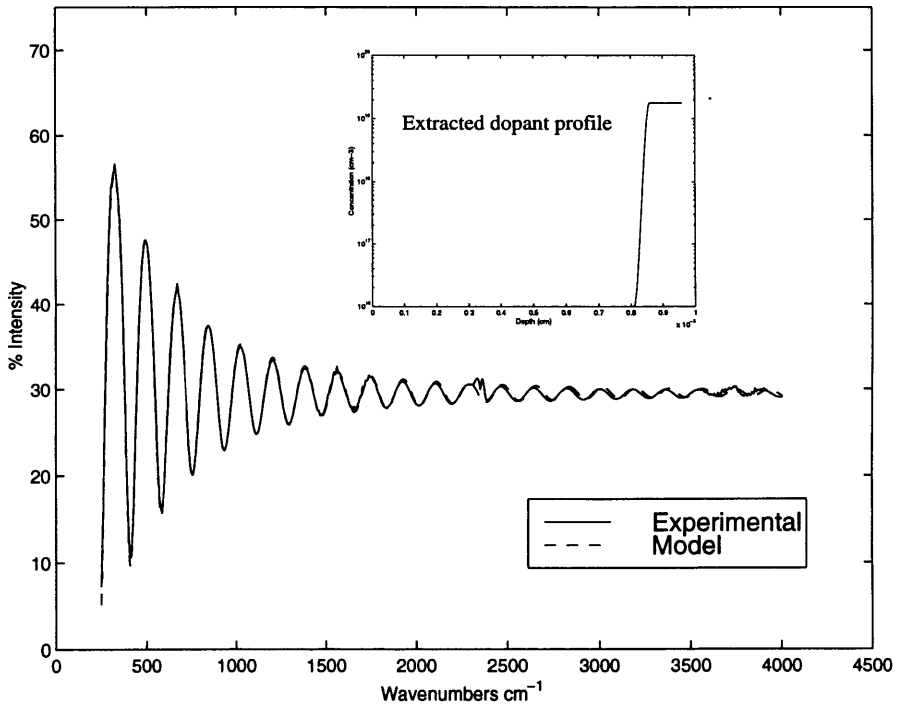

Figure 53: Profile extraction for sample SED7

damping of the amplitude of the interference fringes at the higher wavenumber range. Stated differently, when the combined epi-layer/transition region is reduced below 1 um in thickness, there is an equivalent combination of abrupt epi-layer/substrate which produce virtually identical reflectance spectrum.[20] This is also confirmed by the experimental measurements on thicker epi-layer samples, as shown in Figure 52 and Figure 53.

[20] This result also applies to infrared ellipsometry.

4.7 Extension to Non-Epitaxial Structures: Modeling Shallow Junctions

Although the discussion thus far has been restricted to FT-IR spectrometry of thin silicon epi-layers, it is clear that the methods and models described here are applicable to any semiconductor structure where an optical contrast exists in the IR range (50 wavenumbers to 7000 wavenumbers) due to the presence of free carriers created by the introduction of dopants. One type of such structure which is of importance in IC fabrication are shallow junctions.

The formation of ultra-shallow junctions for MOSFET source/drain structures via ion implantation is one of today's most difficult doping applications for the IC industry. The newly issued 1997 edition of the National Roadmap for Semiconductors specifically notes that the ability to produce highly doped and fully activated shallow junctions is one of the five most difficult challenges for pre-2006 front-end fabrication processes. The junction depth for today's 250 nm technology is typically 100-200 nm [3], scaling to 40-80 nm for the 100 nm technology of 2006. Such scaling requires the development of the accompaning metrology tools. However, the current characterization tools have reached a point where the industry is seeking new and novel ways of measuring the junction depth and dopant concentration [59]. While the key technique, SIMS, is still used, it is being impacted by the trend. This is due to the fact that for the sub-100 nm-type junctions, the typical sputter rate of several hundred Å/min generates insufficient number of data points and thereby causes substantial uncertainties to the doping profile and the depth resolution [13]. Although the improvements to SIMS are being pursued, it still has disadvantages in being a slow, tedious and destructive technique subject to considerable variation in its results. In addition, as SIMS detects the ionized impurities, it does not provide information on the state of carrier activation in the junction region.

On the other hand, FT-IR is a fast, non-destructive technique, sensitive to the free carrier concentrations, and, in conjunction with the models and methods so far presented, capable of resolving very thin (10 nm – class) films, and thus could be suitable to the challenges of the

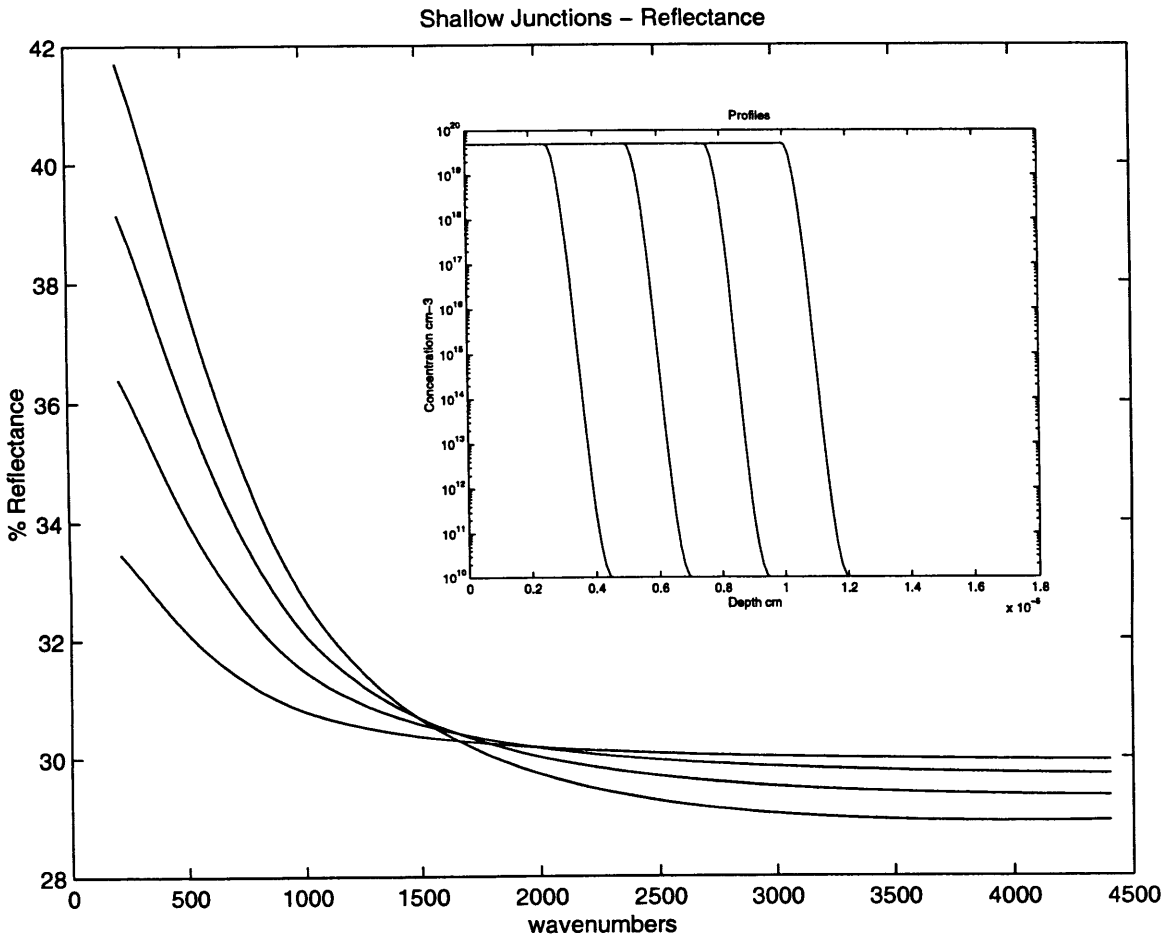

Figure 54 Reflectance Spectra of ultra-shallow junctions

shallow junction metrology. This is evident in the Figure 54, which shows simulated spectra of a series of hypothetical ultra-shallow junction-like profiles. The sensitivity of this method could be further increased by extending the wavenumber range to the lower limit (toward 50 wavenumbers, for example).

4.8 Concluding Discussion

It is quite clear from the results presented in this Chapter that FT-IR in the reflectance mode, augmented with carefully constructed material models and signal processing and optimization algorithms can be used as an accurate tool for non-destructive thickness measurement of very thin silicon epi-layers. Although the thinnest epi sample measured was 47 nm, the method is capable

of substantially better resolution. This is evident from the results of the sensitivity analysis as shown in Figure 55. Given the accuracy of the modeling achieved in this work, it would not be an exaggeration to claim 10 nm film thickness resolution with a few nm precision. As an added benefit of this method, the information on doping concentration and resistivity, mobility and relaxation time is provided as well. The latter parameters correlate well with the results of SIMS characterization and 4-Pt probe measurements for N^+ samples. While the substrate dopant concentration of boron samples is overestimated by the technique, this limitation could probably be resolved by utilizing a more comprehensive model of optical constants in heavily doped silicon which would include the energy dependence of the relaxation time and the interband transitions into the split-off valence band as discussed in Chapter 3.

The instrument is also able to resolve the transition layer profile for thicker (1 um and above) epi-layers. Although silicon epi-layers were the focus for this study, the technique is applicable to other semiconductor structures with optical contrast due to the differences in doping levels. Of such, ultra-shallow junctions appear to be a particularly well-suited candidate.

Potential for *In-situ* Applications

The work carried out in this thesis was restricted to *Ex-situ* measurements and focused on the instrument's and model's ability to reach ultimate limits of film thickness and optical contrast. However, the technique has obvious applicability for *In-situ* measurements due to it's non-contact, non-destructive nature. *In-situ* requirements, however, bring along certain challenges,

which are not present in *Ex-situ* applications, and a certain amount of research would need to be performed in order to develop method to overcome or cope with the limitations imposed by these challenges [64]. One difficulty lies in the emission of infrared radiation during CVD process, which would interfere with the infrared source of FT-IR. Another difficulty has to do with optical properties of the window material of the CVD reactor and the build-up of residuals during epitaxial process. Even if optical window could be characterized with sufficient accuracy, the

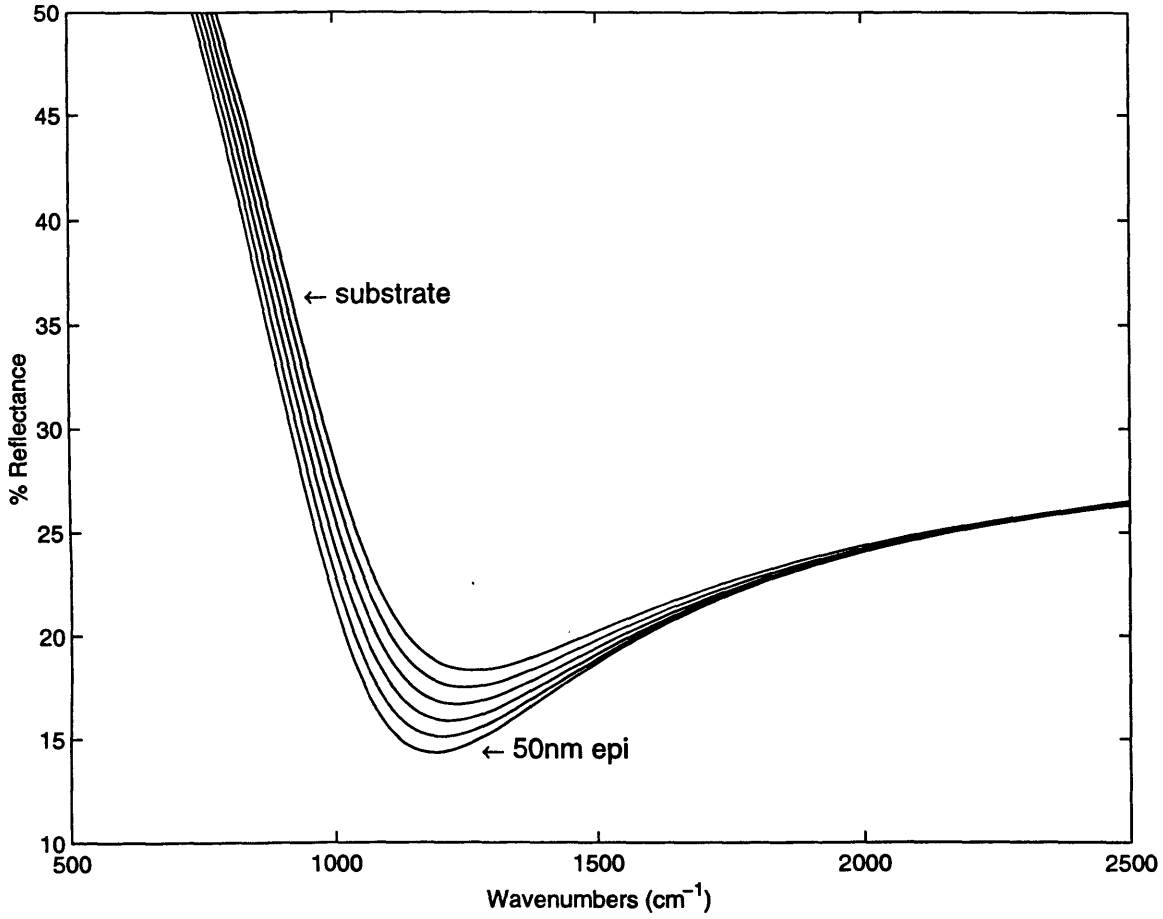

Figure 55: Sensitivity analysis of ultra-thin silicon epi-layers

residuals would probably produce enough of a change in the window optical properties to make measurements problematic. Yet another potential problem may lie in the sample rotation during a typical CVD process which could cause problems with alignment. Performing measurements at a relatively low angle of incidence, as is usually the case in a typical FT-IR application would minimize the misalignment somewhat, but its effects would still need to be investigated. However, none of these difficulties should in principle prevent the method from being successfully used for real-time *In-situ* monitoring and process control applications.

Potential Use in Selective Epitaxy / Patterned Wafers

The work presented is limited to blanket films. While blanket epitaxial wafers certainly constitute an important sector of the epitaxial field, being able to extend the methods developed in this thesis to selective epitaxial structures as used in the elevated S/D MOSFETs of the type shown in Figure 1 would be of obvious interest. Like wise, the ability to characterize patterned shallow junctions would be extremely attractive to the IC industry. It must be clear, however, that the measurements on patterned wafers present very serious challenges. Patterned wafers often assume very complicated structures, which vary widely in geometry, number of layers, and isolation shemes. The quest for being able to perform non-destructive 3-dimensional profiling of these structures remains the Holy Grail of the semiconductor industry [3], and it is unlikely that a single comprehensive method could be found in the near future to address this need[21]. Despite the complexity of the task, a more restrictive solution to the problem could be attempted along two avenues.

One avenue would be to attempt to focus the infrared radiation onto individual structure. For this a tunable infrared laser source would have to be utilized. Even if such device is available, the latteral resolution would be limited to several microns at best. For incoherent source as utilized in the typical FT-IR, the "focusing" would have to be accomplished by a pin-hole illumination. Reducing the pin-hole diameter, however, causes severe degradation in the transmitted beam area leading to the loss of signal-to-noise ratio (SNR). Usually, the pin-hole would be restricted to about 10-50 um in diameter. A more promising, as well as interesting, idea would be to research near-field infrared microscopy. Near field optical microscopy, or optical proximity probes have been utilized with success in some medical applications to overcome the Abbe difraction limitation. Substantial amount of research would need to be performed to extend this technology into the infrared, including suitable sources, detectors, and fiber-optical components. However, if

[21] Human potential for coming out with creative ideas should never be underestimated

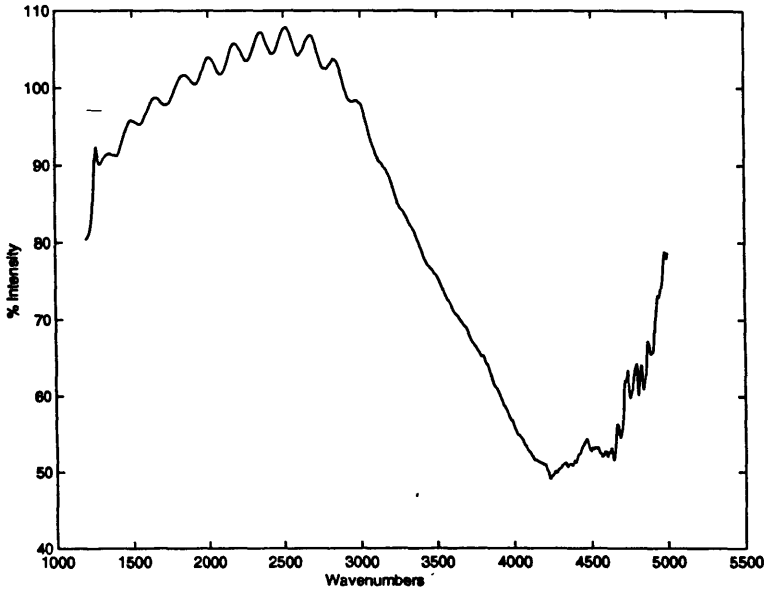

Figure 56 Reflectance spectrum of 1 Gb DRAM trench regions: trench dimension: 0.2umX0.2um, trench depth 5.2 um

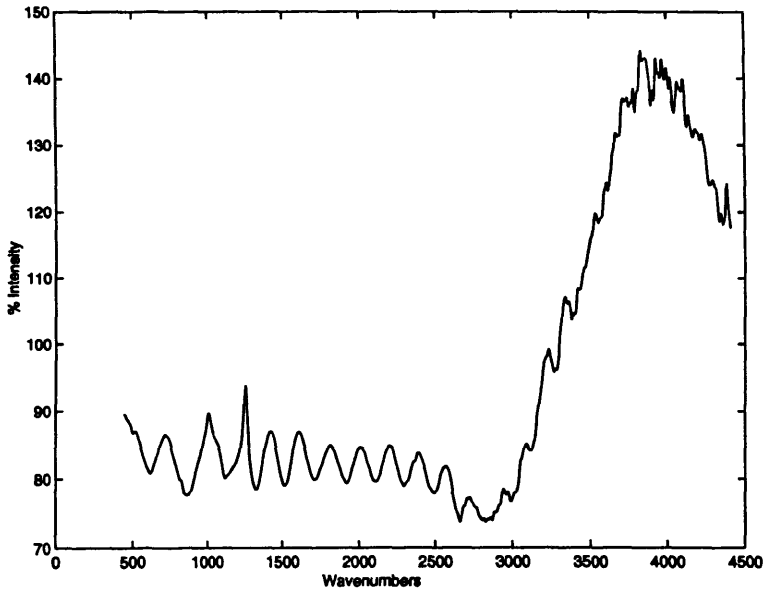

Figure 57: Reflectance spectrum from the above after normalization by the refelectance spectrum taken from the isolation area on the chip: characteristic oscillations clearly observed

successful, such technology would enable significant advances in non-contact 3-D dopant profiling and material characterization [65].

Going to the other extreme as compared to the infrared microscopy is the use of wide-area illumination augmented with more involved models accounting for the lateral features of the patterned wafers. Although the finished patterned wafer can certainly assume a complicated 3-D shape, in the initial stage of fabrication the geometry is often far simpler. In many instances, large areas of the chip are taken up by regular, periodic structures, such as transistor arrays, or silicon trenches typical of DRAM technology. In this case, a decoupling between the vertical and the latteral geometries may be achieved, and a modeling effort may be attempted to account for the lateral features with certain measure of confidence. This is illustrated in Figure 56 and Figure 57 showing the reflectance spectrum from a 1 Gb DRAM test wafer with the IR illumination directed at the trench area. Even though the area of the individual trenches is very small, the interference from the top and bottom surfaces of the trench is clearly observable, and enables trench depth to be estimated. The only other method which will allow the trench depth to be characterized in electron microscopy, which is unsuitable to in-line or *In-situ* applications. This simple example illustrates the potential power of the infrared technique, which, when coupled with appropriate models and algorithms can lead to interesting possibilities.

Chapter 5.

Infrared Spectroscopic Ellipsometry

5.1 Introduction

In this Chapter we extend the methods and models developed thus far to the field of infrared ellipsometry (IRSE). As mentioned elsewhere, IRSE results from a combination of FT-IR with ellipsometry, and, as such, is a natural extension of the basic FT-IR spectrometry. Particularly, the linear system theory of FT-IR and the models and structures of thin epi-layers are directly applicable. IRSE is a recent technique, whose success is largely dependent of the methods which allow the measurements to be made with imperfect components. On the other hand, IRSE is, potentially, significantly more sensitive technique than FT-IR, and possesses several advantages beyond the accuracy and resolution.

We shall introduce the basic principles of IRSE, relying on the theoretical background of FT-IR developed in Chapter 2 and extending it with methods suited for treatment of polarization properties of stochastic light. This is followed by the description of methods to account for non-ideal behavior of the polarizing components of the instrument, which are crucial to this method. We then apply the models and structures of Chapter 3 to the IRSE measurements. Thus we will be in a position to perform direct comparisons of FT-IR vs. IRSE. In the spirit of Chapter 4, we

conclude by discussion of the technique's sensitivity and resolution, and its applicability to some epitaxial-like structures of interest to the IC industry.

5.2 Principles of IRSE with Ideal Components

The transformation of the basic FT-IR spectrometer into infrared ellipsometer is accomplished via the inclusion of two additional infrared polarizers. The first element, known as the *polarizer*, is used to set the polarization of the light incident onto the sample to a pre-determined state. The second element, known as the *analyzer*, enables the polarization state of the reflected radiation to be determined by measuring its spectrum according to the setting of the analyzer azimuth. As compared with FT-IR spectrometry, IRSE possesses two additional degrees of freedom allowed by the independent settings of the polarizers. Utilizing the polarizers, the ellipsometric parameters Ψ and Δ can be determined.

The transformation of polarized light by an optical element such as polarizer may be described via matrix methods. Let **E** be the incoming electric field vector, and **E'** the outgoing vector as transformed by the optical element. Then the outgoing vector is given:

$$\mathbf{E}' = T\mathbf{E} \tag{5.1}$$

where the transformation matrix T is the so-called Jones matrix of the element [66]. In the case of a cascade of elements, the overall Jones matrix is given by the product of individual matrices. Consider the action of an ideal linear polarizer, whose transmission axis is oriented at an angle θ with respect to a particular Cartesian coordinate system. Thus the transmission axis is given by the unit vector $\vec{p} = \begin{pmatrix} \cos\theta \\ \sin\theta \end{pmatrix}$. If the incoming electric field is $\mathbf{E} = \begin{pmatrix} E_x \\ E_y \end{pmatrix}$, then the outgoing field is given as:

$$\mathbf{E}' = (\vec{p} \bullet \mathbf{E})\vec{p} = (\cos\theta E_x + \sin\theta E_y)\begin{pmatrix} \cos\theta \\ \sin\theta \end{pmatrix} = \begin{pmatrix} \cos^2\theta E_x + \sin\theta\cos\theta E_y \\ \cos\theta\sin\theta E_x + \sin^2\theta E_y \end{pmatrix} \tag{5.2}$$

The Equation 5.2 can be re-written in the matrix form as

$$\mathbf{E}' = T_1\mathbf{E} = \begin{pmatrix} \cos^2\theta & \sin\theta\cos\theta \\ \sin\theta\cos\theta & \sin^2\theta \end{pmatrix}\begin{pmatrix} E_x \\ E_y \end{pmatrix} \tag{5.3}$$

where T_1 is the Jones matrix of the linear polarizer.

Likewise, it is easily seen that the Jones matrix of a reflecting material sample is given as:

$$T_r = \begin{pmatrix} r_x e^{i\delta_x} & 0 \\ 0 & r_y e^{i\delta_y} \end{pmatrix} \tag{5.4}$$

Thus, the electric field at the output of the 3-element cascade of IRSE/sample (two polarizers and the sample) is given as

$$\mathbf{E}_d = T_2(\theta_2)T_rT_1(\theta_1) \tag{5.5}$$

For the IRSE measurements, the first polarizer is fixed at 45 degrees, and the second polarizer, and the intensity at the detector of FT-IR is measured at 3 settings of the analyzer: 0, 45, and 90 degrees. In this case, the Jones matrices of the two polarizers assume simple forms, and the intensity at the detector $I_d = \left|E_d E_d^*\right|$ is readily obtained as:

$$I(0^0) = r_x^2 I_0 \tag{5.6a}$$

$$I(90^0) = r_y^2 I_0 \tag{5.6b}$$

$$I(45^0) = \frac{1}{2}(r_x^4 + r_y^4 + 2r_x^2 r_y^2\cos\Delta)^{1/2} I_0 \tag{5.6c}$$

where $\Delta = \delta_x - \delta_y$ and $\tan\Psi = \frac{r_x}{r_y}$, and I_0 is a constant.

Thus we have the following equations for Ψ and Δ:

$$\frac{I(0^0)}{I(90^0)} = (\tan\psi)^2 \tag{5.7a}$$

$$\frac{I(45^0)}{I(90^0)} = \frac{1}{2}[1 + (\tan\psi)^4 + 2(\tan\Psi)^2\cos\Delta]^{1/2} \tag{5.7b}$$

Solving Eq. 5.7 a-b, the ellipsometric parameters *tan*ψ and *cos*Δ are finally obtained. We also notice that as only *cos*Δ is provided, there is an ambiguity in Δ. This, however, may be resolved,

if a compensator, or retarder, is used as the fourth element in the optical train. A retarder serves to introduce an additional phase shift δ to Δ[22]. If $\delta = 90^0$, $cos\Delta$ is changed into $sin\Delta$ in the equations above. Thus, repeating the measurements with and without the retarder, the ambiguity is removed. The retarder, or compensator, may be characterized by the Jones matrix:

$$T_{ret}(\delta) = \begin{pmatrix} e^{-i\delta_x} & 0 \\ 0 & e^{-i\delta_y} \end{pmatrix} \tag{5.8}$$

The additional benefit of using a retarder is that higher sensitivity is achieved at small values of Δ. This enables one to study highly transparent samples, such as very thin glass, as well as highly reflecting ones, such as metal mirrors, which would be virtually impossible by conventional optical methods.

5.3 IRSE with Imperfect Components

The treatment in the previous section assumed ideal behavior of the main polarizing components of the FT-IR/ellipsometer system, such as the source/beam splitter, and the polarizers. This, of course, is not the case in real world. In this section, we describe the methods that allow the non-idealities of the source/beam splitter, and the polarizers to be accounted for.

Determining Polarizing Properties of FT-IR

It was shown in Chapter 2 that the polarizing properties of FT-IR, particularly the beam splitter, but also of the source, had to be taken into account to achieve the results demonstrated in Chapter 4. This was done by making assumptions about these according to parameters α and β. Thus the

[22] A retarder is analogous to an all-pass filter in signal processing, which introduces a phase shift while leaving the amplitude unchanged.

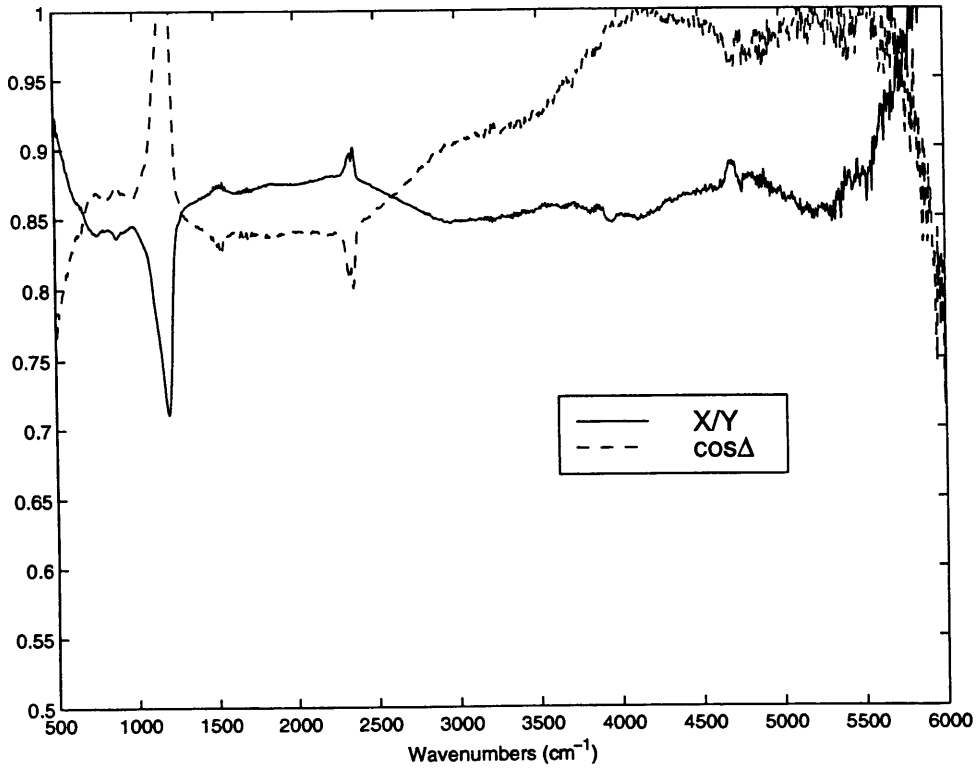

Figure 58: Polarization characteristics of FT-IR, assuming ideal polarizers. X/Y is the ratio of *s* and *p* transmissibities, and Δ is the phase shift difference

measurement values as contained in the optimization vector **z** are subject to deviations of these assumptions from the actual polarization characteristics of FT-IR elements such as the beam splitter, which vary depending on the design. In the case of IRSE, polarization properties of FT-IR can be determined directly, thus removing, at least to the first approximation, the last remaining instrument system function of FT-IR from the measurements.

The determination of the polarizing properties of FT-IR follows the procedure described by the Equations 5.6-7 of the previous section, except the measurements are performed in the straight-through configuration, with no sample in the path. The Jones matrix of the FT-IR/beam splitter can still be modeled as

$$T_{bs}(k)=\begin{pmatrix}\sqrt{X}e^{-i\delta_x} & 0\\ 0 & \sqrt{Y}e^{-i\delta_y}\end{pmatrix} \tag{5.9}$$

where X and Y are (frequency-dependent) transmissivity coefficients of the FT-IR system for *s*- and *p*- polarization components. Removing the polarizer, and taking intensity measurements at 0, 45, and 90 degrees of the analyzer, we determine the ratio $\frac{X}{Y}$ and the phase shif t Δ as:

$$\frac{I(0^0)}{I(90^0)}=\frac{X}{Y};\qquad \frac{I(45^0)}{I(90^0)}=\frac{1}{2}\left[1+\left(\frac{X}{Y}\right)^2+2\left(\frac{X}{Y}\right)\cos\Delta\right]^{1/2} \tag{5.10}$$

Figure 58 shows the measured characteristics of a beam splitter used in one of the FT-IR instruments utilized by the author.

Stokes Parameters and Mueller Matrices

In order to account for the imperfections of the polarizers, we shall now take advantage of two additional techniques which are more suitable and more powerful in describing the transformations of partially polarized light by optical components than the Jones matrix method.

The first, Stokes parameter method [26], replaces the covariance matrix **J** of Eqn. 2.36 by a 4-component vector S whose components $S_{0\text{-}3}$ are:

$$s_0 = J_{xx} + J_{yy} \tag{5.11a}$$

$$s_1 = J_{xx} - J_{yy} \tag{5.11b}$$

$$s_2 = J_{xy} + J_{yx} = 2\,\mathrm{Re}(J_{xy}) \tag{5.11c}$$

$$s_3 = i(J_{yx} - J_{xy}) = 2\,\mathrm{Im}(J_{xy}) \tag{5.11d}$$

This can be described in matrix form as

$$\mathbf{S}=\mathbf{AJ}=\begin{pmatrix}s_0\\ s_1\\ s_2\\ s_3\end{pmatrix}=\begin{pmatrix}1 & 0 & 0 & 1\\ 1 & 0 & 0 & -1\\ 0 & 1 & 1 & 0\\ 0 & -j & j & 0\end{pmatrix}\begin{pmatrix}J_{xx}\\ J_{xy}\\ J_{yx}\\ J_{yy}\end{pmatrix} \tag{5.12}$$

Stokes parameters apply for both coherent and stochastic light. If one considers a monochromatic

wave with E-field given as $\mathbf{E} = \begin{pmatrix} a_1 e^{i\delta_x} \\ a_2 e^{i\delta_y} \end{pmatrix}$, the Stokes vector is obtained as

$$s = \begin{pmatrix} a_1^2 + a_2^2 \\ a_1^2 - a_2^2 \\ 2a_1 a_2 \cos\Delta \\ 2a_1 a_2 \sin\Delta \end{pmatrix} \tag{5.13}$$

Thus Stokes parameters can be assigned physical meaning as follows: s_0 is the total intensity; s_1 is the difference between the *s*- and *p*- polarized intensities (intensities through a linear polarizer oriented at 0^0 and 90^0); s_2 is similar to s_1 but for polarizer at 45^0 and 135^0, and s_3 is the difference between the intensity of light through an element which only passes right-hand circular polarization, and one for left-handed circular polarization.

Similar to the covariance matrix **J**, partially polarized light can be represented as the sum of the Stokes vector for totally polarized light, and Stokes vector for fully unpolarized (natural) light:

$$s = s_p + s_u \tag{5.14}$$

where $s_u = s_0 \begin{pmatrix} 1 \\ 0 \\ 0 \\ 0 \end{pmatrix}$

Using methods described in Chapter 2, the Stokes vectors s_p and s_u may be uniquely obtained from the general Stokes vector $s = \begin{pmatrix} s_0 \\ s_1 \\ s_2 \\ s_3 \end{pmatrix}$ as:

$$s_u = \begin{pmatrix} s_0 - (s_1^2 + s_2^2 + s_3^2)^{1/2} \\ 0 \\ 0 \\ 0 \end{pmatrix}; \quad s_p = \begin{pmatrix} (s_1^2 + s_2^2 + s_3^2)^{1/2} \\ s_1 \\ s_2 \\ s_3 \end{pmatrix} \tag{5.15}$$

and the degree of polarization is given as before:

$$P = \frac{I_p}{I_{tot}} = \frac{(s_1^2 + s_2^2 + s_3^2)^{1/2}}{s_0} \tag{5.16}$$

While the Stokes vector contains equivalent amount of information as the covariance matrix, the real advantage of Stokes vector treatment comes from its use in linear transformations through optical elements: $s' = \mathbf{M}s$, where **M** is a 4 by 4 matrix containing the characteristics of the optical component. The matrix **M** is known as the Mueller matrix [67]. Similarly to the Jones matrix, the cascade of the optical systems is characterized by the product of the individual Mueller matrices.

Mueller matrix representation is more powerful than the Jones matrix formalism, because it allows to treat transformation of partially polarized light through *depolarizing* optical systems, which is something that Jones matrix can not do. A depolarizing optical system is one, which can randomize or decorrelate the *x*- and *y*- electric field components of the incident wave. Using relatively straightforward linear algebra arguments, one may show that for *non-depolarizing* system, the degree of polarization of the transformed light P_o is equal or greater than the degree of polarization of the incoming wave P_o. For a *depolarizing* system, $P_0 \leq P_i$. The physical mechanisms responsible for depolarization may include incoherent scattering processes, such as reflections from rough surfaces. Mueller matrix of non-depolarizing system may be obtained from the corresponding Jones matrix as:

$$\mathbf{M} = \mathbf{A}(\mathbf{T} \times \mathbf{T}^*)\mathbf{A}^{-1} \tag{5.17}$$

where **A** is defined as Eq. 5.12, and $\mathbf{T} \times \mathbf{T}^*$ is the direct product of two 2 by 2 transformation matrices, resulting in a 4 by 4 matrix. It is seen from 2.36 that the Mueller matrix of a non-depolarizing system is Hermitian, and only 7 of its 16 components are independent. For the case of depolarizing system, all 16 components may be independent.

In addition to its ability to describe depolarizing systems, Stokes vector/Mueller matrix formalism is convenient when dealing with non-depolarizing systems, since the resulting intensity

of transformed wave is readily given by the first component of the outgoing Stokes vector.

Mueller Matrix of Imperfect Polarizer

A perfect linear polarizer has 100% transmission along its major axis, and 0% transmission along its minor axis. An imperfect linear polarizer may be characterized by its maximum and minimum transmittances τ_M and τ_m, respectively, for its major and minor axis. It is convenient to use the transformed parameters

$$\cos 2\vartheta = \frac{\tau_M - \tau_m}{\tau_M + \tau_m} \tag{5.18a}$$

and

$$\sin 2\vartheta = \frac{2\sqrt{\tau_M \tau_m}}{\tau_M + \tau_m} \tag{5.18b}$$

Then, using 5.17, one may obtain the Mueller matrix of an imperfect linear polarizer with major axis orientation θ as:

$$\mathbf{M}_{pol} = \frac{\tau_M + \tau_m}{2} \times \begin{pmatrix} 1 & \cos 2\vartheta \cos 2\theta & \cos 2\vartheta \sin 2\theta & 0 \\ \cos 2\vartheta \cos 2\theta & \cos^2 2\theta + \sin^2 2\theta \sin 2\vartheta & \sin 2\theta \cos 2\theta(1 - \sin 2\vartheta) & 0 \\ \cos 2\vartheta \sin 2\theta & \sin 2\theta \cos 2\theta(1 - \sin 2\vartheta) & \sin^2 2\theta + \cos^2 2\theta \sin 2\vartheta & 0 \\ 0 & 0 & 0 & \sin 2\vartheta \end{pmatrix} \tag{5.19}$$

Mueller Matrix of Material Sample

A Mueller matrix for a material sample characterized by the Fresnel reflection coefficients r_s and r_p and ellipsometric parameters ψ and Δ is given by 5.17 as

$$\mathbf{M}_{samp} = \frac{|r_s|^2 + |r_p|^2}{2}\begin{pmatrix} 1 & -\cos 2\Psi & 0 & 0 \\ -\cos 2\Psi & 1 & 0 & 0 \\ 0 & 0 & \sin 2\psi \cos\Delta & \sin 2\psi \sin\Delta \\ 0 & 0 & -\sin 2\psi \sin\Delta & \sin 2\psi \cos\Delta \end{pmatrix} \quad (5.20)$$

Model of IRSE with Imperfect Components

Once the Mueller matrices of the individual components are obtained, the overall light transformation is given in terms of the Stokes vector

$$S_d = \mathbf{M}_{pol}\mathbf{M}_{samp}\mathbf{M}_{anal}S_{FT-IR} \quad (5.21)$$

where $S_{FT\text{-}IR}$ is the Stokes vector for the partially polarized light produced by the FT-IR, and S_d is the Stokes vector of the light impinging on the detector. If we make the assumption that the FT-IR is illuminated with *natural* light, the Stokes vector at the output of FT-IR is given as:

$$S_{FT-IR} = \begin{pmatrix} s_0 \\ s_1 \\ 0 \\ 0 \end{pmatrix} \quad (5.22)$$

We make assumption that the two polarizers are *matched*, so $\vartheta_{pol} = \vartheta_{anal}$ as given in Equations 5.18a-b. The sought Stokes vector S_d is obtained by carrying out the multiplication, which is given in Appendix A.

If one of the polarizers is set at 45^0, the intensity at the detector as a function of the second polarizer angle θ is given by the first element of S_d as (Appendix A):

$$\begin{aligned} s_0{}^d = K[&s_0 + (\cos 2\vartheta \cos 2\theta)s_1 - \cos 2\psi\{(\cos 2\vartheta \cos 2\theta)s_0 + (\cos^2 2\theta + \sin^2 2\theta \sin 2\vartheta)s_1\} \\ &+ \cos 2\vartheta\{(\cos 2\vartheta \sin 2\theta)s_0 + \sin 2\theta \cos 2\theta(1 - \sin 2\vartheta)s_1\}\sin 2\psi \cos\Delta] \end{aligned} \quad (5.23)$$

where $$K = (\frac{\tau_M + \tau_m}{2})(\frac{|r_s|^2 + |r_p|^2}{2}) \quad (5.24)$$

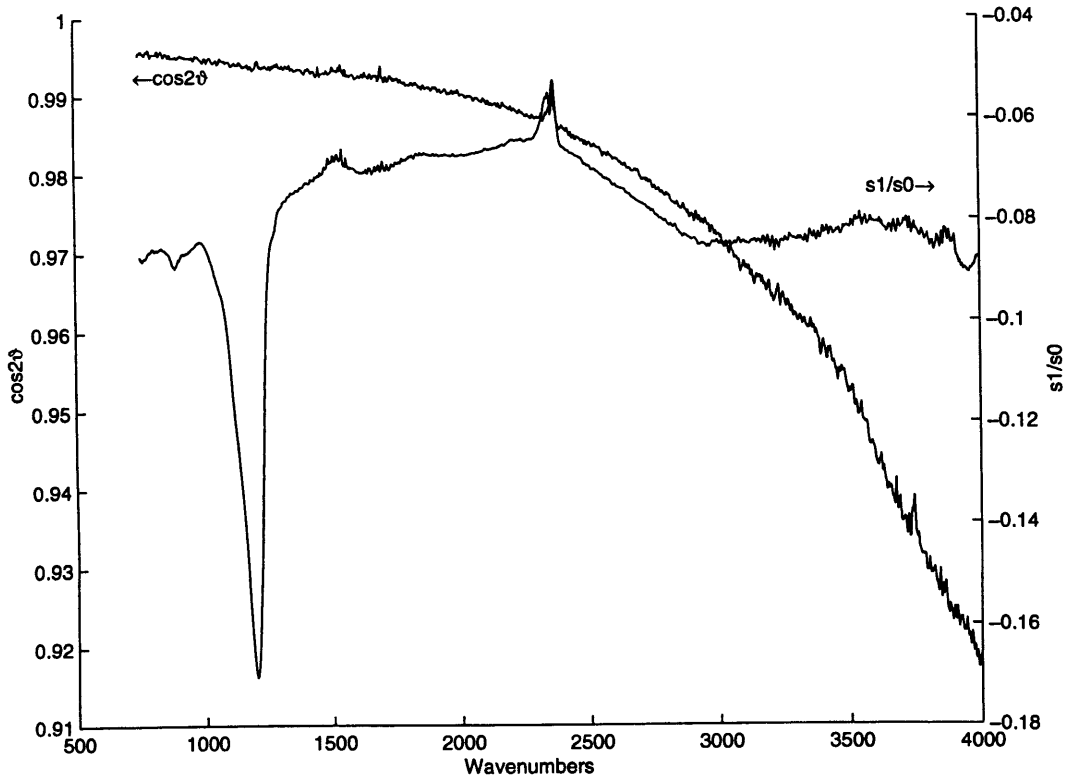

Figure 59: Characteristics of the polarizers and state of polarization of radiation emitted from FT-IR. Cos2υ indicates perfection of the polarizer, which is ideally unity, and s1/s0 is a measure of light polarization fromFT-IR, which is zero ideally.

Correcting for IRSE Non-idealities

Equation 5.23 produces the intensity measured at the detector as a function of the analyzer setting θ. It is influenced by the imperfections of the polarizers given by ϑ, and the polarizing properties of FT-IR given by s_0 and s_1. These can be corrected for by first using IRSE without sample, in straight-through configuration, and measuring the intensity at the 0, 45, 90, and 135 degrees setting of the analyzer. In this case, Equation 5.23 simplifies to produce:

$$I_d(0^0) = s_0{}^d(0^0) = K[s_0 + (\cos 2\vartheta)s_1] \qquad (5.25a$$

$$I_d(45^0) = K[1 + (\cos^2 2\vartheta)s_0] \qquad (5.25b)$$

$$I_d(90^0) = K[s_0 - (\cos 2\vartheta)s_1] \qquad (5.25c)$$

$$I_d(135^0) = K[1-(\cos^2 2\vartheta)s_0] \tag{5.25d}$$

which can be further used to produce:

$$\frac{I_0(0)-I_0(90)}{I_0(0)+I_0(90)} = (\cos 2\upsilon)\frac{s_1}{s_0} \tag{5.26a}$$

$$\frac{I_0(45)-I_0(135)}{I_0(45)+I_0(135)} = \cos^2 2\upsilon \tag{5.26b}$$

from where the imperfections are obtained.

Figure 59 illustrates the non-idealities of an IRSE instrument used in this thesis.

Determining Ellipsometric Parameters with Real IRSE Instrument

Using Equation 5.23 with sample present, the following relations are obtained:

$$I_d(0^0) = s_0{}^d(0^0) = Ks_0[1-\cos 2\vartheta\cos 2\psi + (-\cos 2\psi + \cos 2\vartheta)\frac{s_1}{s_0}] \tag{5.27a}$$

$$I_d(45^0) = Ks_0[1-(\sin 2\vartheta)\frac{s_1}{s_0}\cos 2\psi + \cos^2 2\vartheta \sin 2\psi \cos\Delta] \tag{5.27b}$$

$$I_d(90^0) = Ks_0[1+\cos 2\vartheta\cos 2\psi + (-\cos 2\psi - \cos 2\vartheta)\frac{s_1}{s_0}] \tag{5.27c}$$

$$I_d(135^0) = Ks_0[1-(\sin 2\vartheta)\frac{s_1}{s_0}\cos 2\psi - \cos^2 2\vartheta \sin 2\psi \cos\Delta] \tag{5.27d}$$

which can be further used to produce:

$$\frac{I_s(0)-I_s(90)}{I_s(0)+I_s(90)} = -\frac{(\cos 2\psi - s_1/s_0)\cos 2\upsilon}{(1-\cos 2\psi)s_1/s_0} = A \tag{5.28a}$$

$$\frac{I_0(45)-I_0(135)}{I_0(45)+I_0(135)} = \frac{\cos^2 2\upsilon \sin 2\psi \cos\Delta}{1-(\cos 2\psi \sin 2\upsilon)s_1/s_0} = B \tag{5.28b}$$

from which the amplitude ratio ψ and phase shift Δ are obtain as follows:

$$\cos 2\psi = \frac{A-(\cos 2\upsilon)s_1/s_0}{(As_1/s_0)-\cos 2\upsilon} \tag{5.29a}$$

$$\sin 2\psi \cos\Delta = \frac{B(1-\cos 2\psi\sqrt{1-\cos^2 2\upsilon}\, s_1/s_0)}{\cos^2 2\upsilon} \qquad (5.29b)$$

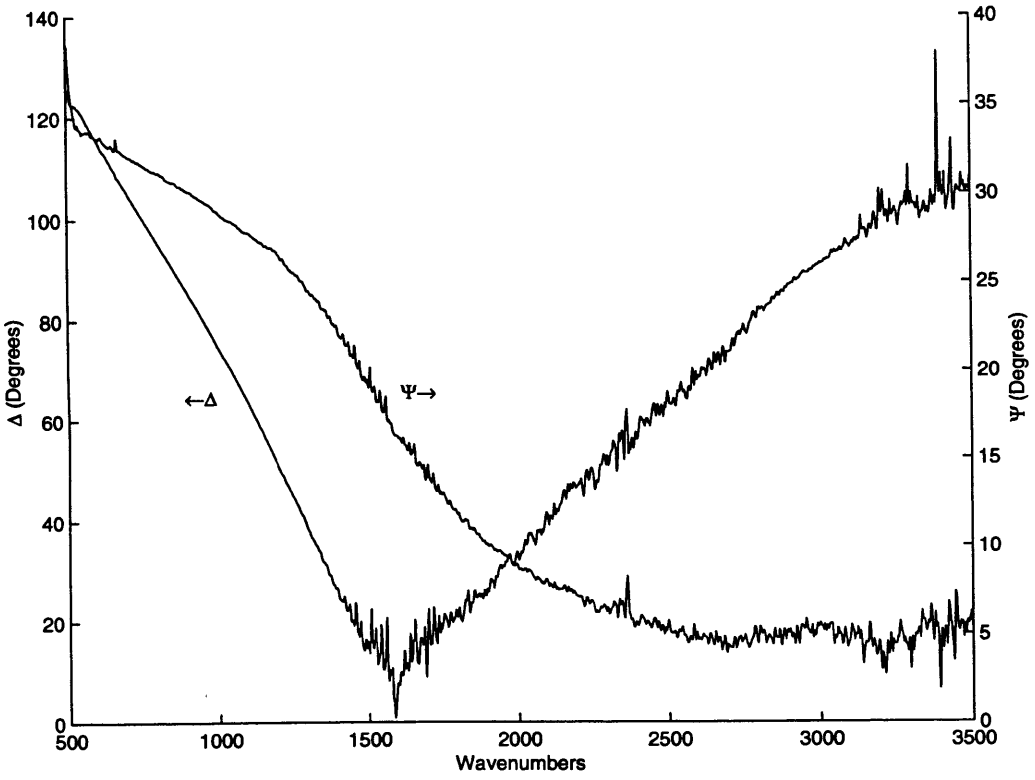

Figure 60: Ellipsometric spectra for sample S52

5.4 IRSE of Thin Silicon Epitaxial Layers

Error! Reference source not found. shows the IRSE spectrum collected from a thin epi-layer sample representative of the wafer matrix described in the previous chapter. Several features of the figure are noteworthy. First, the phase angle, Δ, varies widely across the frequency spectrum. On the other hand, the ratio of amplitudes angle, Ψ, has a much smaller dynamic range. It is the feature of the IRSE measurements that the phase parameter is much more sensitive than the amplitude ratio. In fact, as will be demonstrated, the Δ measurements by IRSE are significantly more sensitive than the reflectance measurements via FT-IR. However, for Ψ, the reverse is true. There are two main reasons for this. First reason is the general fact that measurements of the

phase are more sensitive than those of the amplitude. The second reason has to do with material properties and the angle of incidence. As discussed in Chapter 3, it is of advantage to carry out measurements at high angle of incidence, near the material Brewster angle, which, for intrinsic silicon, is 73.7^0. At the Brewster angle, all the *p*-polarized radiation is transmitted into the sample, and the corresponding Fresnel reflection coefficient is zero. Thus, small deviation in the material refractive index from its intrinsic value will translate in a large change in the phase. On the other hand, for reflectance measurements, and for Ψ measurements, where the amplitudes are measured, it is better to carry out the measurements at a steep angle of incidence, in order to obtain a strong reflection from the surface of the sample and the film-substrate boundary. This is one of the reasons for FT-IR measurements being carried out at a low 30^0 incidence angle[23]. At steep angles of incidence, the Fresnell reflection coefficient is drastically reduced, therefore the corresponding loss of sensitivity.

For these reasons, although ellipsometry is often hyped for its ability to measure two quantities, the amplitude and the phase, independently, thus providing information on the real and imaginary parts of the e-field and the index of refraction, this has to be tempered by the understanding that the two quantities are at the opposite ends with respect to the measurement sensitivity.

Thus, in the discussion which follows, we shall be mainly concerned with the measurements of Δ, and the results presented will be obtained from its spectrum.

Experiment

In this study, we utilized two instruments. Ellipsometer A is an experimental system, where the author took part in design and characterization. System A is based directly on the principles described earlier in the Chapter. At the time the measurements presented in this thesis were taken, the system suffered from two shortcomings, which, while not being major obstacles, limited its

[23] Another reason is to avoid or minimize polarization effects, as discussed in Chapter 3. This was not the issue in this thesis, since polarization affects were accounted for.

flexibility to a certain extent. First was that the system was not equipped with a compensator. As discussed earlier in the Chapter, a compensator, or achromatic retarder, is advantageous in allowing to measure sin(Δ) rather than cos(Δ). This is important if very fine measurements are performed where there is there is little optical contrast between the sample and the ambient, such as highly transparent glass, or when studying properties of highly reflecting samples, such as metal mirrors, or highly doped silicon wafers or very thin epi-layers on highly doped substrates [68]. In the first instance, Δ is near 0^0, while in the second case, which is of interest to us, Δ is near 180^0. Since cos(Δ), which is the normal outcome of IRSE measurement, is relatively insensitive at these values, using the retarder to shift the phase by 90^0 provides obvious advantages. An additional benefit to using IRSE in a two-pass mode, with and without the compensator, is that the phase spectrum Δ(k) may be determined un-ambiguously within the full 360^0 range.

The second shortcoming is that the system was not enclosed, thus purging was not possible. It is advantageous to be able to purge sample compartment of moisture and other extraneous species contained in the ambient environment, which is usually accomplished by running N_2 gas through the sample compartment.

The second system, Ellipsometer B, is a commercial instrument currently being marketed by its manufacturer. It is equipped with a compensator, and has the purge capability. However, it is somewhat limited on the low end of the spectral range to about 600+ wavenumbers (16 um). Since the instrument is located in France, the samples had to be airmailed, which limited the sample space and the author's ability to experiment with different measurement configurations.

The measurements were performed at two angles of incidence. System A utilized 73^0 angle, which is close to the Brewster angle of intrinsic silicon. On the other hand, Brewster angle of the doped silicon declines toward 70^0. Thus System B used 69.56^0 angle, which is closer to the Brewster angle of the doped silicon.

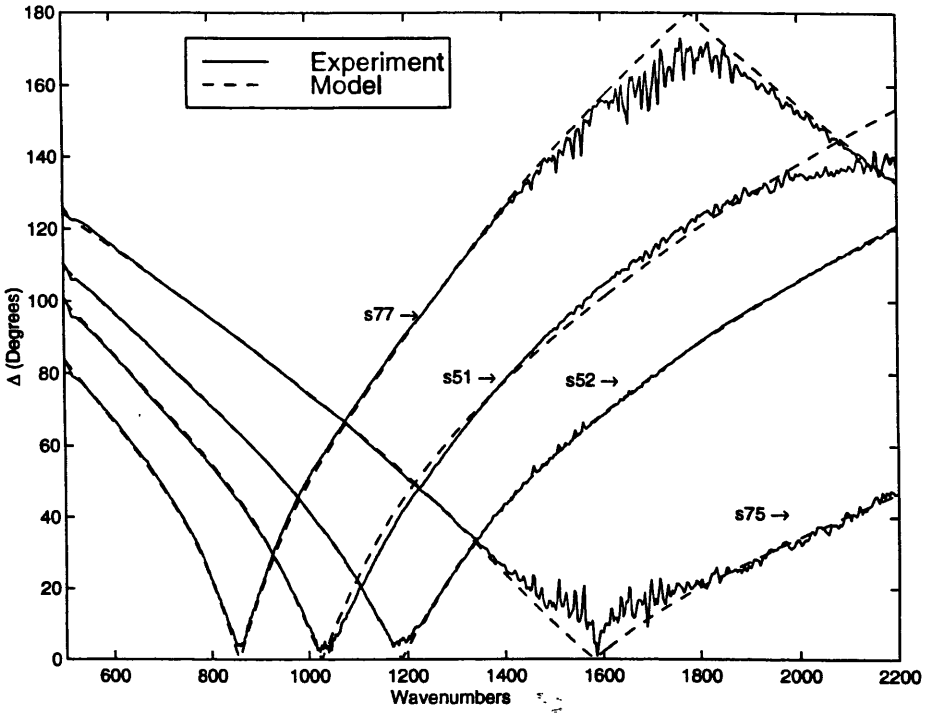

Figure 61: Ellipsometric spectra vs. optimized model predictions using instrument A.

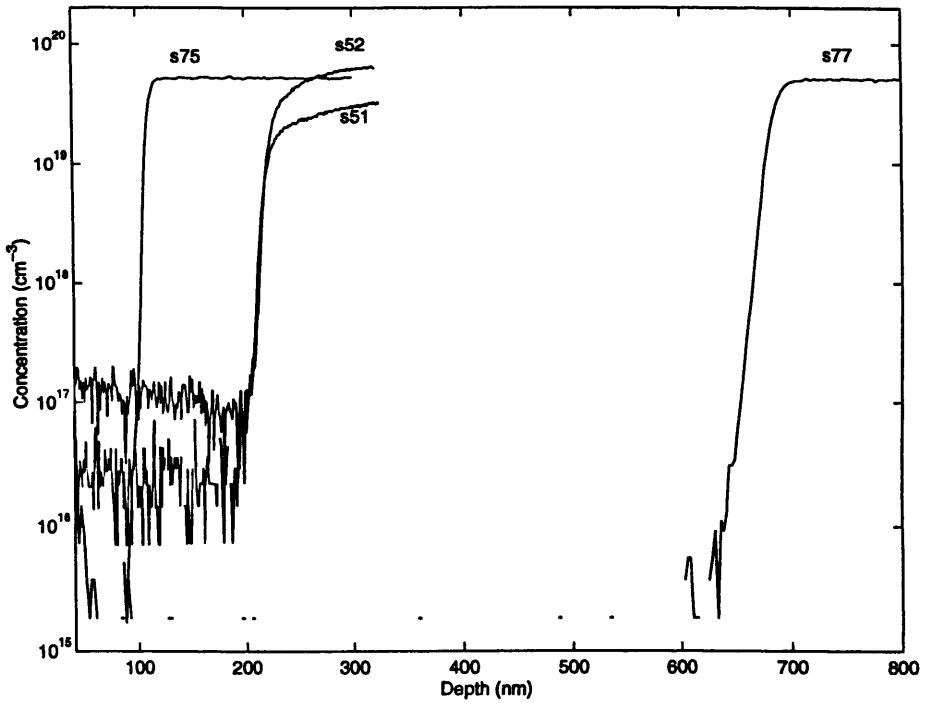

Figure 62: SIMS characterization results

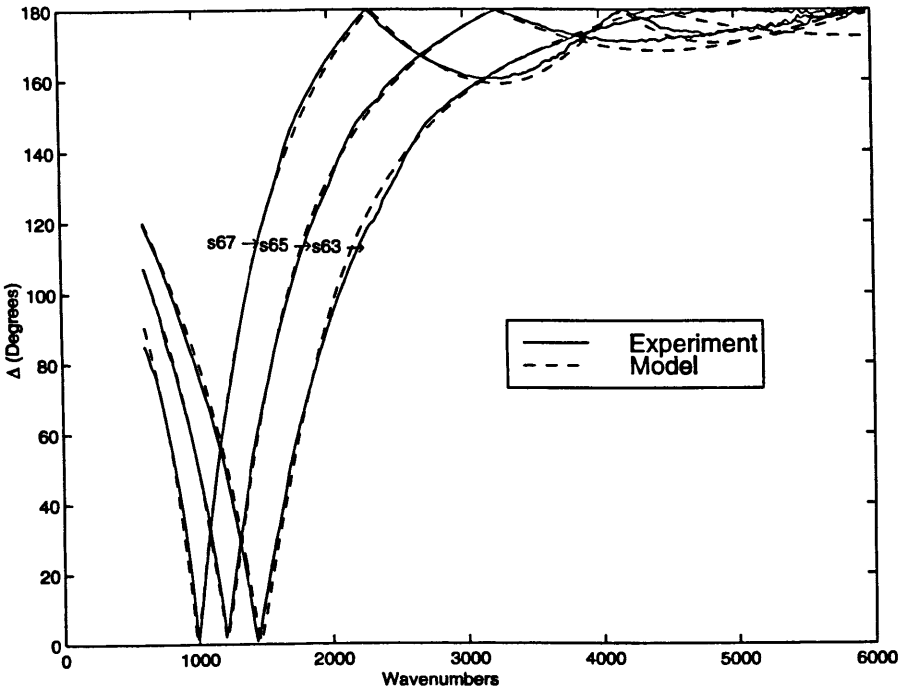

Figure 63: Ellipsometric spectra vs. optimized model predictions using instrument B.

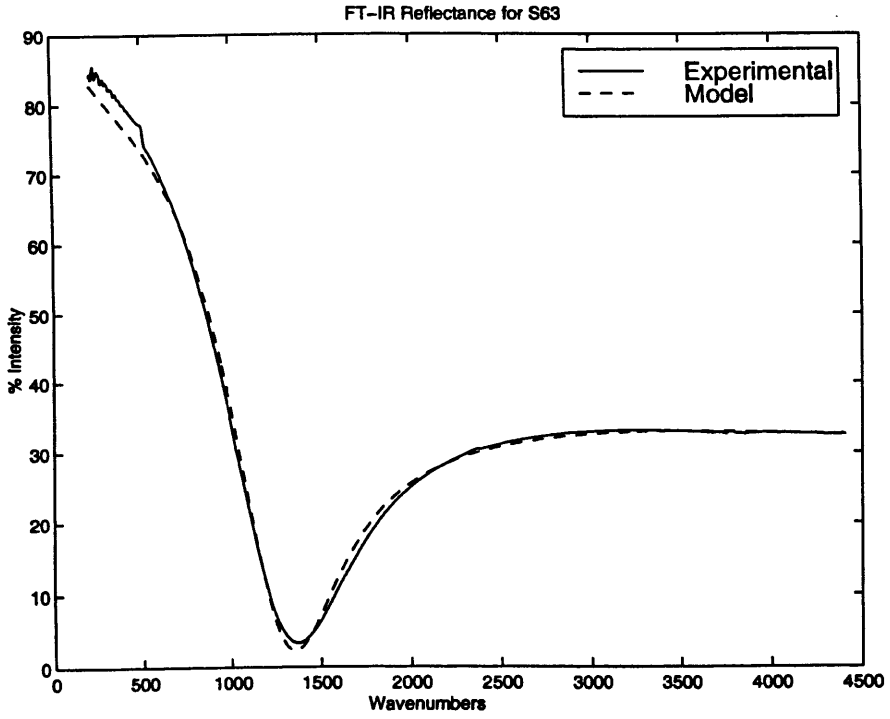

Figure 64: Optimized vs. experimental FT-IR spectra for sample s63. N_{sub} = 1.07E20, d_{epi} = 171 nm.

Results

The models and methods described in the previous chapters dealing with FT-IR measurements are directly applicable to the IRSE measurements. Since the material and structural models of Chapter 3 contain the *s*- and *p*- polarized Fresnell coefficients, relatively minor modifications were required to adopt the optimization procedure to IRSE. Figure 61 - Figure 63 display the measured and optimized spectra for two sets of thin epi-layers taken by Ellipsometers A and B. Figure 64 provides the FT-IR reflectance spectrum of one of the samples for reference. The results of the measurements are displayed in Table 5.

Sample	Concentration N (10^{18} cm^{-3})	d_{epi} (nm)	Relaxation τ (10^{-15} sec)	Mobility μ (cm^2/Vsec)	Resistivity (mΩ-cm)
S51	87.7	319	8	38	1.9
S52	106	256	6.75	32	1.8
S75	115	123	6.2	29.4	1.8
S77	102	501	6.9	32.8	1.9
S63	115	169	7.3	34.9	1.6
S65	97.7	242	7.6	36.0	1.8
S67	91	378	7.5	35.6	1.93

Table 5: Results from IRSE analysis for thin epi-layer samples

As can be seen, very good agreement is achieved between the model and the experiment for both instruments, including Instrument A, despite the former's lack of compensator and purging, although the loss of accuracy at Δ close to 0 or 180 degrees is obvious. The results also correlate well with the SIMS data and the FT-IR results of the previous chapter. It also seen that IRSE measurements achieve substantially higher resolution than the FT-IR in the frequency mode. This

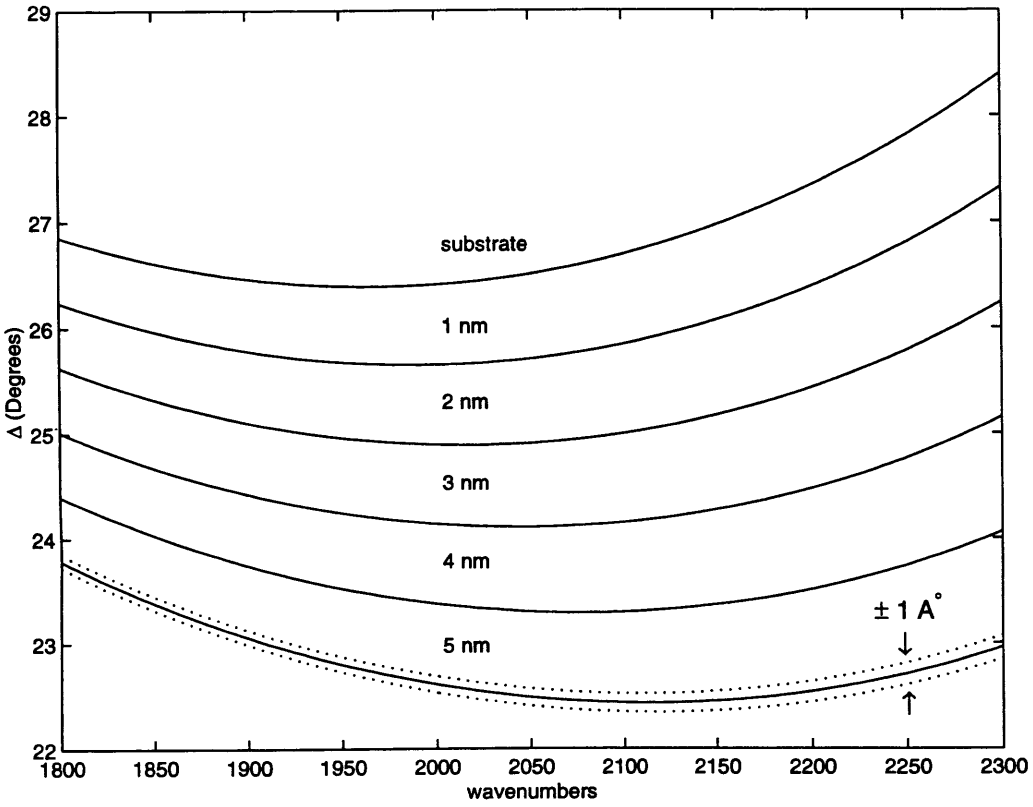

Figure 65: IRSE sensitivity analysis displaying monolayer resolution

becomes apparent by carrying out sensitivity analysis similar to one for FT-IR in Chapter 4.

This is shown in Figure 65. The standard resolution on Δ for conventional ellipsometers is typically in the neighborhood of 0.01 Degree. Making a conservative assumption that 0.1 Degree is achievable for an IRSE instrument, and an achromatic retarder is used, a 1 Å thickness resolution should be obtainable. Such resolution is quite remarkable when one considers that it is achieved with the radiation emitted from an incoherent source with wavelength of over 10 um for the sensitive part of the spectral range, which in turn translates into better than 10^5 to 1 detection sensitivity. In addition to the higher thickness sensitivity, IRSE is also able to detect lower levels of optical contrast than possible with FT-IR, as shown in Figure 66. Here, spectral characteristics of 2 um epitaxial film on Boron-doped substrate of $2*10^{17}$ cm^{-3} are calculated for both ellipsometric and reflectance measurements. It is seen that, while the reflectance measurements

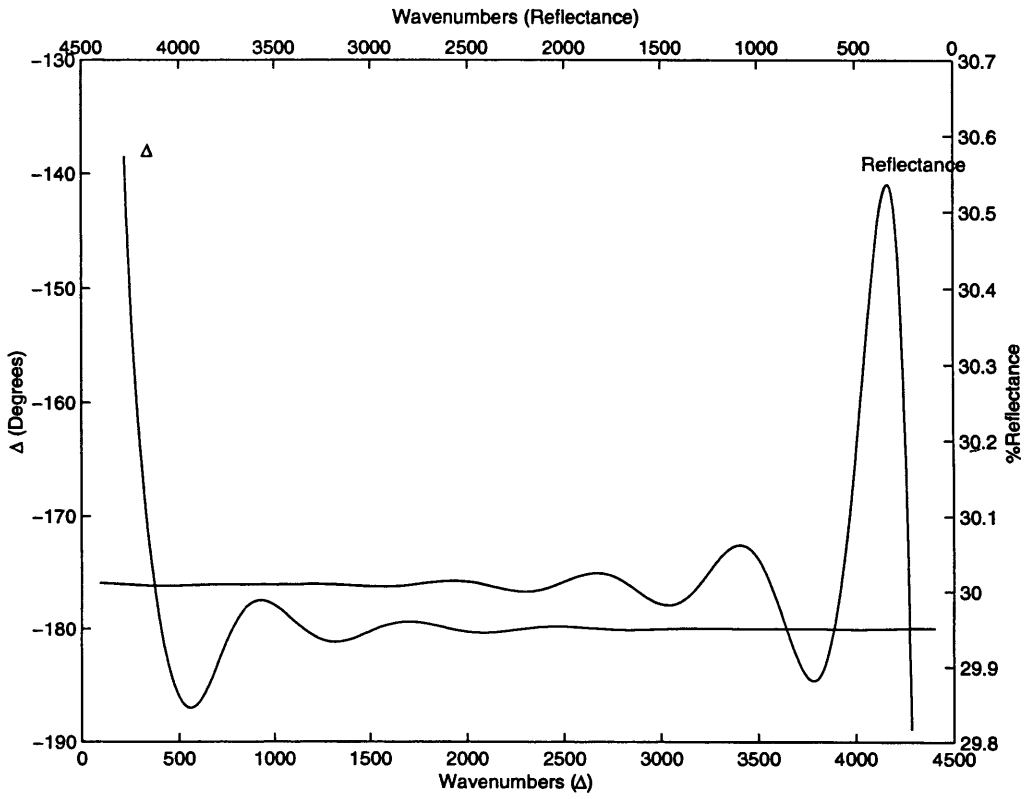

Figure 66: IRSE vs. FT-IR spectra. Simulated 2 um epi-layer on 2E17 doped P^+ substrate.

stand no chance of detecting the resulting interferometric oscillations, the Δ parameter of IRSE is very detectable, and should present no significant problems.

5.5 Concluding Discussion: IRSE vs. FT-IR

From the previous results it may appear that infrared spectroscopic ellipsometry, with its enormous sensitivity to very thin layers and low levels of optical contrast, even when compared with the FT-IR methods described earlier, presents the ultimate in the infrared optical techniques, totally outclassing FT-IR spectrometry. This is not quite so. In fact, both instruments possess advantages and disadvantages versus each other. Clearly, IRSE, by virtue of its polarized phase measurement capability, is by far a more sensitive technique. However, the high sensitivity is

reached at the expense of extra optical components such as polarizers, retarders, and mirrors whose design and manufacture are not trivial and whose performance can not be taken for granted[24]. In the design of optical components, it is extremely desirable to work with materials whose optical properties are uniform across the spectral region of interest. However, the wide-bandwidth nature of the IR measurements and the wavelength range put severe restrictions on the choice of suitable materials[25]. This becomes apparent when one consults an industry data book such as *Handbook of Infrared Optical Materials* [69]. Often seemingly attractive optical properties come at the expense of structural and mechanical perfection. For example, such infrared material as Thallium Bromoiodide, known as KRS-5, has a relatively uniform index of refraction of about 2.38 – 2.25 across a wide IR range (3 um – 34 um) which results in an unusually flat reflectance and transmittance characteristics. However, the material has a rather low melting temperature of 687K and has a serious tendency to cold-flow and change its shape with time. Another popular material, Potassium Bromide (KBr) has better mechanical characteristics, but possesses narrower spectral range and higher dispersion properties. Thus, elaborate methods must often be developed to overcome or minimize the effects of the component imperfections, as was illustrated in this thesis.

Another problem with IRSE, caused by a combination of its sensitivity and component imperfections, is that significant deviations from expected results could be caused by factors not easily understood, or accounted for, by the user. The same sensitivity that enables IRSE to detect small changes in material or structural properties, can cause large variations in measurements due to imperfections in the instrumental components or material surface quality which are not easily modeled. An example of this can be seen comparing optimization results shown in Figure 67 and

---

[24] Properties of mirrors become an issue in polarized measurements and cause deviations in Δ for non-normal angles of incidence.

[25] This is the reason why the most precise measurements are usually carried out at one, or, at best, two wavelengths.

Figure 68. While very good modeling accuracy is achieved on the heavily doped epi-layer sample S63, the modeling fit is considerably worse on the lighter doped sample SEC2, particularly on Δ in the vicinity of 600 – 2000 wavenumbers. Given the fact that excellent accuracy was achieved for that same sample in Chapter 4 using FT-IR methods, and the sample was shown to be of good quality using XTEM and SIMS, a possible reason may do with optical properties of the polarizer and/or retarder in that spectral range, or presence of certain overlayers with rather unusual optical properties.

IRSE is also sensitive to any misallignments of its optical train, and instrument calibration is a very important part of its operation [44]. Since the measurements are typically carried out at high angle of incidence, any deviations from the assumed angle of incidence can cause significant measurement errors. This can be easily seen when comparing the measurement results of instruments A and B, where the angle of incidence differed by 3 degrees. Even if the angle of incidence is set precisely, deviations may still be caused by small tilts in the sample, particularly if the sample is rotated during deposition. In fact, one may construct a Mueller matrix for a tilted sample, where the real plane of incidence differs from the ideal by an angle γ [55]. Knowledge of the sample tilt γ would be important in characterizing metals.

IRSE is also a slower technique than FT-IR, since at least 4 measurements must be taken, one

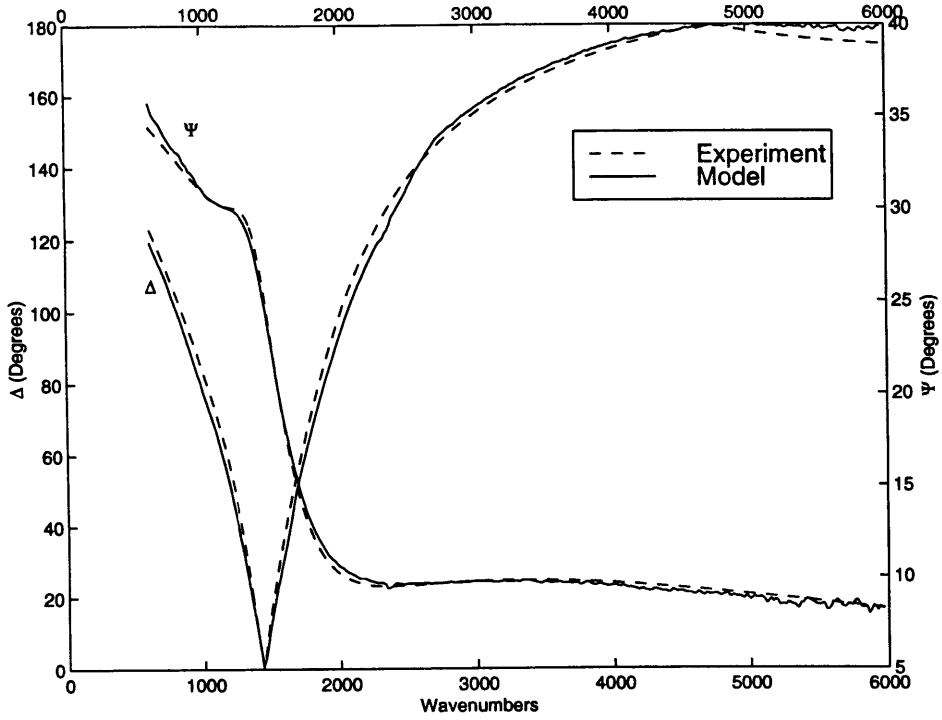

Figure 67: Optimized vs. experimental IRSE spectra for sample s63. N_{sub} = 1.15E20, d_{epi} = 169 nm.

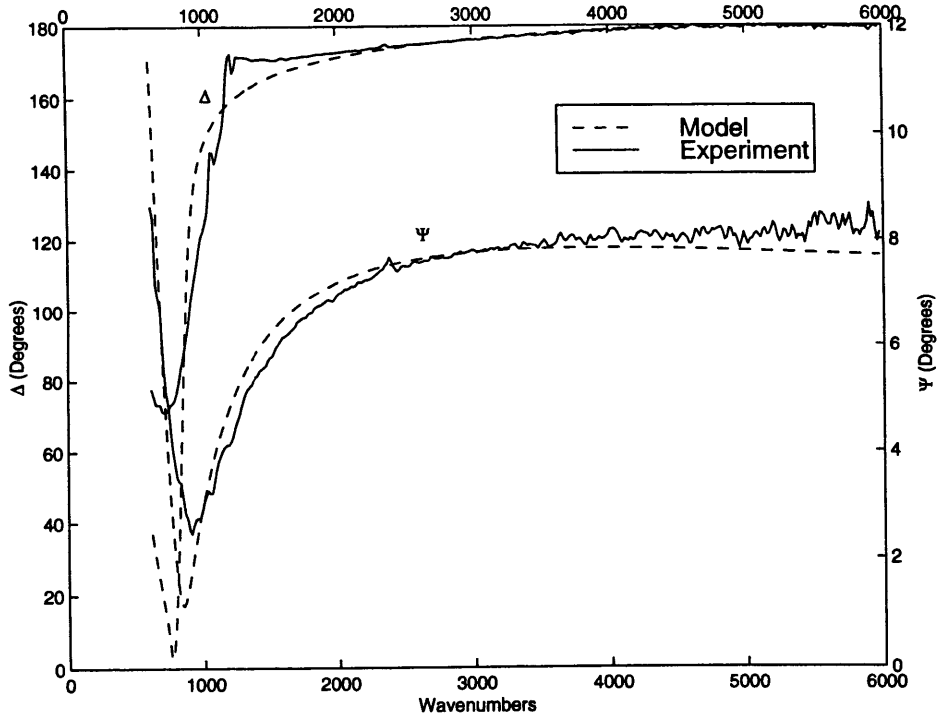

Figure 68: Optimized vs. experimental IRSE spectra for sample SEC2. N_{sub} = 1.63E19, d_{epi} = 158 nm.

for each setting of the analyzer. When a retarder is additionally used, this will be doubled. The speed issue may potentially be overcome by using phase-modulated ellipsometer design as practiced by Drevillon *et. al* [70].

On the other hand, IR ellipsometry possesses several advantages over FT-IR which go beyond sensitivity. One is that by virtue of being a true double-beam technique, ratioing is performed during every measurement, unlike FT-IR in the frequency mode, where the reference spectrum is collected once and can not be easily updated in the case of In-line or *In-situ* applications. FT-IR in the reflectance mode may also be sensitive to differences in the thickness between the sample wafer, and the reference, such as gold mirror. This is due to the fact that the IR beam is usually focused at the sample, and if the reference is of different hight, some energy loss ocurs due to defocusing. This problem does not occur in IRSE, since it is a self-referencing technique. Another potential advantage of IRSE over FT-IR, pointed out by Röseler [34] has to do with the fact that the phase angle Δ sensitivity to rough surfaces, such as present in the back surface of silicon wafer. If the silicon substrate is relatively lightly doped, radiation may not be entirely absorbed in the substrate, and some will be reflected. In the FT-IR case, it would need to be accounted for. However, if the back surface exhibits roughness, radiation reflected from the back would be almost completely depolarized, according to Röseler. It would be interesting to check this experimentally.

To sum up the issue of FT-IR versus IRSE, it's fairly accurate to say that ISE is much more suited as a laboratory research tool with the operator having training in both instrumentation and material properties, and can utilize the instrument's sensitivity to full advantage. On the other hand, FT-IR is a simpler and more robust tool, suitable to production environment on the factory floor, and adoptable, with some effort, for *In-situ* and In-line applications as discussed at the conclusion of Chapter 4, and, when coupled with models and methods described in this thesis, still capable of rather high sensitivity and resolution.

Chapter 6.

Summary and Recommendations for Future Research

Summary

This thesis presented the methods, models and algorithms, which enable precise non-destructive, non-contact characterization of very thin (sub-50 nm) silicon epitaxial films on silicon substrates. The methods provide information on film thickness, substrate doping concentration, and, via relaxation time, resistivity and mobility. Two experimental methods were utilized.

In the first part of the thesis, Fourier Transform Infrared Spectrometry (FT-IR) was utilized in the frequency mode, as opposed to the conventional interferogram mode, as practiced by the industry. Through a combination of physical modeling and signal processing and optimization algorithms, the traditional FT-IR limitations were overcome, and excellent results were obtained

for virtually all samples in the characterization wafer matrix. Films as thin as 47 nm were easily measured, and the technique is capable of better resolution still, with 10 nm results reasonably expected with a nanometer precision. Film thickness is in very good agreement with results of SIMS characterization, and the dopant concentration agrees well with SIMS and 4-point probe results for epi-layers on N^+ substrates, while being overestimated for P^+ types. A more comprehensive model of optical properties of doped silicon, perhaps using energy dependence of the relaxation time and interband transitions into the split-off band may resolve this inconsistency. The effects of the doping profiles, such as the transition layer thickness, were investigated, and determined that, when the combined thickness of the film and transition layer are below 1 um, FT-IR is unable to uniquely resolve the presence of transition layer. That is, for a combination of epi film, transition layer and substrate, there is an equivalent combination of epi-layer and substrate, which produces identical reflectance spectrum. However, when the combined thickness exceeds approximately 1 um, the effects of transition layer become apparent, and the profile may be determined. FT-IR measurements were demonstrated in the presence of relatively low optical contrast, such as 100 nm epi-layers on Sb-doped substrates (10^{18} cm^{-3}), which is not achievable with any other optical method (excluding infrared spectroscopic ellipsometry).

In the second part of the thesis, the methods and models were applied to infrared spectroscopic ellipsometry (IRSE). IRSE is a natural extension of FT-IR spectrometry, but has more involved physics due to polarization properties of stochastic light. Applying methods based upon recommendations of Arnulf Röseler allowed to minimize the effects of non-idealities in main instrument components such as FT-IR beam splitter, and the polarizers, enabling very precise measurements to be made with imperfect components. This method has demonstrated remarkable sensitivity of the phase component, Δ, to very thin layers and very low levels of optical contrast, and the methods and models developed for FT-IR proved to be successfully applied to IRSE as well. Excellent accuracy was obtained for the case of epi-layers on highly doped substrates, and

results correlated well with SIMS and FT-IR data. However, the agreement between the model and experimental spectra deteriorated when the substrate doping level was reduced, particularly for Δ. Since excellent agreement was achieved for these samples using FT-IR, the reason for deterioration may lie with additional imperfections in the optical properties of polarizers and/or retarder in the far end of the spectral range (600 – 2000 wavenumbers), or certain overlayers or interfaces which were not resolved by TEM, SIMS and FT-IR. It was also found that acromatic retarder was essential to study samples which posess low level of optical contrast, such as epi layers on substrates doped less than 10^{19} cm^{-3}. Using achromatic retarder, IRSE should be able, in principle, to achieve monolayer resolution, which is remarkable when utilizing wavelength in the tens of microns range.

Although the techniques described here were designed to deal with problems of thin epitaxial silicon, they have broader applications, and can be applied to any layered structure or profile where optical contrast exists due to the differences in doping level, such as variety of diffused and implanted profiles. It was shown through numerical modeling that FT-IR should be capable of characterizing shallow junctions of at least 25 nm depth, providing information on the thickness, doping level, and implant dose. IRSE should perform significantly better still. The only other tool capable of characterizing such demanding structures is SIMS, which does not measure free carriers, thus it can not study the carrier activation process, and is, of course, destructive. SIMS precision and resolution are also a problem when applied to such challenging structures, and it is not clear if SIMS can achieve monolayer resolution which IRSE seems capable of.

We thus conclude, that the problem of thin epitaxial silicon is virtually solved in a useful, practical manner. These methods should be adoptable by the IC fabrication and metrology industry, and may be utilized for a variety of applications.

Recommendations for Future Research

In-situ Applications

The methods presented in this thesis have broad applicability and can be utilized as enabling technology in a variety of applications. One obvious application to consider is the application of FT-IR and/or IRSE techniques for *In-situ* or In-line monitoring. As mentioned earlier, the extension into *In-situ* area is not as trivial as it may appear, and number of issues would need to be overcome. The application of FT-IR for *In-situ* monitoring of silicon epitaxy was investigated by Z-H Zhow of Professor Rafael Reif's research group at M.I.T.[64]. However, the work focused on the process and control issues and used FT-IR in the conventional, interferogram, mode for monitoring the deposition of relatively thick (> 2 um) epitaxial layers. Since the frequency mode methods of this thesis are far superior, they are very worthwhile investigating. However, as mentioned earlier, issues which include interference with infrared source due to emissions, the effect of the window coating, and the wafer tilting and rotation would need to be researched and overcome. As discussed earlier, FT-IR and IRSE possess certain advantages versus each other for *In-situ* monitoring. While FT-IR is more robust due to its lower sensitivity, simpler operation and low angle of incidence which minimized misalignment and tilting effects, IRSE is superior due to its self-referencing nature. Thus, unlike FT-IR where the reference spectrum may not be easily updated while deposition is taking place, IRSE suffers no such disadvantage. This self-referencing property of IRSE along with its sensitivity, makes possible the following potentially very interesting and extremely powerful tool when used in the emission mode.

Use of FT-IR in the emission mode was investigated by Z.-H.Zhou [71-72]. Unlike the regular use of FT-IR when the sample is illuminated with external IR source, in the emission mode the FT-IR is illuminated by the thermal, black-body radiation emitted from the substrate. Using FT-

IR in the interferogram mode, characteristic interference side-bursts may be observed for thick epi-layers, and deposition temperature may be monitored as well. However, unlike the regular, externally illuminated set-up, the reflectance mode measurements are not applicable to emission mode, since the reference spectrum is not available. However, IRSE is very applicable since it is a self-referencing technique. Using IRSE in the emission mode, one of the major problems for *In-situ* measurements, interference between the external source and thermal radiation is eliminated as well.

Patterned Wafers

Another research area of importance is to investigate the applications of these methods to patterned structures, such as selective epitaxial silicon, and patterned shallow junctions. As discussed at the conclusion of Chapter 4, patterned wafers present serious challenges. However, this problem could still be tackled from two opposite directions.

One way is to take advantage of the fact that during the initial stages of FEOL processing, the pattern features are not as complicated as in the later stages, and, in many cases, large areas of regular structures arranged in a periodic pattern, can be found, as, for example, in DRAMs, SRAMs, and gate arrays/standard cells. In this case, one may use wide-area illumination and attempt to solve the problem through additional modeling. For example, if the thickness (or depth) of the structures of interest is large enough, the characteristic interference oscillations can be detected, as shown in chapter 4. As thickness is reduced, the oscillations disapper, and the modeling can get rather involved. There is no doubt that such work would involve considerable amount of experimentation with different patters and isolation schemes.

The second avenue is to explore the use of infrared microscopy. Using pin-hole ilumination, the IR beam can be narrowed down to a few tenths of micron in diameter, limited by the minimum

amount of energy required for reliable detection. Additional 2-D scanning , or, alternatively, focal plane array detectors, may be utilized to collect more information about lateral geometry which can be used to increase lateral resolution [73]. This offers interesting opportunity for those who would like to combine solid state and optical physics with digital signal and image processing techniques.

Another, perhaps more drastic solution is to explore the use of near-field infrared microscopy, via IR proximity probes. Research work is advancing in materials suitable for use in the infrared optical fibers, which can greatly enhance the flexibility of steering IR radiation. Ability to confine the IR beam to a small area and utilize signal processing techniques as enabled via FT-IR or IRSE can lead to very interesting possibilities.

Appendix A.

As shown in Equation 5.21 of Chapter 5, the Stokes vector at the detector is given by the product of the individual Mueller matrices of the two polarizers, sample, and the Stokes vector of the light emitted by the FT-IR:

$$S_d = \mathbf{M}_{pol}\mathbf{M}_{samp}\mathbf{M}_{anal}S_{FT-IR} \tag{A1}$$

where the Stokes vector of FT-IR is given as

$$S_{FT-IR} = \begin{pmatrix} s_0 \\ s_1 \\ 0 \\ 0 \end{pmatrix} \tag{A2}$$

Thus the degree of polarization of the light from FT-IR is given as

$$P_{FT-IR} = \frac{s_1}{s_0} \tag{A3}$$

The individual Mueller matrices of the polarizers and the sample were previously given by Equations 5.19 and 5.20. The Stokes vector of the light after reflected from the sample is given as:

$$\begin{aligned} S' &= \mathbf{M}_{samp}\mathbf{M}_{anal}S_{FT-IR} \\ &= K\begin{pmatrix} 1 & -\cos 2\psi & 0 & 0 \\ -\cos 2\psi & 1 & 0 & 0 \\ 0 & 0 & \sin 2\psi\cos\Delta & \sin 2\psi\sin\Delta \\ 0 & 0 & -\sin 2\psi\sin\Delta & \sin 2\psi\cos\Delta \end{pmatrix} \\ &\times\begin{pmatrix} 1 & \cos 2\vartheta\cos 2\alpha & \cos 2\vartheta\sin 2\alpha & 0 \\ \cos 2\vartheta\cos 2\alpha & \cos^2 2\alpha+\sin^2 2\alpha\sin 2\vartheta & \sin 2\alpha\cos 2\alpha(1-\sin 2\vartheta) & 0 \\ \cos 2\vartheta\sin 2\alpha & \sin 2\alpha\cos 2\alpha(1-\sin 2\vartheta) & \sin^2 2\alpha+\cos^2 2\alpha\sin 2\vartheta & 0 \\ 0 & 0 & 0 & -\sin 2\vartheta \end{pmatrix}\begin{pmatrix} s_0 \\ s_1 \\ 0 \\ 0 \end{pmatrix} \end{aligned} \tag{A4}$$

where

$$\cos 2\vartheta = \frac{\tau_M - \tau_m}{\tau_M + \tau_m}, \qquad \sin 2\vartheta = \frac{\tau_M \tau_m}{\tau_M + \tau_m} \tag{A5}$$

are the polarizer non-idealities,

and α, τ_M and τ_m are the polarizer azimuth and maximum and minimum transmissions respectively, and

$$K = (\frac{\tau_M + \tau_m}{2})(\frac{|r_s|^2 + |r_p|^2}{2}) \tag{A6}$$

Carrying out the multiplication (A4),

$$S' = K\begin{pmatrix} s_0 + (\cos 2\vartheta \cos 2\alpha)s_1 - \cos 2\psi[(\cos 2\vartheta \cos 2\alpha)s_0 + (\cos^2 2\alpha + \sin^2 2\alpha \sin 2\vartheta)s_1] \\ -\cos 2\psi[s_0 + (\cos 2\vartheta \cos 2\alpha)s_1] + (\cos 2\vartheta \cos 2\alpha)s_0 + (\cos^2 2\alpha + \sin^2 2\alpha \sin 2\vartheta)s_1 \\ \sin 2\psi \cos\Delta[(\cos 2\vartheta \sin 2\alpha)s_0 + \sin 2\alpha \cos 2\alpha(1 - \sin 2\vartheta)s_1] \\ \sin 2\psi \sin\Delta[(\cos 2\vartheta \sin 2\alpha)s_0 + \sin 2\alpha \cos 2\alpha(1 - \sin 2\vartheta)s_1] \end{pmatrix}$$

(A7)

Setting the azimuth of the second (fixed) polarizer at 45^0, the Mueller matrix simplifies to

$$\mathbf{M}_{pol} = \begin{pmatrix} 1 & 0 & \cos 2\vartheta & 0 \\ 0 & \sin 2\vartheta & 0 & 0 \\ \cos 2\vartheta & 0 & 1 & 0 \\ 0 & 0 & 0 & -\sin 2\vartheta \end{pmatrix} \tag{A8}$$

Thus, multiplying (A7) and (A8), produces for the first element of the overall Stokes vector:

$$s_0^{\,d} = K[s_0 + (\cos 2\vartheta \cos 2\theta)s_1 - \cos 2\psi\{(\cos 2\vartheta \cos 2\theta)s_0 + (\cos^2 2\theta + \sin^2 2\theta \sin 2\vartheta)s_1\}$$
$$+ \cos 2\vartheta\{(\cos 2\vartheta \sin 2\theta)s_0 + \sin 2\theta \cos 2\theta(1 - \sin 2\vartheta)s_1\} \sin 2\psi \cos\Delta]$$

(A9)

List of References

1. D. J. Meyer, "Epi's needs in device technology", *Semiconductor International*, no.7, p.70, Jul. 1991.
2. S. M. Sze, *VLSI Technology*, 2nd Ed., McGraw Hill, 1988.
3. National Technology Roadmap for Semiconductors. Technology Needs. SIA. 1997.
4. P. Burggraaf, "Epi's leading edge", *Semiconductor International*, no. 7, p.68, Jul. 1991.
5. *Electronic News*, Jan. 12, 1998.
6. J. O. Borland, T. E. Seidel, *Solid State Technology*, vol.39, no.6, p.89 (June 1996).
7. *Electronic News*, vol. 42, no. 2121, June 17, 1996.
8. L. Rubin, W. Morris, "High-energy ion implanters take off", *Semiconductor International*, no. 4, vol. 20, p. 77, April 1997.
9. Hyungsoon Shin, Al F. Tash, *et al.*, "MOSFET drain engineering analysis for deep-submicron dimensions: a new structural approach", *IEEE Transactions of Electron Devices*, vol. 39, no. 8, p. 1922, Aug. 1992.
10. H. Tian *et al.*, "Effects of profile doped elevated source/drain structures on deep-submicron MOSFETs", *Solid State Electronics*, vol. 38, p.573, 1995.
11. J. R. Pfiester, *et al.*, "A self-aligned elevated source/drain MOSFET", *IEEE Electron Device Letetrs*, vol. 11, no. 9, Sept. 1990.
12. Yuan Taur, *et al.*, "CMOS scaling into the nanometer regime", *Proceedings of the IEEE.*, vol. 85, no. 4, April 1997.
13. R. DeJule, "Meeting the ultra-shallow junction challenge", *Semiconductor International*, no. 4, vol. 20, p. 50, April 1997.
14. H. C. Theurer, J. J. Kleimack, H. H. Loar, and H. Christensen, Proceedings of I.R.E., vol. 48, p. 1642, 1960.
15. R. R. Troutman, *Latch-Up in CMOS Technology: The Problem and Its Cure*, Boston, Mass.: Kluwer Academic Publishers, 1986.
16. N. W. Ashcroft, N. D. Mermin, *Solid State Physics*, Philadelphia, PA, HRW, 1976.
17. W. G. Spitzer, M. Tanenbaum, "Interference method for measuring the thickness of epitaxially grown films", *J. Appl. Phys.*, vol. 32, p. 744, 1961.

18. The American Society for Testing and Materials (ASTM), Committee F1 on Electronics, Philadelphia, PA.
19. P. A. Schumann, R. P. Phillips, "Comparison of classical approximations to free carrier absorption in semiconductors", *Solid State Electronics*, vol. 10, no. 9, p.943, 1967.
20. P. A. Shumann, C. P. Schneider, "Measurement of silicon epitaxial layers less than 1-um thick by infrared interference", *J. Appl. Phys.*, vol. 41, no. 8, p.234, 1970.
21. P. J. Severin, "Correction to be applied to the thickness of an epitaxial layer measured with infrared multiple interference", *J. Electrochem. Soc.*, vol. 122, no. 7, p. 962, 1975.
22. B. Senitzky, S. P. Weeks, "Infrared reflectance spectra of thin epitaxial silicon layers", *J. Appl. Phys.*, vol. 52, no. 8, p. 5308, 1981.
23. P. A. Flournoy, R. W. McClure, G. Wyntjes, "White-light interferometric thickness gauge", *Applied Optics.*, vol. 11, no. 9, p.1907, 1972.
24. K. Krishnan, P. J. Stout, *Practical Fourier Transform Infrared Spectroscopy*, J. R. Ferraro and K. Krishnan, ed., (Academic Press, Orlando, 1990), p.285.
25. P. R. Griffiths, J. A. de Haseth, *Fourier Transform Infrared Spectrometry*, J. Wiley, New York, 1986.
26. Max Born and Emil Wolf, *Principles of Optics*, 6th Edition, 1980.
27. P. J. Severin, "The influence of the phase shift on thickness measurements of silicon epitaxial layers with a Fourier transform infrared spectrometer", *J. Electrochem. Soc.*, vol. 121, no. 1, p. 150, 1974.
28. P. J. Severin, "Interpretation of the infrared thickness measurement of epitaxial layers", *Applied Optics.*, vol. 11, no. 3, p.691, 1972.
29. R. W. Collins, Y-T. Kim, "Ellipsometry for thin-film and surface analysis", *Analytical Chemistry*, vol. 62, no. 17, p. 887a, Sept. 1990.
30. F. Ferrieu, J. H. Lecat, "Spectroscopic Ellipsometry for the characterization of thin films", *J. Electrochem. Soc.*, vol. 137, no. 7, p. 2203, 1990.
31. B. Drevillon, "Phase modulated ellipsometry from the ultraviolet to the infrared: *in-situ* applications to the growth of semiconductors", *Prog. Crystal Growth and Charact.*, vol. 27, p.1, 993.

32. T. A. Leonard, J. Loomis, K. G. Harding, M. Scott, "Design and construction of three infrared ellipsometers for thin film research", *Optical Enineering*, vol. 21, no. 6, p. 971, 1982.

33. A. Röseler, "Spectroscopic ellipsometry in the infared", *Infrared Physics*, vol. 21, p. 349, 1981.

34. A. Röseler, "IR spectroscopic ellipsometry: instrumentation and results", *Thin Solid Films*, vol. 234, p. 307, 1993.

35. H. F. Hazebroek, A. A. Holscher, *J. Phys. E.: Sci. Instr.*, no. 6, p. 822, 1973.

36. A. Corney, *Atomic and Laser Spectroscopy*, Chapter 8. Clarendon Press, Oxford, 1977.

37. R. Loudon, *The Quantum Theory of Light*, 2nd Edition, Clarendon Press, Oxford, 1983.

38. A. Papoulis, *Systems and Transforms with Applications in Optics*, McGraw-Hill, New York, 1968.

39. A. Papoulis, *Probability, Random Variables and Stochastic Processes*, 3rd Edition, McGraw-Hill, New York, 1991.

40. S. M. Kay, *Fundamenrals of Statistical Signal Processing and Estimation Theory*, Prentice-Hall, 1993.

41. H. Stark, J. Woods, *Probability, Random Processes, and Estimation Theory for Engineers*, 2nd Edition, Prentice-Hall, 1994.

42. H. A. Haus, *Waves and Fields in Optoelectronics*, Prentice-Hall, 1984.

43. E. Hecht, *Optics*, 2nd Edition, Addison-Wesley, 1987.

44. R. M. A. Azzam, N. M. Bashara, *Ellipsometry and Polarized Light*, North-Holland, 1977.

45. G. R. Srinivasan, "Autodoping effects in silicon epitaxy", *J. Electrochem. Soc.*, vol. 127, no. 6, p. 1334, 1980.

46. A. S. Grove, A. Roder, C. T. Sah, *J. App. Phys.*, vol. 36, p. 802, 1965.

47. J. J. Grossman, *J. Electrochem. Soc.*, vol. 110, p. 1065, 1963.

48. Abeles, F., *Ann. De Physique*, vol 5, p. 596, 1950.

49. W. G. Spitzer, H. Y. Fan, "Determination of optical constants and carrier effective mass of semiconductors", *Physical Review*, vol. 106, no. 5, June 1, 1957.

50. R. A. Smith, *Semiconductors*, 2nd Edition, Cambridge University Press, Cambridge, 1978.

51. A. Borghesi, A. Stella *et al.*, "Optical determination of Si conduction band non-parabolicity", *J. App. Phys.*, vol. 67, no. 6, p. 3102, 1990.

52. E. Barta, "Determination of effective mass values by a Kramers-Kronig analysis for variously doped silicon crystals", *Infrared Physics*, vol. 17, p. 111, 1977.

53. M. Auslander, S. Hava, "Free carrier contribution to dynamic dielectric function of heavily doped semiconductors. Application to n-type silicon", *Phys. Stat. Sol. (B)*, vol. 174, p. 565, 1992.

54. A. V. Oppenheim, R. W. Schafer, *Discrete-Time Signal Processing*, Chapter 10, Prentice-Hall, 1989.

55. A. Röseler, *Infrared Spectroscopic Ellipsometry*, Academie-Verlag, Berlin, 1990.

56. Y-S. Yen, J. S. Wong, "Band distortions and inversions in FTIR spectra of silicon dioxide on silicon", IBM technical report, 1981.

57. J. S .Wong, Y-S Yen, "Intriguing absorption band behavior of IR reflectance spectra of silicon dioxide on silicon", *Applied Spectroscopy*, vol. 42, no. 4, p.598, 1988.

58. J. F. Ziegler, *Handbook on Ion Implantation Technology,* North-Holland, Amsterdam, 1992.

59. E. Chason, S. T. Picraux, *et al.*, "Ion beams in silicon processing and characterization", *J. App. Phys.,* vol.81, no. 10, pp. 6513-6561, 15 May 1997.

60. G. Strang, *Introduction to Applied Mathematics,* Wellesley-Cambridge Press, 1986.

61. Y. Bard, *Nonlinear Parameter Estimation.*, Academic Press, New York, 1974.

62. H. A. Lyden, "Measurement of the conductivity effective mass in semiconductors using infrared reflection", Physical Review, vol. 134, no. 4A, p. A1106, 1964.

63. R. B. Herring, "Advances in reduced pressure silicon epitaxy", *Solid State Technol.* Vol. 22, p. 75, 1979.

64. Z-H. Zhou, "Real-time *In-situ* monitoring and control of silicon epitaxy by Fourier Transform Infrared Spectroscopy", PhD Thesis, M.I.T., 1993.

65. F. Zenhausern, Y. Martin, H. K. Wickramasinghe, "Scanning interferometric apertureless microscopy: optical imaging at 10 angstrom resolution", *Science*, vol. 269, 25 August 1995.

66. R. C. Jones, *J. Opt. Soc. Am.*, vol. 31, p.488, 1941.

67. H. Mueller, *J. Opt. Soc. Am.*, vol. 38, p. 661, 1948.

68. A. Röseler, "Improvement in accuracy of spectroscopic IR ellipsometry by the use of IR retarders", *Infrared Physics*, vol. 24, p. 1, 1984.

69. P .Klocek, editor, *Handbook of Infrared Optical Materials*, Marcel Dekker, inc., New York, 1991.

70. A. Canillas, E. Pascual, B. Drevillon, "Phase-modulated ellipsometer using a Fourier transform infrared spectrometer for real time applications", *Rev. Sci. Instrum.*, vol. 64, no. 8, p.2153, August 1993.

71. Z-H Zhou, R. Reif, "Epi-film thickness measurements using emission fourier transform infrared spectroscopy – Part I: sensor characterization", *IEEE Trans. On Semiconduct. Manufact.*, vol. 8, no. 3, p. 333, August 1995.

72. Z-H Zhou, R. Reif, "Epi-film thickness measurements using emission fourier transform infrared spectroscopy – Part II: real-time *In-situ* process monitoring and control", *IEEE Trans. On Semiconduct. Manufact.*, vol. 8, no. 3, p. 340, August 1995.

73. G. M. Robinson, D. M. Perry, R. W. Peterson, "Optical interferometry of surfaces", *Scientific American*, July 1991.